Titre: Title:	Characterization of the Effect of Hydrogen Embrittlement on the Fatigue Crack Propagation Behaviour of AISI 415 Martensitic Stainless Steel
Auteur: Author:	Davoud Harandizadeh Najafabadi
Date:	2022
Type:	Mémoire ou thèse / Dissertation or Thesis
Référence: Citation:	Harandizadeh Najafabadi, D. (2022). Characterization of the Effect of Hydrogen Embrittlement on the Fatigue Crack Propagation Behaviour of AISI 415 Martensitic Stainless Steel [Mémoire de maîtrise, Polytechnique Montréal]. PolyPublie. https://publications.polymtl.ca/10488/

URL de PolyPublie: PolyPublie URL:	https://publications.polymtl.ca/10488/
Directeurs de recherche: Advisors:	Myriam Brochu, & Denis Thibault
Programme: Program:	Génie mécanique

POLYTECHNIQUE MONTRÉAL

affiliée à L'Université de Montréal

Characterization of the Effect of Hydrogen Embrittlement on the Fatigue Crack Propagation Behaviour of AISI 415 Martensitic Stainless Steel

DAVOUD HARANDIZADEH NAJAFABADI

Département de génie mécanique

Mémoire présenté en vue de l'obtention du diplôme de *Maîtrise ès sciences appliquées*

Génie mécanique

Août 2022

POLYTECHNIQUE MONTRÉAL

affiliée à L'Université de Montréal

Ce mémoire intitulé :

Characterization of the Effect of Hydrogen Embrittlement on the Fatigue Crack Propagation Behaviour of AISI 415 Martensitic Stainless Steel

présenté par **Davoud HARANDIZADEH NAJAFABADI**

en vue de l'obtention du diplôme de *Maîtrise ès sciences appliquées*

a été dûment accepté par le jury d'examen constitué de :

Louis LABERGE LEBEL, président
Myriam BROCHU, membre et directrice de recherche
Denis THIBAULT, membre et codirecteur de recherche
Salim BRAHIMI, membre

DEDICATION

To my beloved wife, Fatima, and my sons, Sepanta and Pouya. The ones who gave me the courage of starting and continuing the journey of study and immigration.

ACKNOWLEDGEMENTS

The work was financially supported by the Institut de recherche d'Hydro-Québec (IREQ), SACMI, Natural Sciences and Engineering Research Council of Canada (NSERC) and Consortium de recherche et d'innovation en transformation métallique (CRITM). Collaboration of S. Laliberté-Riverin, Alexandre Bois Brochu (from CMQ), Pierre-Antoy Deschênes and C. Baillargeon is also acknowledged.

RÉSUMÉ

Selon l'approche de tolérance aux dommages, le taux de croissance des fissures de fatigue et le mode de rupture doivent être connus à des fins de conception et de maintenance. Le comportement de croissance des fissures de fatigue de l'alliage AISI 415 est bien établi dans la littérature en raison de sa large utilisation industrielle, en particulier dans la fabrication des hydro-turbines. Cependant, l'effet des paramètres environnementaux sur le comportement de croissance des fissures de fatigue de ce matériau est toujours un domaine d'intérêt ouvert. Dans ce projet, l'effet de l'hydrogène interne (H) sur le taux de croissance des fissures de fatigue et le mode de rupture est étudié pour un acier inoxydable martensitique 415 trempé et revenu avec une résistance ultime (σ_u) d'environ 850 MPa et une teneur en austénite réformée de 20 %. Les propriétés mécaniques d'échantillons enrichis en hydrogène sont comparées à des échantillons bruts à l'aide d'essais de croissance de fissures de traction et de fatigue. Pour enrichir les échantillons en hydrogène, les échantillons sont chargés électrochimiquement en utilisant la méthode du courant constant. Les tests de croissance des fissures de fatigue sont effectués selon la procédure ASTM E647 à deux plages d'intensité de contrainte constante (ΔK = 8MPa.m$^{0.5}$ et 15 MPa.m$^{0.5}$) à trois fréquences de chargement cycliques (f = 35 Hz, 3.5 Hz et 0.35 Hz). Les résultats des tests monotones révèlent qu'une teneur en H interne d'environ 11 mg/kg en poids entraîne une diminution de la ductilité en traction du matériau à deux tiers. Le test de croissance des fissures de fatigue révèle que l'hydrogène interne à une concentration aussi faible que 4 mg/kg en poids augmente le taux de croissance des fissures de fatigue de 2 fois à ΔK =15 MPa.m$^{0.5}$ et f = 0.35 Hz. Les résultats indiquent également que, en plus de la concentration en hydrogène, trois paramètres de la fréquence de charge, le niveau de ΔK et la fermeture des fissures affectent également la sensibilité du le taux de croissance des fissures de fatigue à la fragilisation par l'hydrogène. Un modèle est proposé basé sur les théories de la décohésion assistée par l'hydrogène (HEDE) et de la diffusion induite par les contraintes (SID) pour expliquer l'effet des variables étudiées. Ce modèle original est capable d'expliquer la sensibilité plus élevée du la croissance des fissures de fatigue à la fragilisation interne par l'hydrogène à ΔK=15 MPa.m$^{0.5}$ (par rapport aux résultats obtenus à ΔK=8 MPa.m$^{0.5}$) et à la fréquence de chargement la plus basse testée (0.35 Hz). Le modèle explique la proportion la plus élevée de rupture intergranulaire observée à ΔK=15 MPa.m$^{0.5}$ et f=3.5 Hz.

ABSTRACT

The damage tolerance approach requires knowledge of the fatigue crack growth rate (FCGR) and fracture mechanisms of a material in order to plan inspection intervals so that any propagating cracks can be arrested before leading to a failure. The fatigue crack growth (FCG) behaviour of AISI 415 alloy has been well studied in the literature due to its wide industrial usage, specifically in the fabrication of hydro turbines. However, the effects of environmental parameters on crack propagation in this material has not yet been fully documented. An international partnership known as the Fatigue-Corrosion International Research Project (FATCO) was launched in 2019 to investigate the corrosion fatigue behaviour of 13Cr-4Ni alloy. Since hydrogen may be emitted during corrosion, the present study was defined as part of the FATCO project to determine the impact of absorbed hydrogen on fatigue crack growth in AISI 415 steel. To address this central question, a test method is established to introduce hydrogen to AISI 415 and its efficiency and reproducibility are validated. Then, the effect of absorbed hydrogen on the FCGR of AISI 415 is measured. In addition, its effect on the fatigue fracture mechanism is characterized. Lastly, the observed effect of hydrogen on the FCGR and fatigue fracture mode are explained theoretically.

In this project, the effects of pre-charged hydrogen (H) on the fatigue crack growth kinetic and fracture mechanisms are studied for a quenched and tempered 415 martensitic stainless steel with an ultimate strength (σ_u) of approximately 850 MPa and 20 % reformed austenite content. The mechanical properties of samples enriched with hydrogen are compared to raw samples in tensile and fatigue crack growth tests. To enrich the samples with hydrogen, electrochemical charging under a constant current is performed. Fatigue crack growth (FCG) tests are conducted following the ASTM E647 procedure at two constant stress intensity factor ranges (ΔK= 8 MPa.m$^{0.5}$ and 15 MPa.m$^{0.5}$) and three cyclic loading frequencies (f=35 Hz, 3.5 Hz and 0.35 Hz).

The results of monotonic tests reveal that a pre-charged H content close to the solubility limit (more than 13 mg/kg) causes a 30 % decrease in material ductility. FCG testing reveals that pre-charged hydrogen in concentrations as small as 4 mg/kg doubles the FCGR at a specific ΔK of 15 MPa.m$^{0.5}$ and frequency of 0.35 Hz. In addition to the concentration of hydrogen, other factors influencing the sensitivity of the FCGR to hydrogen are the load frequency, level of ΔK, and crack closure.

A model is proposed based on hydrogen enhanced decohesion (HEDE) and stress induced diffusion (SID) theories to explain the effects of the variables studied. SID is used to describe how hydrogen atoms tend to accumulate around a crack tip. Based on this model, the amount of accumulated hydrogen around the crack tip is dictated by competition between the crack velocity and hydrogen diffusion rate. It is hypothesized that based on HEDE, the severity of the effect of hydrogen on the FCGR is controlled by the amount of hydrogen accumulated in front of the crack. This original model explains higher FCG susceptibility to hydrogen embrittlement at ΔK=15 MPa.m$^{0.5}$ (when compared to results obtained at ΔK=8 MPa.m$^{0.5}$) and at the lowest loading frequency tested (0.35 Hz). The model also explains the highest proportion of intergranular fracture observed at ΔK=15 MPa.m$^{0.5}$ and f=3.5 Hz.

TABLE OF CONTENTS

LIST OF TABLES

LIST OF FIGURES

LIST OF SYMBOLS AND ABBREVIATIONS

ΔK	Stress intensity range in fatigue (MPa.m$^{0.5}$)
μ	Chemical potential
μ^0	Reference chemical potential
σ	Applied stress
σ_{max}	Maximum stress of fatigue stress range
σ_{min}	Minimum stress of fatigue stress range
σ_u, *UTS*	Ultimate tensile strength
σ_y, *YS*	Yield stress
σ_H	Hydrostatic stress
v_{crack} , $(\frac{da}{dt})$	Fatigue crack velocity (mm/s)
a	Crack length
B	Thickness of the CT sample
C, m	Constants of Paris equation
C_σ	Hydrogen concentration in stressed area
C_U	Hydrogen concentration in unstressed area
C_L	Hydrogen concentration in metal lattice
CSHE	Cyclic susceptibility to hydrogen embrittlement

CT	Compact tension sample from fatigue test
CZ	Cyclic zone
CZS	Cyclic zone size
d	Distance from critical volume to crack tip
D	Hydrogen diffusion rate
D_{NZ}	Diameter of neighbourhood zone
D_{MZ}	Diameter of monotonic zone
D_{PAG}	Diameter of parent austenite grain
f	Fatigue loading frequency (Hz)
$FCGR$, $(\frac{da}{dN})$	Fatigue crack growth rate (mm/cycle)
h	Width of notch in CT samples
HEDE	Hydrogen enhanced decohesion theory
HELP	Hydrogen enhanced localized plasticity
IG	Portion of fracture surface covered by intergranular features
k	Portion of diffusible H reaching critical volume before crack reaches it
K_C	Material fracture toughness
K_{max}	Maximum stress intensity in fatigue
L	Maximum hydrogen diffusion length before crack reaches critical element
$\bar{V}_H$	Partial molar volume of hydrogen

$\mathcal{R}$	Gas constant (J.mol^{-1}.K^{-1})
MSHE	Monotonic susceptibility to hydrogen embrittlement
MZ	Monotonic zone
MZS	Monotonic zone size
N	Number of fatigue cycles
N_{CV}^{1}	Initial number of H atoms in critical volume
N_{CV}^{2}	Number of accumulated H atoms in critical volume under stress
NZ	Neighbourhood zone
R	Stress ratio during fatigue test
r_{NZ}	Radius of neighbourhood zone
r_{MZ}	Radius of monotonic zone
SID	Stress induced diffusion theory
t	Time (s)
T	Temperature
V_{NZ}	Volume of neighbourhood zone
V_{MZ}	Volume of monotonic zone
W	Width of CT sample
Z	Ratio of released hydrogen to initially trapped hydrogen

LIST OF APPENDICES

CHAPTER 1 INTRODUCTION

Hydraulic turbines are massive facilities installed in the complex infrastructure of dams with limited accessibility for maintenance. An example of such turbines is schematically presented in the Figure 1-1. Hydraulic turbine facilities in Quebec have power ranges of 4 to 442 MW, with runners (the assembly of the blades) weighing from around 10 to 100 tons. Therefore, it is essential to choose durable material for their fabrication so that they are able to tolerate heavy working conditions for prolonged periods. The main deterioration phenomena acting on these turbines are fatigue, corrosion, erosion, and cavitation. Currently, different parts of the turbines, such as the runners (Figure 1-1), are produced by different turbine manufacturers with martensitic stainless steels containing more than 12 % Cr and around 4 % Ni. AISI 415 is a martensitic stainless steel from this family which is widely used in the hydraulic turbines of Hydro-Québec facilities. This family of industrial alloys is well known for their good tensile strength in quenched and tempered condition (usually between 800 and 1000 MPa) [1] and good general and localized corrosion resistance. They also demonstrate good cavitation resistance and weldability [2]. These characteristics promote their use in fabrication of critical parts of hydro turbines such as runners, parts expected to have a long fatigue life in an aquatic environment [3]. The synergetic effect of corrosion and fatigue can promote a phenomenon known as corrosion fatigue. Understanding this deterioration process is vital for design purposes as well as for turbine inspection, maintenance and operation management. In 2019, an international partnership known as the Fatigue-Corrosion International Research Project (FATCO) was launched to study the corrosion fatigue behaviour of AISI 415.

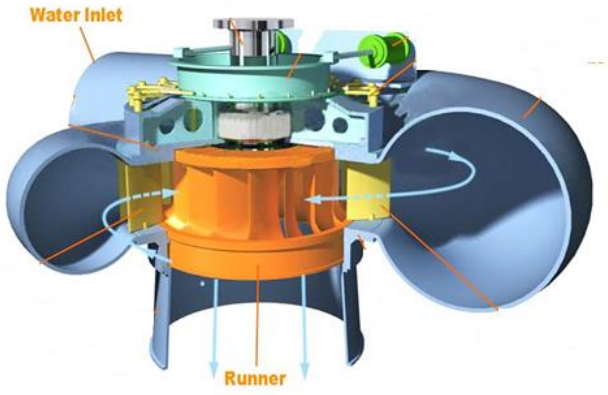

Figure 1-1 Schematic of a Francis turbine [4]

Some degree of localized corrosion is expected and reported in industrial investigations on parts of hydraulic turbines fabricated from AISI 415. This leads to hydrogen release in the active corrosion sites, where this atomic hydrogen can be readily absorbed by the material, raising concerns about the material's resistance to hydrogen embrittlement. While much of the literature emphasizes the significant effect of hydrogen embrittlement on deterioration of mechanical properties in high strength steels (i.e., steels with tensile strength higher than 1000 MPa), there is also some evidence of a negative effect on lower strength steels. Furthermore, it has been proven that the presence of hydrogen can enhance the FCGR for a range of engineering materials. Nevertheless, diffused hydrogen impacts on fatigue behaviour are not limited to high strength steels. Increases in the fatigue crack growth rate in a hydrogen atmosphere were reported by Tsay [3] for two austenitic stainless steels with ultimate strength less than 800MPa. Moreover, Rodkey and Jones [5] studied the effect of internal hydrogen on the fatigue crack growth rate of a martensitic stainless steel containing 12 % Cr and concluded that 4 atomic ppm of hydrogen can significantly increase the fatigue crack growth rate (5 times at $\Delta K = 14$ MPa.m$^{0.5}$ and frequency of 0.2 Hz). In this context, a complete picture of the corrosion fatigue behaviour of AISI 415 will require characterization of the effect of hydrogen embrittlement on fatigue crack growth.

In order to implement the defect tolerance design approach, it is essential to characterize the fatigue crack growth kinetic and how it is impacted by service conditions. There is a demand to characterize the effect of hydrogen embrittlement on the fatigue crack growth behavior of 415 martensitic stainless steel. Therefore, this project focuses on the research question: What is the impact of absorbed hydrogen on fatigue crack growth in AISI 415 steel? The present thesis provides an overview of the project context, methodology, results and a discussion interpreting the results.

Chapter 2 provides a literature review divided into 3 main subsections. The first introduces the typical properties of 415 stainless steel. The second offers an overview of existing knowledge on fatigue crack propagation and affecting factors. The third section introduces theories on the phenomenon of hydrogen embrittlement under monotonic and cyclic loading conditions. Regarding the available literature, this project's specific objective will be clarified at the end of this chapter.

Throughout Chapter 3, the project's methodology will be discussed. First, different variables of the project will be identified and categorized as dependent, independent, control or moderator variables. Then, the test plan will be introduced, followed by reports of the material properties, experimental procedures and test methods.

In Chapter 4, the test results regarding the effect of H on monotonic mechanical properties of AISI 415 will be presented.

In Chapter 5 the results regarding the effect of H on fatigue crack propagation will be presented within a scientific manuscript submitted to *Engineering Fracture Mechanic*.

While the aforementioned article covers discussion of a significant part of the results, Chapter 6 provides a general discussion in regard to the project's specific objectives.

Chapter 7 provides the conclusion, limitations of the study and some recommendations for further studies.

CHAPTER 2 LITERATURE REVIEW

This chapter will begin with a review of the characteristics of the material under study, and then provide an overview of the principles of fatigue crack propagation. In the next subsection, a review of the principles of hydrogen embrittlement will be provided, beginning with the general concepts, and then narrowing focus to the effects of hydrogen embrittlement on the FCG of martensitic stainless steels. The objectives of the project will then be defined with the intention of addressing the knowledge gap in the literature and the practical needs of our industrial partner.

2.1 Nominal characteristics of AISI 415 steel

AISI 415, produced in accordance with the ASTM A240 standard [1], is a stainless steel used widely by Hydro-Québec in the fabrication of hydraulic turbine runners. Containing more than 12 wt % of chromium in its composition this alloy presents a good corrosion resistance in river water. The standard range of chemical properties for this material is presented in

Table 2.1.

Table 2.1 Standard chemical composition of AISI 415 according to ASTM A240 (in wt %) [1]

	C	**Mn**	**P**	**S**	**Si**	**Cr**	**Ni**	**Mo**
ASTM A240-18	0.05	0.5-1.0	0.030	0.030	0.6	11.5-14.0	3.5-5.5	0.5-1.0
Note: When no range is given, the values are the maximum allowed								

AISI 415 has a good weldability and can be heat treated to reach an optimized combination of strength and ductility. The standardized mechanical properties of AISI 415 after heat treatment are presented in Table 2.2.

Table 2.2 Standard mechanical properties of AISI 415 according to ASTM A240 [1]

	***UTS* (MPa)**	***YS* (MPa)**	***El %***	**Hardness BHN**	**Hardness HRC**
ASTM A240-18	795	620	15	302 max	32 max
Note: The exact reported values are the minimum required values unless otherwise specified					

Some guidelines to reach the desired mechanical properties are provided in ASTM A480 [6] as follows:

1. Austenitizing at a minimum temperature of 955°C for one hour per one inch of thickness
2. Air quenching to a temperature below 93°C
3. Tempering between 566°C and 621°C

The duration of each step of heat treatment should be adjusted properly to reach the mechanical properties indicated in

Table 2.2.

Following heat treatment, the resulting microstructure is a mixture of martensite lathes and reformed austenite. The martensitic microstructure was previously revealed by Deschênes [7] in the material AISI 415 (tempered at 620°C), as shown in Figure 2-1.

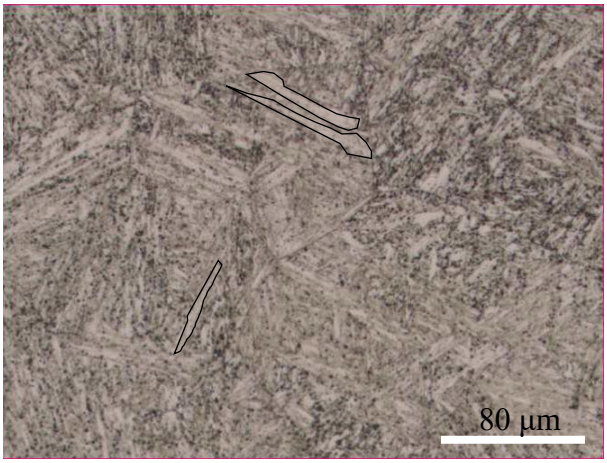

Figure 2-1 Typical microstructure of tempered AISI 415 from Deschênes [7]

In Figure 2-1, three examples of the martensitic lathes are contoured in black. In this figure, only the martensitic constituents is visible since observation of austenite is performed at higher magnifications. Austenite is an elongated phase located between martensite lathes as shown in Figure 2-2, reproduced from Thibault et al. [8], who studied an AISI 415 alloy containing around 17 % reformed austenite.

The mechanical properties of this family of steels (cast and wrought) have been studied extensively, under both static and cyclic loading regimes. Chaix [9] studied the effect of different tempering conditions on the uniaxial tension properties of CA6NM (the cast version of AISI 415). His findings are summarized in

Table 2.3.

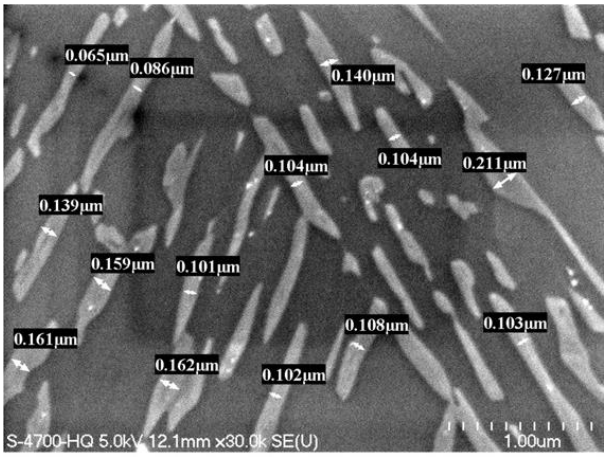

Figure 2-2 Reformed austenite phase in AISI 415 alloy, from Thibault et al. [8]

Table 2.3 Effect of tempering condition on mechanical properties of a 13Cr-4Ni martensitic stainless steel (CA6NM) [9]

	600ºC (2h)	**610ºC (8h)**	**620ºC (2h)**	**550ºC (2h)**
σ_y (MPa)	701	596	552	830
***UTS* (MPa)**	819	777	767	889
Elongation to fracture(%)	21.1	21.6	20.8	17
Reduction of area (%)	69	70	71	---

The *UTS* values in Table 2.3 indicates that AISI 415 is not a high strength steel (*UTS* of less than 1000 MPa) mainly because it has a low carbon content. It can also be observed that longer tempering time leads to lower strength (σ_y and *UTS*) but higher ductility (elongation to fracture). During tempering, carbon precipitates and reformed austenite is created. Both mechanisms are known to reduce the material strength.

2.2 General aspects of fatigue crack propagation

Hydraulic turbines must tolerate variable working conditions (i.e., power output variations [POV], stop/starts [SS] and overloads), implying complex alternating loading cycles for the turbine runners. These variable loadings are schematized in Figure 2-3, as suggested by Hassanipour [10]. As could be seen in this figure, alternative loading on these components are mainly composed of high frequency low amplitude POV and low frequency high amplitude SS loadings. These variable loadings could lead to fatigue.

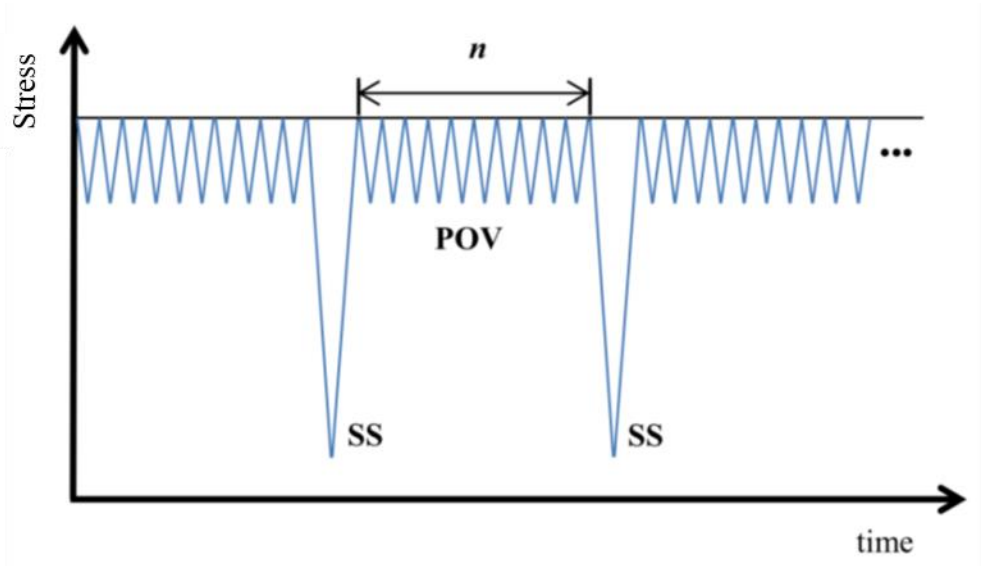

Figure 2-3 Simplified loading cycle of a hydraulic turbine [10]

When designing a turbine for a specific application, three criteria are considered. First, the SS maximum stress should be well below the yield strength of the material. Secondly, based on the damage tolerant approach under monotonic loading, the maximum stress intensity factor (K_{max}) building up at discontinuities should always remain below the critical stress intensity factor (K_c). Third, based on the damage tolerant approach for cyclic loading, the stress intensity range (ΔK), which is building up at discontinuities during cyclic loading (e.g., SS or POV), should remain below the crack propagation threshold.

The damage tolerant approach under both monotonic and cyclic loading has been formulized in the framework of linear elastic fracture mechanics (LEFM). The following section introduces the

fundamentals of LEFM. LEFM under monotonic loading will be discussed in Section 2.2.1, and used to discuss crack propagation under cyclic loading (fatigue regime) in Section 2.2.2.

2.2.1 Linear elastic fracture mechanics (LEFM)

Fracture toughness is expressed in terms of the stress intensity factor through LEFM. This section reviews the fundamentals of LEFM.

A. A. Griffith was one of the pioneers of fracture mechanics. He mathematically expressed the effect of the presence of a crack on the yielding ability of materials. His methodology, based on energy concepts, was proposed for very brittle materials. Others, such as *G*. R. Irwin, extended this approach to ductile materials where the plastically deformed part of a material is small. This method is known as the strain energy release rate (*G*).

However, most efforts that followed focused not on *G* but the concept of stress intensity factor (*K*). Based on linear elasticity theory, the stress intensity for mode I of loading (the most severe from a fracture point of view) is called K_I, and can be characterized by the following formula at the vicinity of an ideally sharp crack:

$$K_I = F\sigma\sqrt{\pi a}$$

Where F is a geometrical factor, σ is the nominal applied stress and a is the length of the crack. There is a critical stress intensity value above which a crack will cause sudden failure of a component. This critical value is a material property and is known as the fracture toughness (K_{Ic}).

The essential assumptions of any equation formulated via LEFM are as follows:

a) The material can be considered a homogeneous, isotropic continuum.

b) Deformation should be elastic and its relationship with stress should be linear.

c) Internal stresses and body forces are negligible (or should be measurable experimentally).

To verify assumption (a), the crack should be long relative to microstructural features such as grain size. To comply with assumption (b), no plastic deformation should occur in the material, however this is not practical due to stress singularity at the tip of a sharp crack. The size of this plastic zone at the crack tip should be small enough relative to all geometric dimensions of the part (including crack length and distance to free surfaces) that it could be neglected [11]. Lastly, assumption (c)

implies that the cracked material should be free from residual stresses such as those produced by machining or welding, or these stresses should be experimentally quantified.

The concept of the crack propagation threshold is applicable not only to monotonic loading but also to a cyclic loading regime, where fatigue can cause failure at a stress intensity amplitude lower than the static toughness of the part. This will be discussed in the following section.

2.2.2 Propagation of long cracks

In a flaw-free sample, most of the fatigue life would be spent in the crack initiation stage. Nevertheless, engineering parts often contain discontinuities such as forging defects and voids. Design and maintenance based on the damage tolerant approach account for the presence of discontinuities in the material. This approach, often based on linear elastic fracture mechanics (LEFM) under a cyclic loading regime, is used to predict the rate of crack propagation.

According to LEFM theory, the propagation rate of an evolving crack (*da/dN*) is driven by variation in the stress intensity factor (*ΔK*). For most metals, the relationship between *ΔK* and the fatigue crack propagation rate (*da/dN*) can be schematized as illustrated in Figure 2-4.

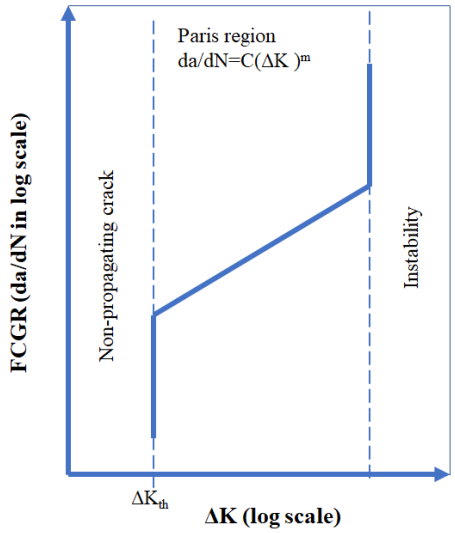

Figure 2-4 Long crack propagation rate dependency on stress intensity factor [12]

In Figure 2-4, the stress intensity threshold (ΔK_{th}) is theoretically the lowest ΔK at which the crack can propagate.

The inclined part of the graph is known as the Paris region and is defined by the Paris equation as follows:

$$\frac{da}{dN} = C(\Delta K)^m \tag{2.1}$$

Where a is the crack length, N is the number of cycles, and C and m are constants which determine the rate of change in the crack propagation rate within the stress intensity range (ΔK). Notably, the relationship of *da/dN* with ΔK in the Paris region is not always linear since phenomena such as crack closure may cause it to deviate from linearity. The importance of crack closure will be discussed in the following section.

2.2.3 Crack closure

The concept of crack closure has been defined as the effect of a zone of residual deformation around the crack tip. It is stated that the crack surface can remain closed for a portion of cyclic loading. Therefore, a concept of effective force range (ΔP) (or ΔK) can be defined by subtracting the portion of cyclic load that has no effect on opening the crack tip. In a tension-tension load cycle, for example with an *R ratio* ($\frac{\sigma_{min}}{\sigma_{max}}$) of 0.1, when the maximum load is applied, the crack will be fully opened, and all stress will be carried by the uncracked ligament of the sample. But at the minimum load, two surfaces of the crack might touch each other due to this effect and compressive stress can rise. Thus, the "crack closure load" is also defined as the load at which the surfaces of a crack begin to transmit stress.

McEvily [13] reviewed the crack closure phenomenon, summarizing the different mechanisms of crack closure under 3 categories. These are shown schematically by Trudel [14] in Figure 2-5 and are described briefly as follows:

- Plasticity induced crack closure is due to formation of a non-negligible plastic zone at the crack tip. This is illustrated in Figure 2-5(a).

- Roughness induced crack closure is due to crack tortuosity. As illustrated in Figure 2-5(b).
- In the case of corrosion-induced crack closure the formation of corrosion products at the crack tip can lead to crack surfaces making contact before complete unloading (Figure 2-5(c)).

Phase transformation induced crack closure is due to volume expansion via a change in the crystal structure. Chaix [9] observed crack closure during FCG of CA6NM steel samples containing different amounts of reformed austenite. The author speculated that transformation-induced plasticity was the reason for this incidence; no direct observations or measurements were provided.

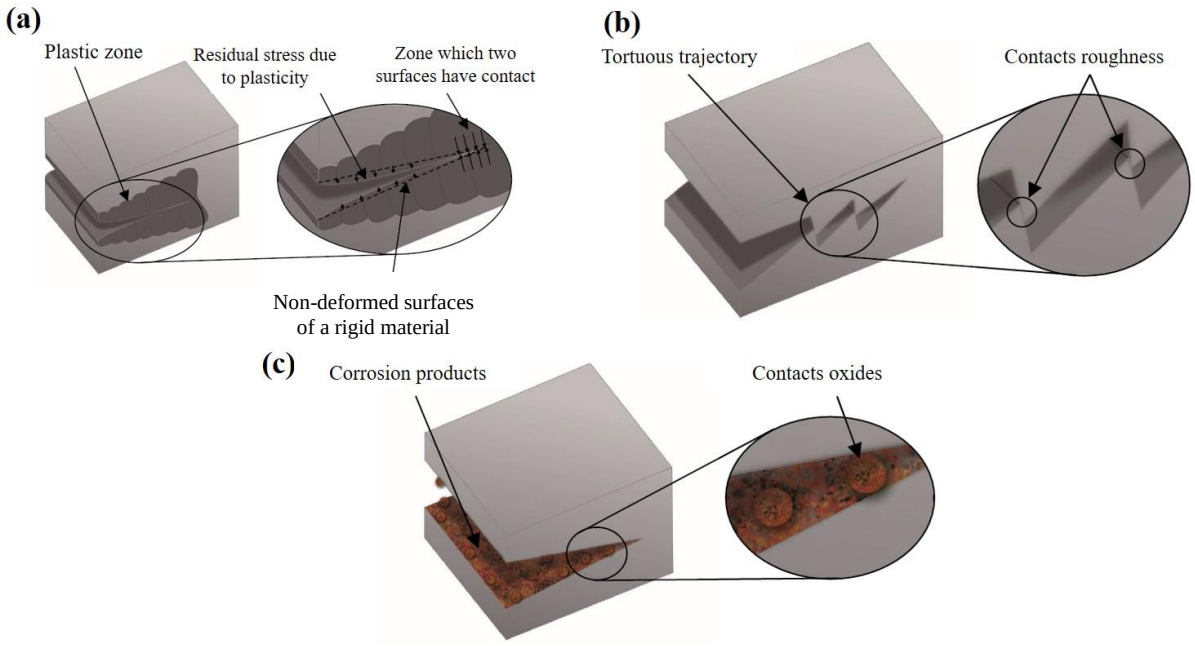

Figure 2-5 Different types of crack closure shown schematically by Trudel [14] (a) plasticity-induced crack closure, (b) roughness-induced crack closure, (c) corrosion-induced crack closure

Standardized recommendations for measurement of crack closure during a fatigue crack growth test are proposed in ASTM E647 Appendix X2 [15]. The minimum load at which a crack will be fully opened (P_{op}) should be measured, and if the P_{op} is less than the applied load (P_{app}), this will indicate crack closure. Crack closure is usually quantified as a ratio of P_{op}/P_{max} (or equally,

K_{op}/K_{max}) where P_{max} is the maximum applied load. Different methods are proposed to indicate when a crack is fully opened, such as eddy current and potential drop, which should be performed during the test. However, the method which is used more commonly is treating the load vs. crack mouth opening displacement that could be performed on the results of a fatigue crack growth test.

2.2.4 Fatigue crack propagation of 13Cr-4Ni

Chaix [9] studied the effect of different tempering conditions on the long crack propagation behaviour of CA6NM (cast version of AISI415) following the ASTM E647 and using compact tensile (CT) samples with an *R* ratio of 0.1. The effect of heat treatment on the FCGR is illustrated in Figure 2-6.

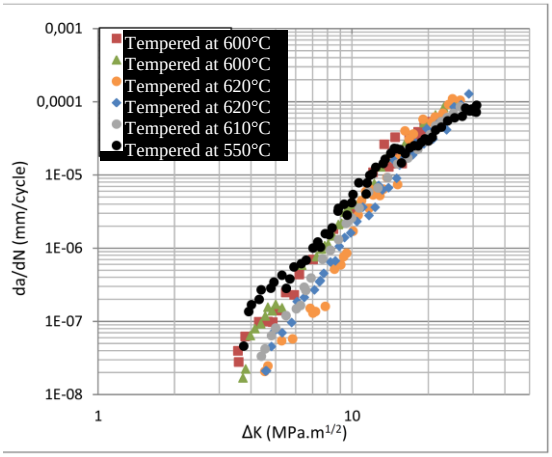

Figure 2-6 Influence of tempering conditions on fatigue crack growth rate of CA6NM, studied by Chaix [9]

Chaix [9] concluded that both the ΔK_{th} and slope of the linear part of the graph are dependent on tempering conditions. To quantify the differences, the Paris equation terms *C*, *m* and ΔK_{th} were fitted to the experimental results (Table 2.4). In short, the higher tempering temperature and time led to a lower crack propagation rate and higher ΔK threshold. This behaviour was explained by more significant crack closure in the microstructure that had been treated at higher temperatures (610°C and 620°C). The crack closure ratio P_{op}/P_{max} at ΔK between 4.5 MPa.m$^{0.5}$ and 6.5 MPa.m$^{0.5}$ is also listed in Table 2.4. Tempering at higher temperature promoted the formation of reformed

austenite which would transform into martensite under the high strain (transformation induced plasticity [TRIP]) at the crack tip. Since martensite is less compact than austenite, a compressive stress field is formed which can cause crack closure and reduce the crack propagation rate.

Table 2.4 Effect of tempering condition on fatigue crack growth behaviour of a 13Cr-4Ni martensitic stainless steel (CA6NM) [9].

	550ºC (2h)	**600ºC (2h)**	**610ºC (8h)**	**620ºC (2h)**
Reformed austenite	1-3%	2.5 - 405%	12- 17 %	12.5-16.5%
ΔK_{th} (MPa.m$^{0.5}$)	3.75	3.64	4.4	4.56
C	2.25x10^{-9}	1.73x10^{-10}	2.17x10^{-10}	4.77x10^{-11}
m	3.21	4.28	4.00	4.60
P_{op}/P_{max}	NA	0.74	0.79	0.82

Akhiat [16], who studied the effect of carbon content on the fatigue crack propagation rate of CA6NM under an *R* ratio of 0.1, also reported that the fatigue crack growth rate is lower for the alloy containing a higher percentage of reformed austenite.

Another important fatigue crack propagation behaviour in 13Cr-4Ni steels was observed by Chaix [9], Trudel [14], and Deschênes [7]. These studies reported that a fatigue crack tends to adopt a partially intergranular path under specific test conditions. Chaix [9] reported the dependency of the fraction of intergranular fracture on the applied ΔK. As can be seen in Figure 2-7, the percentage of intergranular fracture is maximal between ΔK 12 to 15 MPa.m$^{0.5}$. It can cover as much as 70 % of the fracture surface.

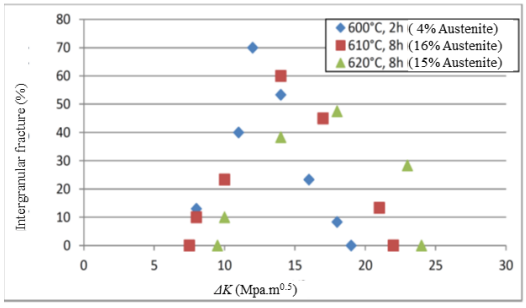

Figure 2-7 Correlation of applied stress intensity factor range on fatigue fracture mode (presented as surface fraction of intergranular fracture). Modified from the work of Chaix [9]

It is frequently reported in the literature that hydrogen embrittlement could cause intergranular fracture in steels [2, 17, 18].

Although this behaviour was not fully explained by the researcher, Chaix [9] proposed that it could be the result of competition between crack propagation and hydrogen diffusion in the metal matrix. The mechanism of hydrogen embrittlement and its influence on fatigue behavior will be covered in the next section.

2.3 Hydrogen embrittlement

Hydrogen embrittlement (HE) of martensitic stainless steels is controlled not only by the atomic hydrogen available in the environment, but also by its adsorption, absorption, diffusion and concentration in the material. In this section, these aspects will be discussed to provide the theoretical foundations for discussion and analysis toward the project objectives.

2.3.1 Hydrogen promotion and absorption

Atomic hydrogen can be present at the metal surface not only in environments containing H_2 gas, but also in environments containing other hydrogen gaseous compounds such as H_2S or H_2O. It can also be evolved in aquatic environments via electrochemical reactions.

In an aquatic environment with neutral acidity, such as river water, a very simplified corrosion reaction can be considered as follows, where *M* represents the metal atom:

Anodic reaction: $M \rightarrow M^{n+} + ne^-$

Cathodic reaction: $2H_2O + 2e^- \rightarrow H_2(g) + 2OH^-$

The cathodic reaction, also known as a hydrogen evaluation reaction (HER), can be broken down into sub-steps to better understand its controlling factors. The following mechanism is suggested by He et al.[2], who studied the HER mechanism on the surface of a 13Cr-5Ni-2Mo super martensitic stainless steel.

In the first step, hydrogen ions are neutralized by electrons released on the corroding metal surface.

$$H^+ + e^- + M \overset{K_1}{\rightarrow} M - H_{ad}$$

Where $M - H_{ad}$ indicates an adsorbed hydrogen atom on the metal surface and K_1 is the rate of this reaction. In the second step, some of these adsorbed hydrogen atoms are combined to form a hydrogen gas molecule with a rate of K_2:

$$M - H_{ad} + M - H_{ad} \overset{K_2}{\rightarrow} 2M + H_2$$

However, a portion of adsorbed atoms can also be absorbed by the metal:

$$M - H_{ad} \overset{K_3}{\leftrightarrow} M + H_{ab}$$

K_3 is a combination of two constants (K_{ads} and K_{des}) representing the rate of successive adsorption and desorption reactions.

The rate of this reaction is largely controlled by the chemistry and surface characteristics of the metal. He et al. [2] performed a specific experiment known as Iyer-Pichering-Zamenzadeh (IPZ) to measure essential kinetic parameters such as K_1 and K_2 for a 13Cr-5Ni-2Mo alloy using a permission test setup. The alloy used in that study was in as-received condition, so the exact heat treatment condition and amount of reformed austenite are not known. The authors reported K_1=6.55x10^3 cm/s and K_2=3.62x10^{-1} mol/(cm^2.s). Although this method could not provide direct measurement of K_3 (K_{ads} and K_{des}), the parameter K was measured. The K value is defined by the following equation and was measured by He et al. [2] as 4.06x10^{-5} mol/(cm^2.s) for this alloy.

$$K = \frac{K_{ads}}{1 + K_{des}(\frac{L}{D_{eff}})} \qquad (2.2)$$

In the above equation, D_{eff} is a diffusion constant, which will be discussed in more detail in Subsection 2.3.3.

2.3.2 Pre-charged and in-situ hydrogen testing strategies

Before proceeding with the literature on hydrogen embrittlement, it should be mentioned that there are two main strategies for investigating the susceptibility of a material to hydrogen embrittlement. In a pre-charged hydrogen strategy, samples are charged with hydrogen using electrochemical reactions or by baking them in a high-pressure atmosphere of hydrogen gas. The pre-charged samples are then exposed to mechanical testing. In an in-situ hydrogen charging strategy, hydrogen

is introduced during the mechanical tests. The pre-charged strategy is representing the internal H while the in-situ strategy is a representation of environmental H sources.

2.3.3 Hydrogen diffusion in metallic matrix

Although hydrogen adsorption is largely determined by the surface properties of a material, the diffusion step is more controlled by trapping. While diffusing, a certain amount of hydrogen is weakly trapped (e.g., by dislocations) or strongly trapped (e.g., by interacting with inclusions) so that the diffused hydrogen concentration in the material may surpass its solubility limit in a trap free structure. Classification of weak (reversible) and strong (irreversible) traps is based on the activation energy needed to release the hydrogen from a given trap. Traps with activation energy lower than 60 kJ/mol are considered weak or reversible traps [2, 17].

It is generally accepted that weakly-trapped hydrogen can cause hydrogen embrittlement. However, a recent study by Murakami and Matsuoka [19] demonstrated that at least under cyclic loading, irreversible trapped hydrogen can also increase hydrogen embrittlement.

Reformed austenite precipitation throughout the martensitic matrix forms a trap with activation energy of 55 kJ/mol. There are two different hypotheses regarding the effect of reformed austenite on a material's susceptibility to hydrogen embrittlement. Some studies (such as Li et al. [20] and Yang et al. [21]) concluded that the presence of reformed austenite (RA) increases an alloy's resistance to hydrogen embrittlement by preventing hydrogen diffusion in martensite. Nevertheless, if austenite becomes mechanically unstable, the hydrogen may be released and become diffusible. In such circumstances, reformed austenite is considered detrimental as it traps and releases a high concentration of hydrogen, favouring embrittlement. Chen et al. [22] showed that under high stress, twinning is likely in reformed austenite, resulting in an augmentation of the material's susceptibility to HE.

The presence of traps in the metallic matrix also influences the diffusion coefficient of hydrogen. When considering traps, the diffusion coefficient of a material is known as the effective diffusion coefficient (D_{eff}). The D_{eff} of a 13Cr-5Ni-2Mo alloy (very close to the chemistry of 13Cr-4Ni) under three different tempering conditions was measured by He et al. [2] using hydrogen permission tests.

The reported values are summarized in Table 2.5. Tempering conditions influenced the amount of reformed austenite, which in turn affected the diffusion coefficient[2]. This is not surprising, since the hydrogen diffusion coefficient in austenite is much lower than in a martensite crystal structure

.

Table 2.5 Effect of reformed austenite content on the effective diffusion coefficient of 13Cr-5Ni-2Mo martensitic stainless steel [2]

	Austenite content (%)	**D_{eff} ($10^{-9}cm^2/s$)**
Single tempering at 590ºC for 1h	0	9.2
Single tempering at 640 ºC for 1h	4.8	6.5
Double tempering at 640 ºC for 1h	10.4	4.7

2.3.4 Hydrogen embrittlement theories

Hydrogen embrittlement is a complex phenomenon. Any change in material, environment or applied stress can significantly change the effects of hydrogen embrittlement. The presence of a doping element (e.g., Mo), inclusions (e.g., Al_2O_3), or secondary phases (e.g., reformed austenite) can either promote or reduce hydrogen embrittlement.

In addition, hydrogen is an atom that is very difficult to detect due to its small size.

Because of this complexity, no unique theory can explain the effect of hydrogen on the mechanical behaviour of steel. Following, three of the most known theories of hydrogen embrittlement will be reviewed which provide a base to discuss the results of this study.

i) Hydrogen-enhanced decohesion (HEDE)

Hydrogen-enhanced decohesion (HEDE), also known as hydrogen-induced decohesion (HID), is based on the assumption that interstitial hydrogen atoms weaken the bonding of metal matrix atoms. Although there is not yet an experimental method that can directly evaluate this hypothesis, it is supported by some evidence. One observation supporting HEDE is that the crack tip opening angle is reduced in the presence of hydrogen. This phenomenon was visualized by Vehoff and Rothe [23], who studied crack propagation in a single Fe-3Si crystal, as shown in Figure 2-8. It is evident in this figure that introduction of hydrogen reduced plastic deformation at the crack tip resulted in a sharper crack. In addition, these authors reported that the crack planes were parallel to (100) and no dimple was

observed on the fracture surface under a hydrogen atmosphere. It can be concluded that introduction of hydrogen led to atomic bond decohesion so that less slip (plastic deformation) could be tolerated, and the crack would propagate by cleavage fracture along crystallographic planes. The sharper crack tip in this case also reduced the possibility of crack arrest due to blunting.

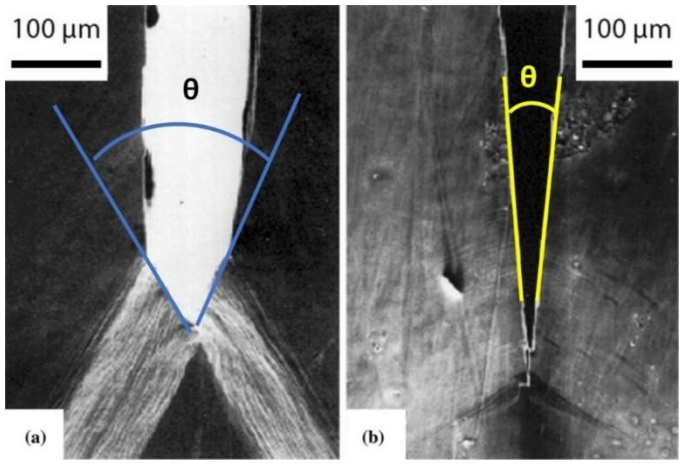

Figure 2-8 Effect of hydrogen on crack tip opening in a single crystal of Fe-3Si. Crack tip opening for sample tested under a) vacuum and b) hydrogen atmosphere (modified from Vehoff and Rothe [23])

HEDE theory is also supported by the general knowledge that hydrogen tends to diffuse toward highly stressed areas, such as the tip of a crack[24].

ii) Hydrogen-enhanced localized plasticity (HELP)

The main hypothesis behind hydrogen-enhanced localized plasticity (HELP) theory is that hydrogen facilitates the mobility of dislocations. In 1998, Ferreira et al. [25] showed that hydrogen can decrease the stacking fault energy (SFE) of a crystal structure. It is common knowledge that the mobility of dislocations is an inverse function of the SFE. If we accept this hypothesis linking the presence of hydrogen and SFE, it can be anticipated that the global effect on material properties will be a reduction of yield strength. Such an effect was described by Jagodzinski et al. [26], who reported

a reduction of 70 MPa on the stress required to plastically deform a tensile sample of pure iron after electrocharging the sample with hydrogen.

iii) Combination of HELP and HEDE

Nagao et al. [27-29] studied the hydrogen embrittlement of high strength carbon steels extensively between 2012 and 2018. These authors used focused ion beam analysis (FIB) and transmission electron microscopy (TEM) observations to investigate the layer just beneath a fracture surface. They explained the occurrence of intergranular and quasi-cleavage fractures using a theory called hydrogen-enhanced plasticity mediate decohesion. Based on this theory, an intergranular fracture can be considered the result of dislocation pile-up at the parent austenite grain boundaries, while "quasi-cleavage" fractures are due to dislocation pile-up at block boundaries (a block being a substructure of martensite, smaller than a grain). The HELP phenomenon would support the presence of dislocation pileups, facilitated by the increased mobility of dislocations. However, once hydrogen atoms are accumulated at the pile-up sites (the grain or block boundaries), embrittlement would follow as proposed by HEDE theory[27].

Bearing in mind the different theories proposed to explain the interaction of hydrogen in iron rich microstructures, Subsections 2.3.5 and 2.3.6 focus specifically on studies reporting the effects of hydrogen on the mechanical behaviour of martensitic stainless steels.

2.3.5 Hydrogen embrittlement of martensitic stainless steels

The literature reviewed in this section reveals that a wide range of martensitic stainless steels (including medium strength steels) are susceptible to hydrogen embrittlement. The influence of reformed austenite in hydrogen embrittlement of martensitic stainless steels is also addressed in this section.

It is reported that high strength martensitic stainless steels are susceptible to H embrittlement under monotonic loading. Shen et al. [30] investigated the hydrogen embrittlement and stress corrosion of a Jethete M152 martensitic stainless steel (yield strength = 1000 MPa) using a slow strain rate testing process. Regarding the severity of hydrogen charging, they reported 70 to 90%

susceptibility to hydrogen embrittlement for this material. Susceptibility to hydrogen embrittlement is a normalizing practice widely used by researchers as a ratio between elongation reduction due to hydrogen embrittlement and initial elongation to fracture without hydrogen. The term monotonic susceptibility to hydrogen embrittlement (MSHE) is used to prevent confusion with susceptibility to hydrogen embrittlement under cyclic loading. MSHE is defined based on the following equation:

$$MSHE = \left(\frac{EL_{UC} - EL_C}{EL_{UC}}\right) * 100 \quad (2.3)$$

Where EL_{UC} and EL_C are elongation to fracture of the uncharged and charged samples, respectively.

Significant susceptibility to hydrogen embrittlement is also reported for medium strength martensitic stainless steels. Kumar et al. [31] reported MSHE of 74.3% for a martensitic stainless steel containing 13% Cr (a chemical composition similar to AISI 415), which had been pre-charged with 9 mg/kg of hydrogen. A change of fracture mode from ductile dimple to brittle intergranular fracture was observed when increasing the hydrogen content of the samples. Moreover, He et al. [2] studied the susceptibility of 13Cr-5Ni-2Mo steel to hydrogen embrittlement under static loading. These authors reported MSHE of 90%, 85%, 75%, and 60% for samples with 10.6% reformed austenite containing 9, 8, 6 and 4.5 mg/kg of hydrogen, respectively[2]. In addition, Fan et al. [18] studied the hydrogen embrittlement of 415 stainless steel under static loading using an external hydrogen charging strategy (electrocharging of hydrogen during a slow strain tensile test). These authors reported MSHE of 61 % and 42 % for samples containing 7 % and 20 % reformed austenite, respectively [18].

It is generally accepted that while diffusible hydrogen plays the essential role in promoting hydrogen embrittlement, reversibly trapped hydrogen (activation energy lower than 60 kJ/mol) is also very effective in terms of a material's susceptibility to HE. Several researchers have investigated this hypothesis. Silverstein and Eliezer [32] studied austenitic, duplex and super martensitic stainless steels using thermal disperse spectroscopy (TDS) to understand trapping sites and their interaction with hydrogen. These authors showed that introduction of hydrogen can enhance the austenite to martensite phase transformation in all of the alloys studied [32]. He et al. [2] illustrated that an increase from 0 to 4.6 % reformed austenite content in 13Cr super martensitic

stainless steel can dramatically reduce the effective diffusion coefficient and flux of hydrogen, while a further increase to 10.8 % has only a slight effect. These authors also suggested that hydrogen is for the most part trapped at the interface of reformed austenite and the matrix rather than in the volume of reformed austenite. He et al. [2] observed that reformed austenite can increase or decrease susceptibility to hydrogen embrittlement depending on the severity of hydrogen charging. A combination of HELP, HEDE and TRIPing is claimed to explain this complex behaviour of 13Cr steels.

2.3.6 Effects of hydrogen embrittlement on fatigue crack propagation

Literature reviewed in this section reveals that FCGR is increased by the presence of absorbed hydrogen. Several parameters that moderate the effect of hydrogen on the fatigue crack growth rate are also reviewed in this section.

A number of studies have demonstrated the susceptibility of fatigue in steel to hydrogen embrittlement. Brüch et al. [33] studied the effect of hydrogen embrittlement on crack initiation and short crack propagation in a martensitic stainless steel (X3CrNiMo13-4). These authors revealed that samples pre-charged with hydrogen demonstrated a higher rate of short crack growth and less of a barrier effect than uncharged samples tested in an air or vacuum atmosphere [33]. They correlated this behavior with the HEDE mechanism [33]. In line with that finding, Rodkey and Jones [5] reported the effect of absorbed hydrogen on the acceleration of FCGR for a medium strength martensitic stainless steel containing 12 %Cr. These authors reported the most significant effect at ΔK=14 MPam$^{0.5}$ and a frequency of 0.2 Hz, as 4 mg/kg of hydrogen led to a fatigue crack growth rate of up to 5 times greater than uncharged samples [5]. The hydrogen enhanced striation formation (HESF) model is a theory based on HELP, proposed by Murakami et al. [34] to explain the effect of hydrogen on accelerating the FCGR of austenitic pre-charged samples as well as the impact of the test frequency on the magnitude of this acceleration. This model was then used by Matsuoka et al. [35] to explain the behaviour of a carbon steel in hydrogen assisted fatigue tests. More recently, in 2018, Matsuoka et al. [36] used this model to discuss the accelerating effect of hydrogen on the fatigue crack growth of a martensitic material (Cr-Mo).

Studies have shown that cyclic susceptibility to hydrogen embrittlement is affected by parameters such as frequency and ΔK. It has been pointed out by researchers such as Rodkey and Jones [5] and

Murakami et al. [34] that FCGR acceleration due to the presence of hydrogen is more pronounced under lower loading frequencies in both pre-charged and in-situ hydrogen charging strategies. Murakami and Matsuoka [19] reported an increase in the crack growth rate as test frequency is decreased. However, they observed that at ΔK 17 MPa.m$^{0.5}$ or lower, the change in frequency has no effect on crack growth rate and in all frequency conditions, the crack growth rate in charged samples is almost 30 times higher than in uncharged samples [19].

Although there has been no study focused specifically on the effect of hydrogen on the FCGR of AISI 415, in studies on other materials such as 304 [34], 4340 [37] and 13Cr [5] steels, the frequency dependency of FCG susceptibility to hydrogen embrittlement has been attributed to the competition between the hydrogen diffusion rate toward the crack tip and the velocity (*da/dt*) of the propagating crack. To understand why hydrogen atoms are diffused toward the crack tip it is essential to review the theory of stress induced diffusion of hydrogen, which is the subject of the following section.

2.3.7 Stress induced diffusion of hydrogen

Several studies have revealed that hydrogen tends to diffuse from the surrounding area toward the crack tip and accumulate there. This diffusion of hydrogen from a dilute area toward a region of high concentration is referred to as hydrogen redistribution or alternately, reversed diffusion, as it occurs in the reverse direction of the concentration gradient. In this subsection, experimental evidence of this phenomenon is reviewed, and the stress induced diffusion mechanism is introduced as a theoretical explanation.

Wang et al. [38] visualized the diffusion of hydrogen toward a crack tip under loading by scanning the surface electrical potential of an H-charged 18Ni maraging steel with scanning kelvin probe force microscopy. Jiang et al. [39] studied the effect of cyclic plastic deformation on hydrogen permission and diffusion in a carbon steel weldment. These authors showed that under cyclic plastic deformation the concentration of diffusible hydrogen increased (by roughly 2 times depending on the severity of the charging condition).

Stress induced diffusion is a proposed theory for reverse diffusion of hydrogen. When a non-stressed sample is charged with hydrogen, a quasi-uniform distribution of hydrogen throughout the

sample is expected. Application of an external mechanical stress leads to a change in this quasi-uniform distribution and H atoms diffuse towards the stress concentration area due to the chemical potential gradient effect. This effect is caused by the expansion of the interstitial spaces of the metallic matrix under elastic tension stress concentration which creates a potential difference between the stressed and unstressed area [40]. Wriedt and Oriani [41] investigated the influence of tensile and compressive stress on the solubility of hydrogen in a ferritic metal matrix. They proposed that hydrogen solubility under a uniaxial stress of σ could be calculated as follows:

$$C_\sigma = C_0 \exp\left(\frac{\sigma \bar{V}_H}{3\mathcal{R}T}\right)$$

Where C_0 is the solubility of hydrogen at zero stress, $\bar{V}_H$ is the partial molar volume of hydrogen, $\mathcal{R}$ is the gas constant (8.314 J mol^{-1} K^{-1}), and T is the temperature in kelvins. A general value of around $2x10^{-6}$ m^3/mol-H is reported as ($\bar{V}_H$) in most steels [42].

Other theories have also been proposed for hydrogen transport in a metal matrix. Tien et al. [43] proposed a stress induced dislocation sweep-in of hydrogen. This theory explains the fast transportation of absorbed hydrogen deep into the plastic zone at the fatigue crack tip. However, this is a short-range phenomenon as dislocations trap only nearby hydrogen atoms. In the case of high cycle fatigue crack propagation, the area of high dislocation density is limited to a small plastic zone at the crack tip. Therefore, in a pre-charged hydrogen strategy this plastic zone can act as a strong trapping site but not as a driving force for long distance hydrogen absorption.

2.4 Summary of the literature review

Throughout the current chapter, a literature review is provided on the specific characteristics of the material under study as well as the principals of fatigue crack propagation and fundamentals of hydrogen embrittlement.

AISI 415 alloy is introduced as a 13Cr-4Ni low carbon martensitic stainless steel with a maximum hardness of 32 HRC and minimum *UTS* of 795 MPa, containing reformed austenite content from virtually 0 % up to 20 %.

The FCGR is introduced as a criterion of the damage tolerance design approach. It is pointed out that this material demonstrates a steady fatigue crack growth rate across a relatively wide range of ΔK, obeying the Paris equation. However, it is also noted that the relationship between the FCGR (da/dN) and ΔK may deviate from this ideal linear relationship due to phenomena such as crack closure. In particular, the fatigue crack growth of AISI 415 is reviewed, and it is noted that in several studies, some evidence of intergranular fracture has been observed, suggesting the possibility of hydrogen embrittlement.

After introducing key terms related to hydrogen embrittlement, HEDE and HELP are presented as two hydrogen embrittlement theories used later in this study. Different methods are used to introduce hydrogen to the test samples, which are categorized as pre-charged and in-situ hydrogen strategies. The charging strategy is a parameter affecting hydrogen embrittlement. Susceptibility to hydrogen embrittlement has been reported not only for high strength steels but also for medium strength (UTS~900 MPa) martensitic stainless steels under both monotonic and cyclic loading. While to the best of the author's knowledge there is no published study on the susceptibility of the FCG of AISI 415 to hydrogen embrittlement, a number of studies on materials similar in chemical composition to AISI 415 suggest a frequency dependency for FCG susceptibility to hydrogen embrittlement. Reviewed studies of other materials recall that hydrogen diffuses toward a highly stressed crack tip area, and its competition with crack growth velocity (da/dt) could be a reason for such a dependency.

Reviewing the literature revealed that:

- The strategy of introducing hydrogen to the test samples in and of itself has an effect on hydrogen embrittlement. Therefore, decision about type of this strategy should be made with precision and this should be calibrated to reach reproducible results comparable to the available literature.
- Despite the medium hardness and strength of this material, significant hydrogen embrittlement under monotonic loading has been reported.
- The susceptibility of the FCG of several martensitic stainless steels with relatively close chemical composition has been proven.

- The susceptibility of the FCG of these materials has been shown to be dependent on the loading frequency.
- Experimental evidence for other materials suggests redistribution and accumulation of hydrogen at the highly stressed area at the crack tip.

The objectives of the current study will now be defined in light of the literature review.

2.5 Objectives of the project

For the purpose of design and maintenance of components that can tolerate the synergistic effects of fatigue and corrosion, the behaviour of cracks propagating in AISI 415 in the presence of hydrogen must be quantified.

However, the authors are not aware of any studies on the effect of absorbed hydrogen on the FCG of AISI 415 as a quenched and tempered martensitic stainless steel with a relatively high percentage of reformed austenite (around 20 %), widely used in the fabrication of hydraulic turbines in Hydro-Québec facilities. Therefore, the present work seeks to answer the research question: *What is the impact of absorbed hydrogen on fatigue crack growth in AISI 415 steel?*

To answer this question and address the knowledge gap on this subject, the following specific objectives (SO) are defined:

SO1: Develop a test method to introduce hydrogen to AISI 415 steel and validate its efficiency and reproducibility.

SO2: Measure the effect of absorbed hydrogen on the FCGR of AISI 415.

SO3: Characterize the impact of absorbed hydrogen on the fatigue fracture mode.

SO4: Theoretically explain the behaviours observed in SO2 and SO3.

The next chapter will describe the research strategy and experimental methods used to fulfill these objectives.

CHAPTER 3 METHODOLOGY

As discussed in the literature review, different factors influence the fatigue crack propagation behaviour of steels. Therefore, to study the impact of hydrogen embrittlement on fatigue crack growth in AISI 415, the effects of these parameters must be isolated and identified. Based on the available literature, the most effective parameters are illustrated in Figure 3-1.

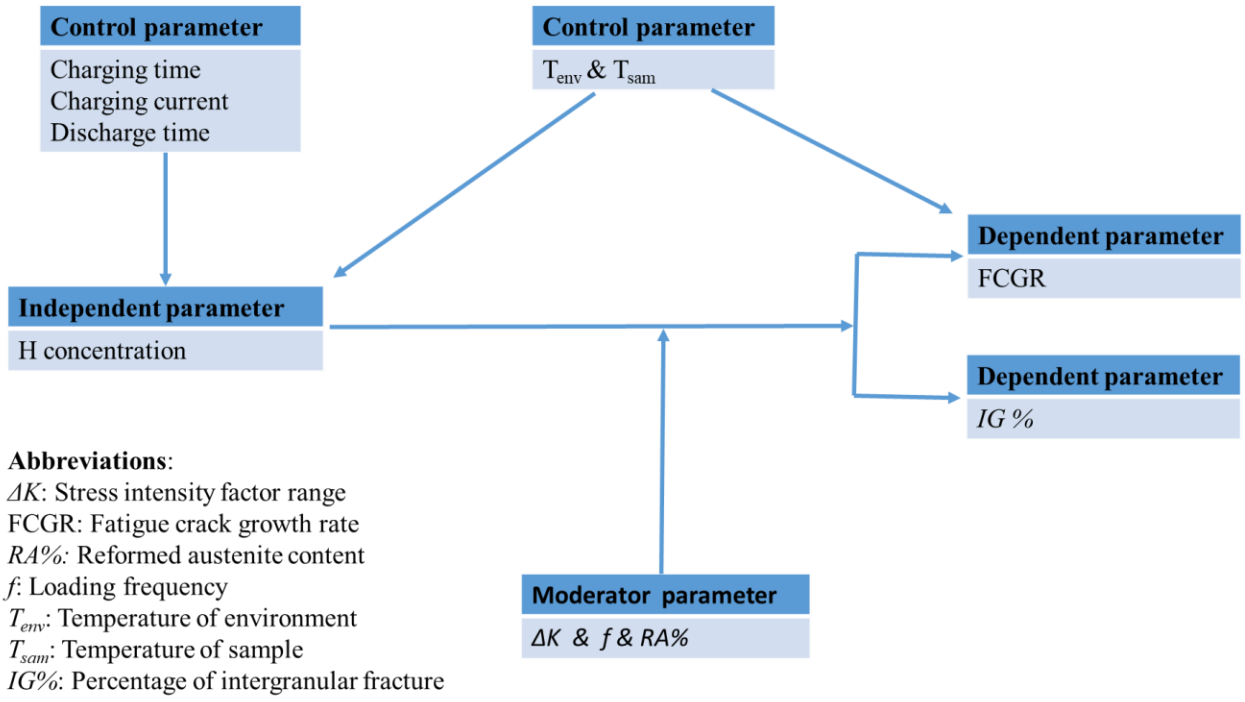

Figure 3-1 Dependent, independent, control and moderator parameters

These parameters fall under the four major categories of independent, controlled, dependent and moderator parameters. In the present study, the independent variable is the hydrogen concentration of test samples. The control parameters, namely the sample and the environment temperature or charging condition, influence both the dependent and independent variables. As this influence was not the focus of this study, these parameters were controlled to remain constant during the experiments. The dependent variables are those used to characterize crack propagation behaviour, namely the FCGR and fracture mode (percentage of intergranular fracture, or IG). These two parameters were measured during and after each test. The moderator parameters influence the causal relationship between the dependent and independent variables. In the scope of this project, these are of two sources: mechanical and material. The stress intensity factor range (ΔK) and

frequency (f) are characteristics of the load cycle (mechanical source). The reformed austenite content (RA %) is a characteristic of the microstructure that can be modified through heat treatment (material source).

As this project aims to reveal the susceptibility of the material under study to hydrogen embrittlement during fatigue, extreme scenarios were tested. To fulfill the subobjectives defined in the previous section, the strategy was to perform fatigue crack growth tests on samples saturated with hydrogen and compare the results to those obtained for the same material that had not been exposed to hydrogen (see Steps D and E in Table 3.1). In order to broaden the mechanical conditions studied and thereby increase the likelihood of detecting the effect of hydrogen on the FCGR, these tests were performed at 2 different ΔKs and 3 loading frequencies. Note that determining no significant effect of hydrogen on the FCGR for one mechanical condition is not a conclusion that can be generalized to other conditions.

As the proposed experimental protocol is innovative, we decided to work with one material containing a fixed amount of reformed austenite (RA%). Based on the existing literature, a microstructure with the maximum amount of austenite was selected. Of the materials commonly used by our industrial partner, our aim was to test the microstructure most susceptible to hydrogen embrittlement.

Table 3.1 links our experimental steps to our specific objectives. It also summarizes key information described in detail in the subsections of this chapter. The first experimental step was dedicated to material characterization (see Step A in Table 3.1). Step B aimed to develop and validate a hydrogen charging methodology. Step C was designed to validate the selected material's susceptibility to hydrogen embrittlement before machining the samples required to perform Steps D and E.

Table 3.1 Experimental plan of the project

Methodology / **Subobjectives**		**SO1** Develop test method to introduce hydrogen to AISI 415	**SO2** Measure effect of absorbed hydrogen on FCGR of AISI 415	**SO3** Characterize impact of absorbed hydrogen on fatigue fracture mode	**SO4** Theoretically explain behaviours observed in SO2 and SO3
Experimental steps	**Test method**				
A. Material characteristics	Microstructural studies, XRD, hardness, uniaxial tensile test	X	X	X	X
B. Measure hydrogen content after different charging method/duration of discharge	Electrochemical H charging	X			X
C. Measure change of elongation due to charging tensile samples with variable H content	SSRT, ASTM G129	X			
D. Measure change in FCGR due to charging CT samples with H	ASTM E647 ΔK=8 &15 (MPa.m$^{0.5+}$ f=0.35, 3.5 & 35 Hz R=0.1)		X		X
E. Indicate fracture mode change due to charging CT samples with H				X	X

The experimental methods and material characterizations will be discussed in detail in the following sections.

3.1 Material characteristics

The material studied is hot rolled AISI 415 (UNS 415000) alloy, a super martensitic stainless steel of the 13Cr-4Ni alloy family.

The material was delivered from the factory in quenched and tempered condition. Chemical and mechanical properties of the as-received material are presented in Table 3.2 and Table 3.3, respectively.

As represented in Table 3.2, the chemical composition of the supplied material is in accordance with the nominal composition of the alloy. In addition, Table 3.3 reveals that the ultimate strength (*UTS*), yield strength (σ_y), elongation to fracture (*El* %) and hardness of the material conform with the mechanical requirements of the standardized 415 alloy.

Table 3.2 Chemical composition of supplied UNS S41500 in wt % and nominal composition as per ASTM A240

	C	**Mn**	**P**	**S**	**Si**	**Cr**	**Ni**	**Mo**
Certificate	0.014	0.8	0.014	0.001	0.5	12.1	4.5	0.6
ASTM A240 [a]	0.05	0.5-1.0	0.030	0.030	0.6	11.5-14.0	3.5-5.5	0.5-1.0
Note: single values are maximum allowable content.								

Table 3.3 Mechanical properties of supplied UNS S41500 (as received) and material requirements as per ASTM A240

	***UTS* (MPa)**	**σ_y (MPa)**	***El* (%)**	**Hardness (BHN)**	**Hardness (HRC)**
Certificate	862	624	20	269	----
ASTM A240[a]	795	620	15 min.	302 max.	32 max.

Although the material was delivered from the factory in quenched and tempered condition, it was heat treated again according to the schedule illustrated in Figure 3-2 in order to promote a microstructure with a maximum amount of reformed austenite.

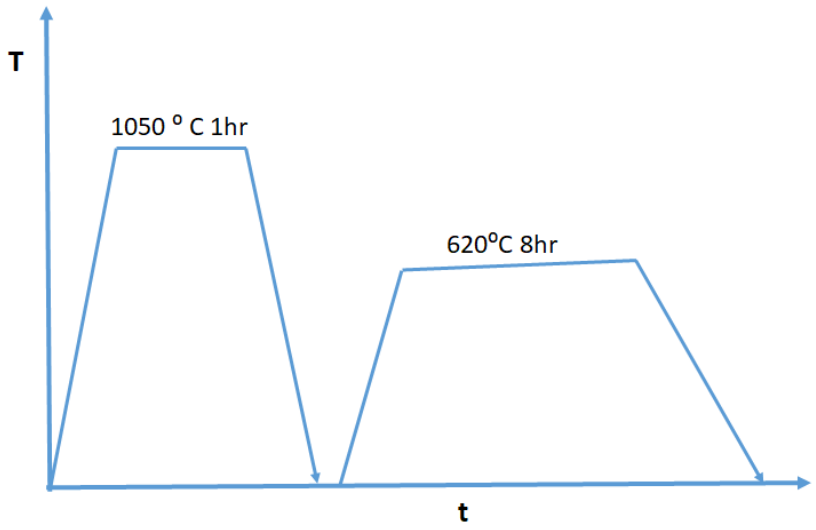

Figure 3-2 Heat treatment cycle of project samples: austenitization at 1050°C for 1 hour followed tempering at 620°C for 8 hours

3.1.1 Hardness test

To check the accuracy of heat treatment, a macro-hardness test was performed on the bulk of the material using a Mitutoyo Rockwell hardness tester on a Rockwell C scale following the ASTM E18 standard test method. The hardness reported was 22.8±0.9 Rockwell C, which is the acceptable range of the ASTM A240 standard (Table 3.2).

In addition, a micro-hardness test was performed to evaluate the effect of mechanical work during machining on the material properties. Micro-hardness was measured using a Vickers hardness scale in accordance with ASTM E384 with an Akashi setup on two parts of a spare CT sample. The first part was tested as machined, whereas the mechanically affected layer of the second part was removed before hardness testing by grinding and chemical polishing in an agitated solution of 30% HCl-30% HNO_3-40% H_2O for 10 minutes. Removal of the mechanically affected layer led to a slight reduction in hardness from 306±8 HV to 289±7.3 HV. This shows that machining has a slight effect on hardness, however, this effect is negligible in fatigue crack growth measurement where any surficial alteration would be eliminated during pre-cracking.

3.1.2 Microstructural characterization

To characterize the microstructure, 5 samples were cut from different parts of the available heat-treated raw block so that both planes (parallel and perpendicular to the rolling direction) could be observed. These samples were supported with hot mounting and ground with SiC paper of 240 up to 1200 grit, then polished with diamond suspension with a particle size of 6, 3, and 1 micron. Different etchants and etching durations were selected based on the ASTM E407 [44] and previous experiments on similar alloys in the research group [7, 9, 14, 16]. The efficiency of these methods to reveal the microstructure was examined practically, and best results were achieved with Fry's modified reagent (1 gr CuCl2 + 50 ml HCl + 50 ml HNO_3 + 150 ml H_2O) and Kalling's reagent #2 (2 gr $CuCl_2$ + 40 ml HCl + 40 ml ethyl alcohol) to reveal the parent austenite grain as well as lathes and other microstructural features.

To measure the parent austenite grain size, standardized methodologies such as counting grains in a specified area could not be used, as complex microstructures of this alloy do not allow all boundaries to be revealed. Therefore, for each grain, five different dimensions were measured as illustrated in Figure 3-3 using ImageJ software, and the average of these was reported as the size

of that grain. This measurement was repeated for around 50 grains on both observed planes and the average of these results was reported as the global grain size for the alloy under study.

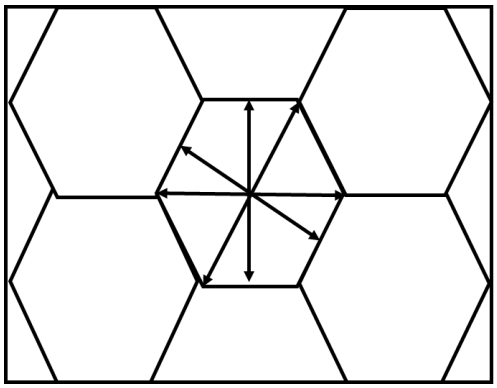

Figure 3-3 Schematic presentation of grain size measurement

3.1.3 Measurement of reformed austenite content

To determine the reformed austenite content, 5 samples were ground using abrasive SiC paper from 240 to 1200 grit. Then, chemical polishing was used to remove at least 50 microns of each surface of the samples. This was a precaution taken to remove the layer of material that can be affected by deformation induced during mechanical polishing. The samples were immersed in an agitated solution of 30 % HCl-30 % HNO_3-40 % H_2O for 10 minutes, and then rinsed successively with water and ethanol.

Quantitative x-ray diffraction (XRD) was performed at IREQ (Institut de recherche d'Hydro-Québec) to measure the austenite phase of the samples. The XRD pattern was obtained using a Bruker D8-Advance diffractometer equipped with a Cu tube with an Ni filter at a voltage of 25 kV and current of 20 mA. Scanning was performed from $2\theta = 40°$ to 140° in 0.05° increments, at a duration of 3-4 seconds on rotating samples. Lastly, Rietveld analysis was performed with Topaz software to determine the amount of austenite phase in the microstructure. To validate the accuracy of the method, two samples with known austenite content in the same range were also tested, determining errors of less than 1% for each measurement. All XRD experiments and results analysis were performed by IREQ. It should be mentioned that the austenite content measured in is a combination of reformed and retained austenite. However, in this document this amount is simply addressed as reformed austenite since the content of retained austenite considered negligible according to the work of Chaix [9].

3.2 Sample preparation

Two sets of samples were machined from the heat-treated block for mechanical testing: tensile samples for the uniaxial tensile test and compact tension (CT) samples for fatigue crack growth tests. Tensile samples were chosen for their ease of manufacturing and testing as compared to CT samples. In addition, these samples require a smaller volume of material than CT samples, which was important to consider within this project. All results in the existing literature on AISI 415 were obtained from tensile tests.

The tensile samples of the first set consisted of 11 cylindrical sub-sized samples with a diameter of 4 mm in accordance with the ASTM E8M standard. Axes of all samples were in line with the rolling direction of the raw material. A tensile sample is schematically illustrated in Figure 3-4(a). A technical drawing is also presented in Appendix A.

The CT samples of the second set were fabricated in accordance with the ASTM E647 standard. A schematic of these samples is presented in Figure 3-4(b). It was determined that the CT sample thickness would be 3mm, in order to be thin enough for fast convergence of H distribution during H-charging to a uniform value, while not compromising the ASTM E399 standard for the plain strain condition (as explained in Section 3.5).

The sample geometry is defined by the terms *W*, *B* and *h*, as illustrated in Figure 3-4. The W chosen is 50.8 for consistency with previous studies in the research group. The criteria for LEFM and plane strain to be applicable are defined by Equations 3.1 and 3.2 in the ASTM E647 and ASTM E399 standards, successively.

$$a, (W - a), B, h \ > \frac{4}{\pi} \times (\frac{K_{max}}{\sigma_y})^2 \tag{3.1}$$

$$a, (W - a), B, h \ > 2.5 \times (\frac{K_{max}}{\sigma_y})^2 \tag{3.2}$$

The crack size value *a* evolved during the tests. It was kept within a range of 1 mm to 49 mm to continuously respect the inequality reported above for a maximum K_{max} of 16.5 MPa. However, in

practice the valid range of crack length is more limited. According to the ASTM E647 standard, 3 mm of pre-cracking is required for a CT sample with h=3mm.

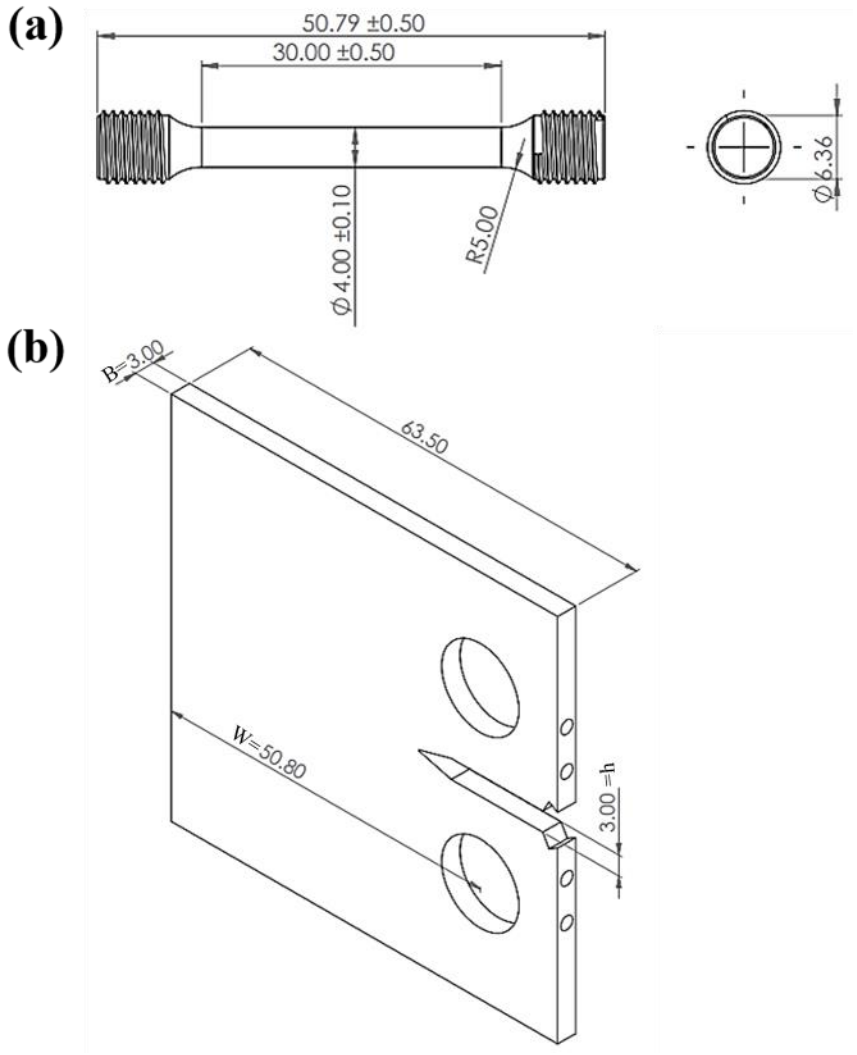

Figure 3-4 Schematic of: (a) SSRT samples; (b) CT samples

The remaining heat-treated block was used for microstructural characterization, reformed austenite measurement and hardness tests.

3.3 Hydrogen charging

Electrochemical methodology was chosen to introduce hydrogen into the material. In this method, a sample is placed in an electrolytic solution and a cathodic current is applied to the sample so that atomic hydrogen evolves on the surface of the sample. This hydrogen can adsorb on the metal surface and diffuse into its structure. This method is safer than working with pressurized hydrogen and it can be easily performed in existing laboratory settings. Nevertheless, it takes more time to reach hydrogen saturation throughout the thickness of a sample. Hydrogen charging before the test was also the preferred option over hydrogen charging while testing. The latter methodology would have involved fatigue testing in an aqueous environment, adding a level of complexity. The downside of charging with hydrogen before testing is the inevitable discharging of hydrogen over time. Diffusible hydrogen will escape a hydrogen rich environment to reach thermodynamic equilibrium.

To fulfill the objectives of the project, we needed to obtain a significant amount of absorbed hydrogen in the samples, ideally with a uniform distribution throughout the sample. The key experimental parameters affecting total hydrogen concentration and distribution are current density, electrolyte chemistry, configuration of charging setup, geometry of the samples (e.g., sample thickness) and charging time.

Current density and electrolyte chemistry were selected as parameters based on the existing literature [18] and previous works in the research group [45]. A three-electrode setup was used to apply a constant cathodic current of 0.1 mA/cm^2 to the sample (cathode) through a 0.1 M NaOH solution (electrolyte). The anode was a tube of AISI 304, and the reference electrode was Hg/HgO-1M NaOH. Configuration of the charging setup was designed according to the sample's shape to provide uniform current density on all surfaces. Cylindrical and rectangular tubes were used as anodes for tensile and CT samples respectively, as illustrated in Figure 3-5. The minimum possible sample thickness was chosen to reduce the charging time needed to reach uniform distribution throughout the sample. According to the criteria discussed in Section 3.5, the minimum allowable thickness for CT samples was 3 mm. Therefore, for tensile samples, the lowest sub-sized standard specimen recommended by ASTM E8 was chosen which has a thickness of 4 mm. Comparable CT sample thickness and tensile sample diameter are prerequisites to estimating their hydrogen content based on results obtained from tensile samples.

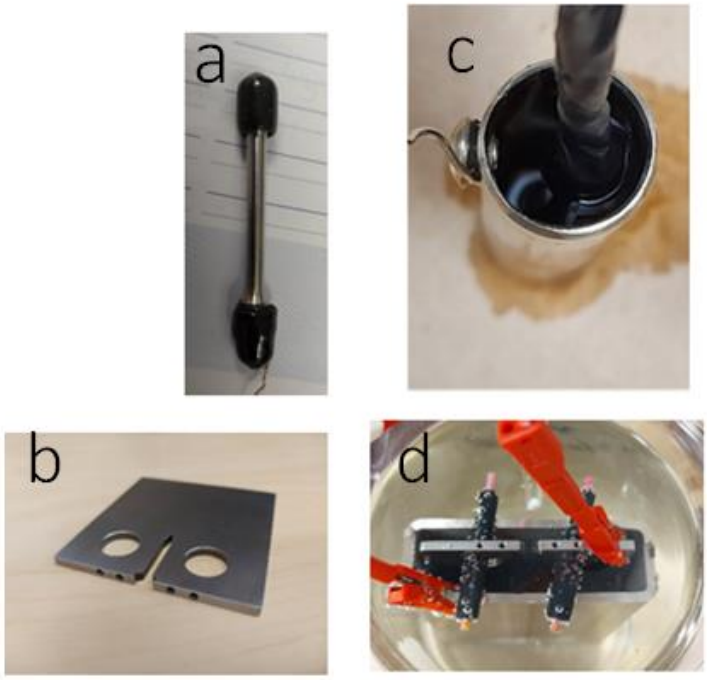

Figure 3-5 Hydrogen charging setup: a) sub-sized tensile sample, b) CT sample, c) installation of sub-sized tensile sample inside anodic tube, d) installation of CT sample inside rectangular anode

However, to quantify the time required to reach hydrogen saturation and evaluate the extent of hydrogen discharge over time, a numerical simulation was performed as described below.

3.3.1 Optimization of charging time

Two-dimensional numerical simulations were used to select the time required to reach uniform hydrogen distribution throughout the test specimens. The relative changes in hydrogen concentration throughout the thickness of the sample were calculated by a team member using a numerical model (see Figure 3-6). Using the effective diffusion coefficient of $5x10^{-13}$ m^2/s (according to the work of He et al.[2]) for a cylindrical tensile sample with a diameter of 4 mm, this calculation is performed for different charging times. The results are presented in Figure 3-6.

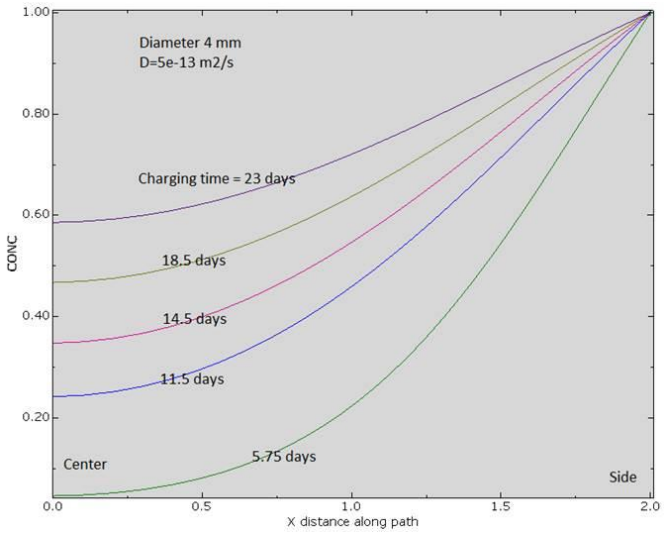

Figure 3-6 Relative hydrogen concentration from surface to centre of cylindrical tensile sample with diameter of 4 mm after different hydrogen charging times (Developed by S. Laliberte-Riverin)

The relative hydrogen concentration is the ratio of instant hydrogen concentration at distance "*x*" from the centre line (C) to hydrogen concentration just beneath the surface (C_0). Therefore, relative hydrogen concentration at x=0 (centre of the sample) could be considered an index of hydrogen uniformity throughout the sample. After 15 to 30 days of hydrogen charging, a hydrogen uniformity of 40 % to 65 % can be expected, as illustrated in Figure 3.6. The charging time is selected to be within this range. However, it was not possible to use a constant charging time for all samples tested due to the restricted availability of labs during the COVID-19 pandemic. Therefore, the tensile samples were charged for 25 to 28 days and the CT samples for 17 days.

This inconsistency in charging time plus the hydrogen escape phenomenon would result in different hydrogen content when testing the samples. In addition, H concentration measurement is a destructive method. To compensate for this lack of information, the hydrogen charge and discharge profile as a function of time were measured as described in Subsection 3.3.2.

3.3.2 Hydrogen measurement

To determine the hydrogen charging profile as a function of time, a cylindrical 13Cr-4Ni sample with a diameter of 5 mm was charged with hydrogen using the abovementioned setup. Slices of the sample were cut at 1, 3, 7 and 14 days, respectively, to measure their hydrogen content. To

determine the hydrogen discharge profile as a function of time, a CT sample was used. Using the same setup, it was charged for 17 days and then cut into two halves. The first half was cut into 4 smaller parts. The hydrogen content of the first part was measured immediately, and the other parts tested after 3, 8 and 13 days, respectively, of storage in ambient conditions. These data were then used to plot hydrogen concentrations versus discharge time.

To evaluate whether geometry affected the hydrogen distribution throughout the test samples, the second half of the abovementioned sample was stored in lab conditions for 14 days and then cut into 3 mm slices parallel to the notch plane. The slice containing the notch plane, the slice right beneath it and a slice further from the notch plane were tested for their hydrogen content, at distances from the notch plane of 1.5, 4.5 and 12 mm, respectively.

Lastly, the hydrogen content of the test samples was measured after tensile and FCG tests. In both cases, half of the fractured samples were tested for their hydrogen content. For one of the CT samples (CT1), the broken sample was cut into 3 mm slices parallel to the fracture surface (notch plane). The slice containing the fracture surface, the one directly beneath it and a slice further from the fracture surface were tested for their hydrogen content, at distances from the fracture surface of 1.5, 4.5 and 12 mm, respectively.

Hydrogen concentration measurements were outsourced to the Centre de métallurgie du Québec (CMQ), a partner of the FATCO project. Samples were kept in a freezer until testing time in order to limit hydrogen escape.

The samples were melted, and a Bruker Elemental GmbH Analyzer was used with nitrogen as the carrier gas and a thermal conductivity detector to measure the hydrogen. Prior to each measurement, a calibration of the apparatus was performed with standard samples containing 0.8 mg/kg, 3.4 mg/kg, and 7.3 mg/kg hydrogen. These experiments and the analysis of results were performed by the CMQ.

3.4 Conventional and slow strain rate tensile tests

Uniaxial tensile testing was performed in accordance with the general requirements of ASTM E8 for the conventional rate and ASTM G129 for the slow strain rate, to fulfill the following two objectives.

- Characterization of conventional mechanical properties of the material to facilitate comparison of results with available literature.
- Evaluation of the impact of hydrogen embrittlement on the monotonic mechanical properties of the material under study.

For the first objective, a conventional strain rate of $2.5x10^{-4}$/s was applied (as per ASTM E8). For the second, a slow strain rate of $1x10^{-5}$/s was applied (as per ASTM E129).

Two samples were tested with the conventional strain rate. Two samples were tested with the slow strain rate in as-machined condition. Three samples were tested after 25 to 28 days of hydrogen charging.

Yield strength (σ_y) is calculated based on the 0.2 % strain method of ASTM E8. Maximum engineering stress is also reported as ultimate strength (*UTS*). To determine the elongation to fracture, an extensometer remained attached to the sample until its breaking point was reached (except for one sample from which the extensometer was detached before necking).

All tensile tests were performed using an Instron tensile machine with a load cell of 20 KN under an ambient atmosphere, except for one sample tested in another laboratory to control for possible errors due to testing equipment.

3.5 Fatigue crack growth test

Fatigue crack growth tests were performed following the ASTM E647 standard test method, using compact tension (CT) samples under constant ΔK. To perform a constant ΔK fatigue crack growth rate test, the maximum load should be reduced as the crack progresses. For this purpose, the crack length was measured automatically using the crack mouth opening displacement (CMOD) compliance method in accordance with ASTM E647. In this method, the CMOD is measured with an extensometer mounted to the notch mouth and converted to crack length following calculations described in detail in this standard. Then, the fatigue machine was programmed to use the calculated crack length to adjust the load so that the ΔK remained constant.

Before the fatigue crack growth tests were performed, the raw samples were pre-cracked in air to reach an initial crack size of 3 mm (in accordance with ASTM E647 criteria). Pre-cracking was

performed at a constant ΔK of 12 MPa.m$^{0.5}$, a stress ratio of 0.1 and a frequency ranging from 10 to 30 Hz.

In this study, 3 CT samples were used to measure the fatigue crack growth rate under ΔKs of 8 and 15 MPa.m$^{0.5}$, an *R ratio* of 0.1 and frequencies of 0.35, 3.5 and 35 Hz, as reported Table 3.4. To minimize the number of samples and dispersion within the results, one CT sample was used to test several conditions. It was first loaded in its as machined and polished condition to measure the FCGR of the raw material. It was then charged with hydrogen (17 days) and tested again.

Table 3.4 Summary of FCG test conditions performed on the three CT samples (CT0, CT1 and CT2)

	Un charged samples		**Charged samples**	
	ΔK15 MPa.m$^{0.5}$	**ΔK 8 MPa.m$^{0.5}$**	**ΔK15 MPa.m$^{0.5}$**	**ΔK8 MPa.m$^{0.5}$**
f=35 Hz	CT0(x2), CT1, CT2	CT1	CT0(x4), CT1(x2), CT2	CT0, CT1, CT2(x2)
f=3.5 Hz	CT0, CT1,	CT1	CT0(x3), CT1(x2)	CT1, CT2
f=0.35 Hz	CT2		CT1, CT2	CT2
x2, x3 and x4 indicate number of repetitions of the test condition on the same sample				

In addition to the automatic crack length measurement using the crack mouth opening displacement compliance, the crack length was also read optically using a microscope. Optical readings are mainly used to prove the accuracy of automatic crack length readings and to adjust test conditions as needed. Automatic readings are used to determine the fatigue crack growth rate as described in the next section.

3.5.1 Fatigue crack growth rate measurements

Different data acquisition intervals for reading crack length were tested to determine the best practice. At first, this interval was set to every 250 µm of crack propagation in compliance with the ASTM E647 standard. However, the data gathered using this interval was not sufficient for measurement of the crack growth rate. Therefore, the acquisition intervals were set to a fixed number of cycles (every 5 000 cycles) rather than a specific length of crack propagation.

In this context, for each condition, the crack propagation rate was calculated using the two following methods.

For each test condition, the first 10 000 load cycles were used to stabilize crack propagation. Then, the crack length versus the number of cycles was recorded and used to evaluate the FCGR. The results were reported in graphs such as the one presented in Figure 3.5, and a linear fit was applied to the data using the least-squares method. The slope of this linear fit was reported as the mean crack growth rate of a specific test condition.

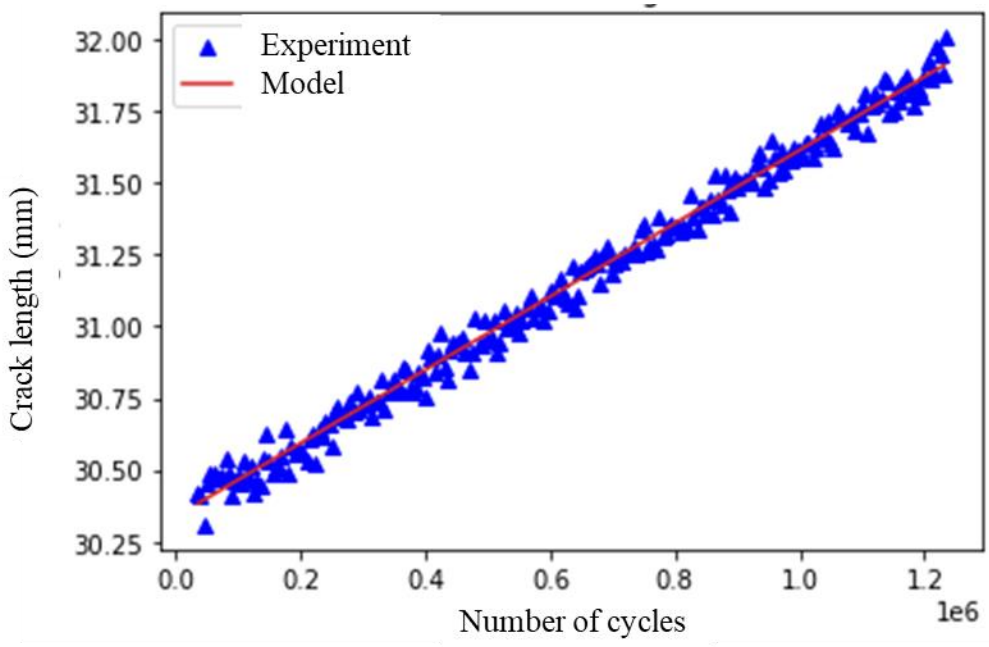

Figure 3-7 An example of the plot of crack length versus number of cycles and fitted linear model

In addition, the average FCGR was calculated again by dividing the difference in crack length (length at end minus length at beginning of process) by the number of elapsed cycles.

3.5.2 Crack closure measurement

During the fatigue crack propagation test, the applied force and crack mouth opening displacement (CMOD) were recorded for several specific full cycles of loading under each test condition.

The CMOD versus load recordings were used to calculate the crack closure load (PCL). An example of the CMOD versus load graph is shown in Figure 3.6. The deviation in linearity at low loads is attributed to crack closure. To systematically identify the point of deviation with linearity, the procedure proposed in ASTM E647 Appendix X2 was followed. An offset of 4% was selected

as it provided the most robust result. A Python code was used to automatize the calculation to all load cycles recorded during a test. Using this code, the crack closure of each recorded cycle is measured in terms of the closure load (P_{Cl}) and PCL/Pmax (Pmax being the maximum load of that cycle). The results are illustrated on different plots and a mean value is also reported as a representative of the crack closure of related test conditions.

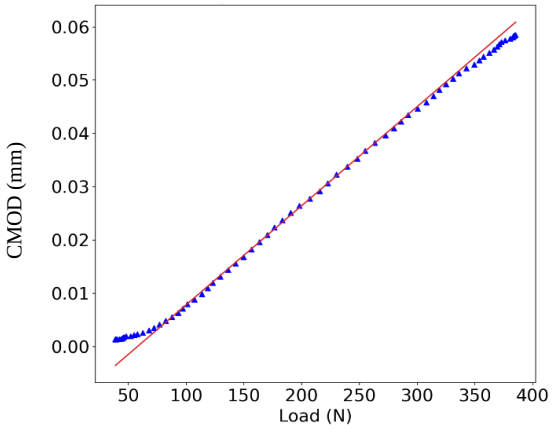

Figure 3-8 An example of a CMOD-Load plot, showing the decreasing part of a load cycle and the model fitted to its linear part

3.6 Fractography

Overall views of the fractured surfaces resulting from the tests performed on the tensile and CT specimens were obtained using a digital optical microscope. In addition, higher magnification images were gathered using scanning electron microscopy (SEM).

CHAPTER 4 RESULTS

This chapter is dedicated to the tensile test results verifying that AISI 415 is susceptible to hydrogen embrittlement (SO1).

4.1 Monotonic loading test results

One specific objective of this project is to verify whether AISI 415 with the specific microstructure previously described is susceptible to hydrogen embrittlement. In addition, in order to draw comparisons with the existing literature, we needed to determine the mechanical properties of the material.

The results of the slow strain rate tensile tests performed on the hydrogen-charged (C1 to C3) and uncharged (UC1 and UC2) AISI 415 samples are presented in Table 4.1 and Figure 4-1.

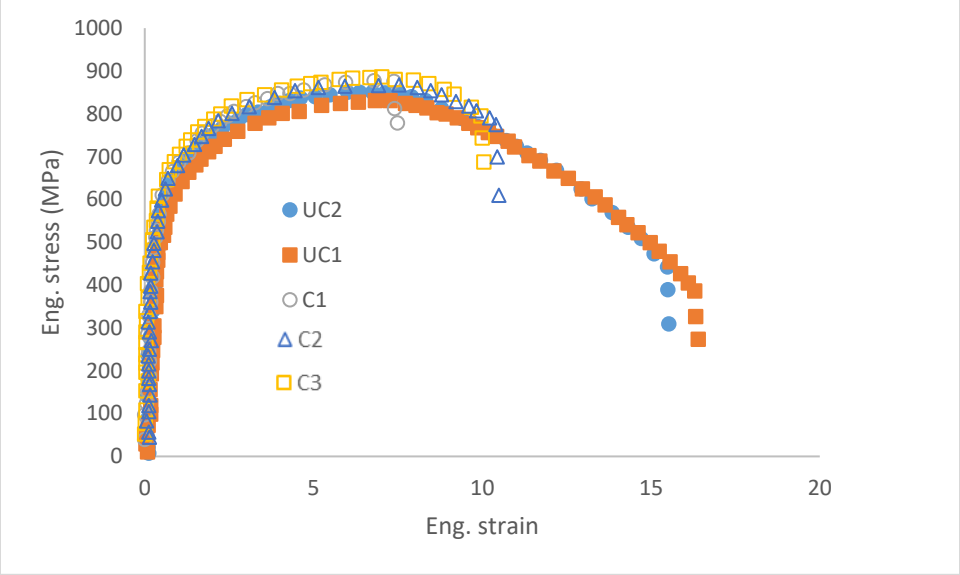

Figure 4-1 Tensile test results as engineering stress vs engineering strain for charged (C1 to C3) and uncharged (UC1 and UC2) samples of AISI 415 under slow strain (10^{-5} s^{-1})

Table 4.1 SSRT results for H-charged and uncharged 415 stainless steel

Sample condition	Charging duration (days)	[H] mg/kg	Elongation (%)	σ_u (MPa)	σ_y (MPa)
C 1	28	13.5	7.5	874	587
C 2	28	9.2	10.7	863	595
C 3	25	10.0	10.1	877	573
UC 1	0	~1.5	16.5	822	523
UC 2	0	~1.5	16	844	534

The test results of the SSRT for charged and uncharged samples reveals that while the changes in the ultimate and yield strengths after charging is negligible, the elongation to fracture is significantly reduced. A linear relationship is recognized between the total content of internal H and elongation to fracture under monotonic loading, as shown in Figure 4-2.

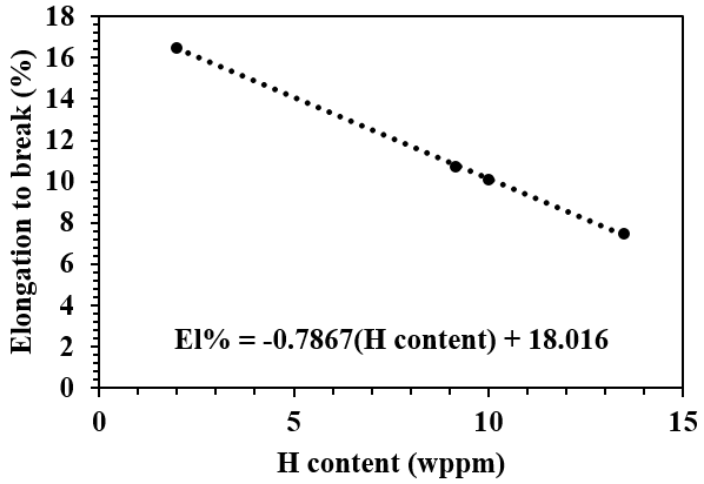

Figure 4-2 Elongation to fracture of SSRT samples with different hydrogen content

A fractographic analysis of tensile test specimens is presented in Figure 4-3. The fracture surface of the raw material presented dimples over its entire surface, representing a ductile failure mechanism. Samples containing 9.2 mg/kg and 10 mg/kg of hydrogen presented fracture surfaces covered with a mixture of dimples and quasi-cleavage facets. Lastly, the sample containing the highest amount of hydrogen was covered in a combination of intergranular facets and cleavage planes. This last sample had the smallest elongation at fracture (7 %). These observations combined with a significant reduction in ductility are direct proof of the material's susceptibility to hydrogen embrittlement. It also confirms that the hydrogen charging methodology was successful.

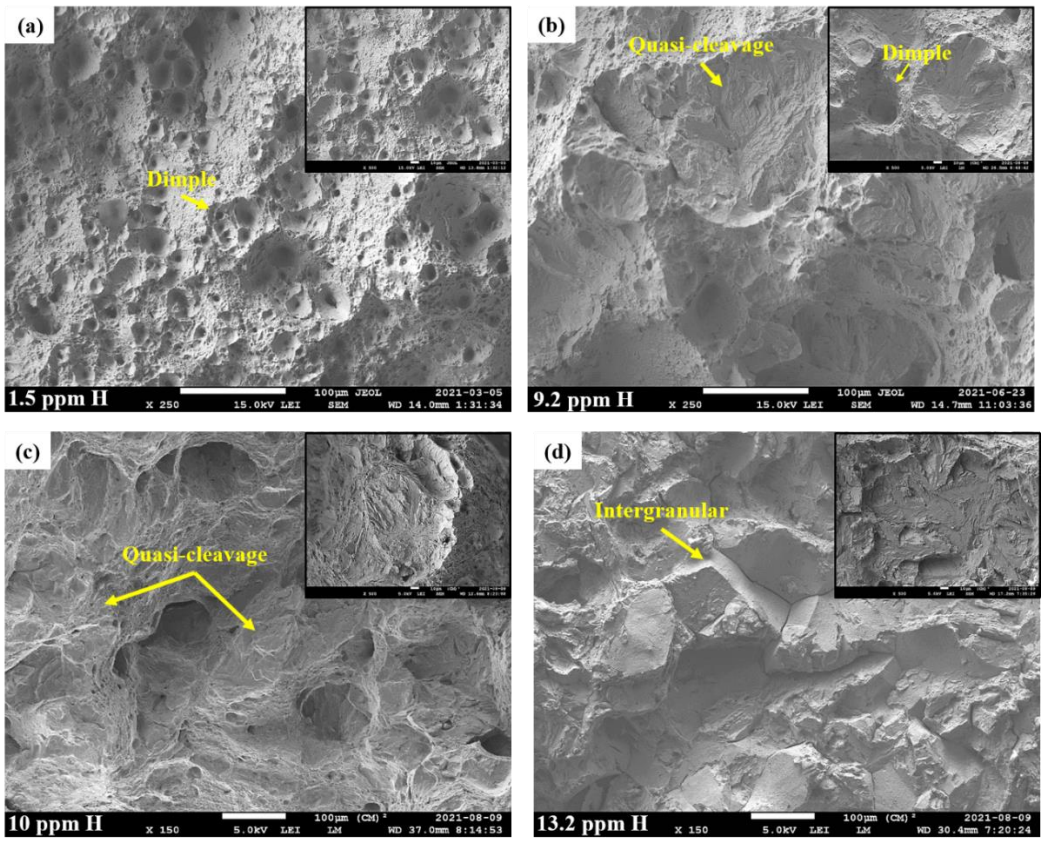

Figure 4-3 Fractography analysis after SSRT test for H of (a) 1.5 mg/kg (raw material), (b) 9.6 mg/kg, (c) 10 mg/kg, and (d) 13.6 mg/kg

CHAPTER 5 ARTICLE 1: EFFECT OF HYDROGEN ON THE FATIGUE CRACK GROWTH BEHAVIOR OF A TEMPERED MARTENSITIC STAINLESS STEEL

Authors: D.Harandizadeh Najafabadi, A.Barabi, D.Thibault, M.Brochu,

This chapter presents the crack propagation behaviour of the raw AISI 415 versus AISI 415 charged with hydrogen (SO2, SO3 and SO4). This is presented in the form of a scientific paper submitted to *Engineering Fracture Mechanics* on July 08th, 2022. This is a modified version of the original paper considering the comments of the jury members.

Abstract

The effect of pre-charged al hydrogen (H) on FCGR and fracture mode is studied for a 415 martensitic stainless steel. Specimens are electrochemically charged with H and tested at constant stress intensity factor ranges (ΔK = 8 MPa.m$^{0.5}$ and 15 MPa.m$^{0.5}$) and three cyclic loading frequencies (f = 35 Hz, 3.5 Hz and 0.35 Hz). The results reveal that H in concentration as low as 4 mg/kg, doubles the FCGR at a specific ΔK and frequency. Results also indicate that, in addition to the concentration of hydrogen, the sensitivity of the FCGR to hydrogen is influenced by the load frequency, the level of ΔK and crack closure. Hydrogen enhanced decohesion (HEDE) and stress induced diffusion (SID) theories are combined to explain the effect of the studied variables. This original model is capable of explaining the higher FCG susceptibility to H embrittlement at ΔK =15 MPa.m$^{0.5}$ (when compared to results obtained at ΔK = 8 MPa.m$^{0.5}$) and at the lowest loading frequency tested (0.35 Hz).

Keywords: Martensitic stainless steel; Reformed austenite; Internal hydrogen; Hydrogen embrittlement; Fatigue crack growth

5.1 Introduction

Low carbon martensitic stainless steels containing more than 12 % Cr and around 4% Ni have a good combination of strength (800 MPa – 1000 MPa) and ductility (20 %) in quenched and tempered condition [1]. Their good corrosion resistance and weldability also makes them candidates for welded assembly such as hydraulic turbine runners [2].

Turbine runners experience both fatigue and corrosion damages during their service[3]. When corrosion takes place, the cathodic reaction releases hydrogen that can eventually be adsorbed and diffused into the material, raising the risk of hydrogen embrittlement. This H can dissolve in the material crystal structure through interstitial sites (diffusible H), or it may get trapped at crystal heterogeneities such as grain boundaries, dislocations, or precipitates (trapped H). Both diffusible and trapped H raise the risk of H embrittlement incidence. Although H embrittlement is usually a concern for high strength steels (tensile strength over 1000 MPa), it was also reported for lower strength steels [46, 47]. Hydrogen embrittlement of tempered 13%Cr-4%Ni was specifically studied by Fan et al. [18] who revealed a 40 % reduction in ductility when the material was exposed to hydrogen during a tensile test.

While irreversible H traps may decrease the potential of embrittlement, reversible H traps (with low activation energy) may release H under working condition becoming an internal source of H. Reformed austenite is such trap and in the 13%Cr-4%Ni tempered stainless steels its proportion can be as high as 20%. The complexity related to the presence of reformed austenite is its mechanical instability. Under a critical amount of strain, it can transform into martensite, releasing the trapped hydrogen into the martensitic matrix.

Besides reducing the material's ductility, literature shows that hydrogen can enhance the FCGR of high strength steels, low carbon martensitic steels and even austenitic stainless steels. Tanaka et al. [48] reported an increase of the FCGR by 30 times after charging a Cr-Mo steel (SCM435, hardness of 330 HV) with 0.3 to 0.5 mg/kg of hydrogen. Tsay et al. [6] reported an increase in the FCGR of over 10 times from experiments conducted on 304 austenitic stainless steel when comparing the results of tests performed in laboratory and hydrogen rich environments. To complement, Rodkey et al. [5] have studied the effect of internal hydrogen on the FCGR in a martensitic stainless steel containing 12% Cr. They reported, for a ΔK of 14 MPa.m$^{0.5}$ and a frequency of 0.2 Hz, 5 times increase in the FCGR when specimens were charged with 4 mg/kg of hydrogen. They also reported that the effect of H on the FCGR is more significant when tested at low loading frequency.

Different theories were proposed to explain the effect of hydrogen on the mechanical properties of steels. Hydrogen enhanced localized plasticity (HELP) and hydrogen enhanced decohesion (HEDE) are two such theories. HELP is based on two assumptions: i) H increases the strain planarity (decreasing dislocation climbing to other planes) and ii) hydrogen interacts with

dislocations and facilitates their in-plane slip leading to slip localization. This localized plasticity can promote crack propagation due to enhanced shear decohesion [49]. Nevertheless, the HELP theory cannot explain the loss of ductility which is the main concern when referring to H embrittlement. The HEDE is based on the hypothesis that a critical amount of hydrogen can lead to the decohesion of atomic bonds [50]. This weakened atomic cohesion may lead to cleavage or intergranular fracture depending on the hydrogen spatial distribution in the material and the stress state.

A combination of the HELP and HEDE theories is sometimes used to explain specific mechanical behaviors. Fan et al. [18] used a combination of HELP and HEDE to rationalize the coexistence of intergranular and quasi-cleavage features on the fracture surfaces of tensile test coupons manufactured from a 415 steel containing reformed austenite. Murakami et al. [34] proposed a model named hydrogen enhanced striation formation (HESF) based on the HELP theory to rationalize the acceleration of fatigue crack growth in austenitic specimens pre-charged with hydrogen, and the effect of frequency on this behavior. They also proposed that hydrogen concentrates at the crack tip due to stress induced diffusion mechanism. This would explain the synergetic effect of the crack propagation rate and the diffusion rate. This model was later used by Matsuoca et al. [37] to discuss the impact of hydrogen on the propagation kinetic of a fatigue crack in a Cr-Mo martensitic steel. The model well explained the frequency dependency of the FCGR susceptibility to H embrittlement, but it could not be used to rationalize the intergranular and cleavage features observed on the fracture surfaces.

According to the information gathered from the literature, there is a gap of knowledge to anticipate and explain the effect of hydrogen on the fatigue crack growth of low and medium strength steels. In addition, the hydroelectric industry is willing to improve the comprehension of fatigue corrosion behavior of martensitic stainless steels to support inspection and maintenance plans. Therefore, the present research project aims at measuring and explaining the effect of hydrogen on the FCGR in AISI 415 manufactured according to ASTM A240. ASTM E647 testing procedure is used to quantify the growth rate of fatigue cracks propagating in compact tension (CT) specimen uncharged and charged electrochemically with hydrogen. Tests are performed at two ΔK and three frequencies. In the discussion section, a novel model supported by HEDE and SID theories is proposed to rationalize the results.

5.2 Materials and Methods

5.2.1 Material characterization

The material is AISI 415 stainless steel with the chemical composition listed in Table 5.1. The material is austenitized, quenched and tempered at 620℃ for 8 h (as per ASTM A480 [6]) to reach a yield strength (σ_y) of 584 ± 16 MPa, an ultimate strength of 856 ± 16 MPa and a hardness of 22.8 ± 0.9 Rockwell C. Its microstructure is mainly martensitic as shown in Figure 5-1.

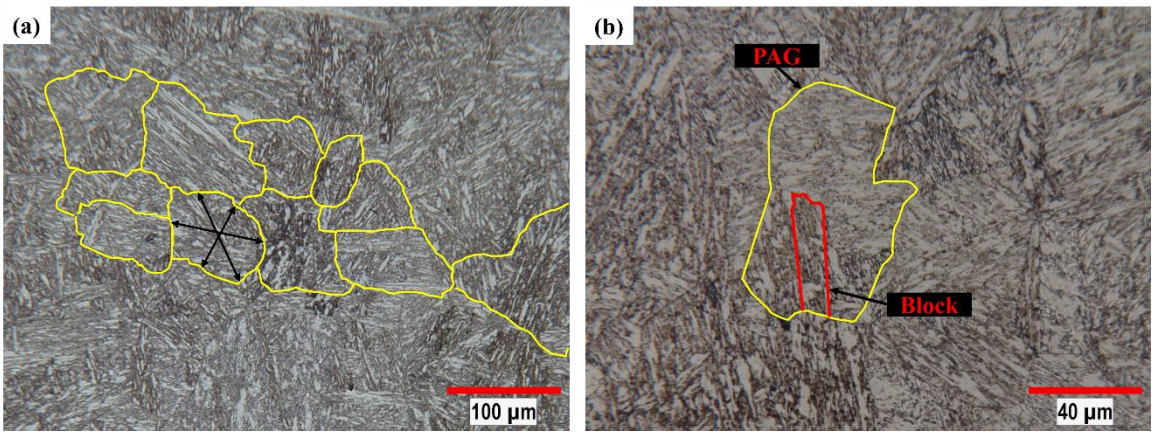

Figure 5-1 Microstructure of 415 stainless steel heat treated at 620℃ for 8 hours showing: (a) General martensitic structure with PAGs contoured in yellow. (b) PAGs and blocks shown with yellow and red solid line respectively. The microstructure was revealed with a Kalling's reagent having a chemical composition of 1 gr $CuCl_2$, 40 ml HCl, 40 ml ethanol. Prior to etching, the sample was mechanically polished up to 1 µm using a diamond solution.

In Figure 5-1 *(a)*, the martensite is structured within parent austenite grains (PAG) contoured in yellow. The PAG average size is 60 ± 15 µm. The diameter was estimated over 40 grains by averaging, for each grain, 3 diameters measurements distributed equally over the grain circumference, such as demonstrated by the black arrows in Figure 5-1(a). A standard grain measurement method, such as ASTM E112 [51] could not be used due the heterogeneity in the

grain boundary visibility over a micrograph. Within each PAG, the martensite is organized in blocks as illustrated in Figure 5-1 (b).

Table 5.1 Chemical composition of AISI 415 stainless steel in wt%

	C	Mn	P	S	Si	Cr	Ni	Mo
Material certificate	0.014	0.8	0.014	0.001	0.5	12.06	4.4	0.6
ASTM A240-18*	0.05	0.5-1.0	0.030	0.030	0.6	11.5-14.0	3.5-5.5	0.5-1.0

*** Note: Maximum amount unless a range is specified**

The reformed austenite could not be revealed by optical microscopy because it is finely distributed between martensite laths and it is few micrometers in size [8]. Therefore, X-ray diffraction (XRD) analysis was performed. Prior to this measurement, a final step of chemical polishing was executed using a mixture of 30 % HCl+40% HNO_3+10% H_2O. The purpose of this step is to eliminate residual strain known to influence the measurements of austenite. The XRD results were processed using the Rietveld method [52]. Five measurements were performed on 5 samples, resulting in an average austenite content of 19.5 % ± 0.8 %.

The raw material content in hydrogen was also measured. An average hydrogen content, over 3 samples, of 1.24 ± 0.19 mg/kg is reported. The methodology of hydrogen measurements is reported in *section 2.2*.

5.2.2 Hydrogen content measurements

The content of H in the alloy was measured by melting a sample of about 20 mm^3 in an electrical furnace. While melting, a flow of nitrogen gas (purity of 99.999%) is used to carry the released hydrogen to a thermal conductivity detector (TCD). The thermal conductivity reading is used to calculate the content of hydrogen released from the sample. The H analyser is calibrated with 3 samples of known hydrogen content (0.0, 3.4 ± 0.6 and 7.3 ± 0.6 mg/kg) before each set of

hydrogen measurements. Whenever possible, the measurements were repeated. In these cases, an error bar is reported to indicate the standard deviation in the test results.

5.2.3 Hydrogen charging methodology

Some of the samples were H charged electrochemically using a galvanostatic method (constant current density) involving 3 electrodes: the specimen as the cathode, a stainless steel AISI 304 tube for the anode and a Hg/HgO-1 M NaOH for the reference electrode. A tube of rectangular cross section was used for the anode to conform to the shape of the compact tension (CT) specimen (see Figure 5-2 for the geometry of the CT specimen. The specimen was introduced inside the tube providing a uniform distance of 6 mm between all four sample surfaces and the inner tube surfaces (anode). A constant cathodic current density of 0.1 mA/cm^2 was applied within a 0.1 M NaOH solution. For all the experiments lasting more than 3 days, the solution was renewed every 3 days and its temperature was recorded constant at 23ºC. The charging time was optimized using the results of the charging experiments presented in the section 2.4 below.

5.2.4 Determination of H charge and discharge profile

To determine the time-dependency of H concentration while charging and discharging 2 sets of hydrogen measurements have been conducted.

To characterize the hydrogen charging profile, a 13%Cr-4%Ni dummy sample containing the same amount of reformed austenite was charged with the same setup used to charge the CT specimens. Slices of the dummy sample were cut after 1, 3, 7 and 14 days of charging to measure the hydrogen content according to the procedure described in *section 2.2.*

To characterize the hydrogen discharging profile, a reference CT specimen (CT_{ref1}) was charged for 17 days and cut into pieces to measure the hydrogen content at different times: immediately after charging (t = 0 day) and after 3, 8 and 13 days.

5.2.5 Determination of H spatial distribution

To investigate the spatial distribution of hydrogen at different distances from the notch plane, two additional sets of hydrogen measurements were performed. One reference CT (CT_{ref2}) was charged for 17 days then cut into 3 mm thick slices parallel to the notch plane. The 1st slice contained the notch plane, the 2nd and 3rd slices were 3 mm and 10 mm beneath. Hydrogen measurements were performed on each slices using the methodology described in *section 2.2*. Another set of hydrogen measurements was performed on a CT specimen (CT1) tested in fatigue and charged with hydrogen for 17 days while testing (details of the testing conditions are provided in *section 2.5*). After test completion, three slices were cut from half CT1 specimen using the cutting pattern described above. H content in each slice was measured using the methodology described in *section 2.2.* Results of H distribution in the CT_{ref} and CT1 specimens will be presented in the *discussion.*

5.2.6 Fatigue tests

Crack propagation tests were performed according to ASTM E647 methodology, using compact tension specimens (CT). Five CT specimens (CT_{ref1}, CT_{ref2}, CT0, CT1 and CT2) were machined according to the dimensions given in Figure 5-2, with a sample length (*W*) of 50.8 mm. The CT specimen thickness, *B*, was chosen thin (*W/B* = 17) to reach a uniform concentration of hydrogen rapidly during the electrocharging process.

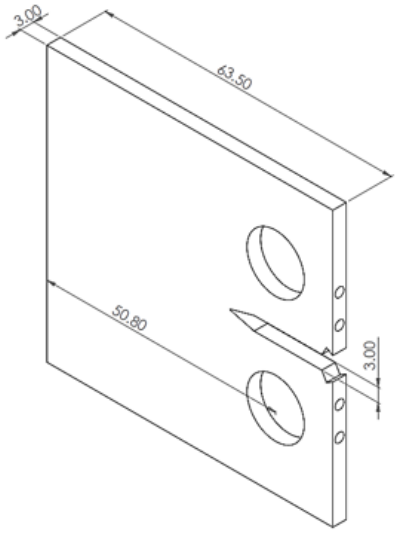

Figure 5-2 Geometry of the CT specimens. All dimensions are in mm.

FCG tests were performed on a servo-hydraulic test machine equipped with 20 kN load cell. Three CT specimens (CT0, CT1 and CT3) were pre-cracked at a constant ΔK of 15 MPa.m$^{0.5}$ to reach an initial crack length of about 3 mm. The fourth CT specimen (CT_{ref}) was used for the hydrogen charging profile characterization as described in *section 2.4*. The FCG tests were then performed in blocks of constant *ΔK-hydrogen content-frequency* as described in Table 5.2B. The ΔK was maintained constant by reducing the load as the crack length progressed. The crack length was monitored continuously using the compliance method according to the procedure described in appendix A5 of the ASTM E647. The accuracy of the crack length calculated based on the compliance was verified regularly by optical readings. These were taken on each lateral surfaces, at every 250 µm of crack advancement. The content of hydrogen was modified by charging the specimens for the duration specified in the columns *H charging (days)* of Table 5.2. During a test, up to 12 test blocks were applied to a specimen (see the descriptions in Table 5.2). When the ΔK was reduced from 15 MPa.m$^{0.5}$ to 8 MPa.m$^{0.5}$, the crack was forced to propagate over at least 1 mm to exit the monotonic plastic zone. The same precaution was not taken when increasing the ΔK. The loading frequency was modified without specific precaution. The material behavior was studied at 35 Hz, 3.5 Hz and 0.35 Hz. To mitigate the potential effect of crack geometry (length, asymmetry, curvature), some test blocks were repeated at different crack length and on several specimens. Tests blocks performed in the same conditions are highlighted by a given color in Table 5.2.

Table 5.2 Test condition protocol for each CT specimen. Colors highlight test blocks performed in the same conditions.

CT0				CT1				CT2			
Crack length (mm)	**ΔK (MPa.m$^{0.5}$)**	**F (Hz)**	**H charging (days)**	**Crack length (mm)**	**ΔK (MPa.m$^{0.5}$)**	**F (Hz)**	**H charging (days)**	**Crack length (mm)**	**ΔK (MPa.m$^{0.5}$)**	**F (Hz)**	**H charging (days)**
15-18.5	15	35	0	13-14.5	15	35	0	12-15	15	35	17
18.5-20.5	15	3.5	0	14.5-16	15	3.5	0	15.5-17	15	0.35	17
20.5-23	15	35	0	16-17	T	35	0	17-18	T	35	17
23-25	15	35	3	17-18.4	8	35	0	18-18.2	8	35	17
25-27	15	3.5	3	18.4-20	8	3.5	0	18.2-19.5	8	0.35	17
27-30	15	35	17	20-22	15	3.5	17	19.5-21.7	8	3.5	17
30-32	15	3.5	17	22.5-24.7	15	0.35	17	22-23.6	8	35	17
32-33	T	35	17	24.7-27.5	15	35	17				
33-35	8	35	17	27.5-29	15	3.5	17				
				29-30.5	T	35	17				
				30.5-32	8	3.5	17				
				32-34	8	35	17				

The FCGR relevant to each test condition was measured by the slope of the best linear fit on a graph of the crack length vs the number of cycles (*a*-*N*) as shown in Figure 5-4 (d), (e) and (f). The crack closure forces were also monitored using the method proposed in ASTM E647 appendix X2 with an offset of 4 %.

After test completion, the CT specimens were forced open to reveal the two fracture surfaces. Fractographic observations were performed by optical microscope (OM) and scanning electron microscopy (SEM). In addition, half of CT1 specimen was sliced for hydrogen measurements as described in section 2.4.

5.3 Results

5.3.1 Hydrogen charge and discharge

This section is dedicated to the characterization of the hydrogen concentration profile as a function of time during electrocharging and discharging in ambient environment.

During the charging experiments, the concentration of hydrogen increased with the charging time as observed in Figure **5-3**. It reached an asymptotic value of about 12 mg/kg after 14 days of charging. During the discharging experiments, the concentration of hydrogen decreased exponentially. Hydrogen diffused out the CT specimen intensively within the first two days and reached a stable concentration of about 4 mg/kg after 4 days.

Based on the theory of diffusion, the evolution of hydrogen concentration as a function of time, (*C(t)*), is expected to follow the trend of the Fick's second law applied to the boundary conditions of a specific problem and integrated over the sample thickness. De Araújo et al. [53] simplified Fick's second law for thin plates and membranes where the hydrogen concentration is homogenous within a sample by equation (5.1).

$$\frac{dC^H}{dt} = A[C_e - C^H(t)] \tag{5.1}$$

where A is a constant and C_e is the saturated concentration of a species in a given material. The integration of equation (5.1) applied with boundary conditions leads to:

$$C^H(t) = (C_0 - C_e) * exp(-A * t) + C_e \tag{5.2}$$

where C_0 is the initial concentration of the species in the material. In the work of de Araujo et al., equation (5.2) well described the evolution with time of the concentration of an interstitial element (carbon) in a thin steel plate (1 mm thick).

This form of equation was fitted on our experimental results to interpolate hydrogen concentration, as shown by the dotted lines in Figure **5-3**. The proposed model offers a good fit for both the charging and discharging experiments. This fitting suggests a saturated concentration of H of 13 mg/kg in the studied material. This is in accordance with the work of Solheim et al [54]. The team studied the solubility of hydrogen in a martensitic stainless steel (12% Cr -6% Ni) with different amount of reformed austenite. They reported a solubility limit of 16 mg/kg for steel containing 17% of reformed austenite. The discharging experiment suggests that the value of trapped H after electrocharging and ambient discharging for 14 days is around 4 mg/kg. The charging model fitted to our results was used to choose charging durations of 3 and 17 days with the objective of reaching approximately 6 mg/kg and 13 mg/kg of hydrogen respectively.

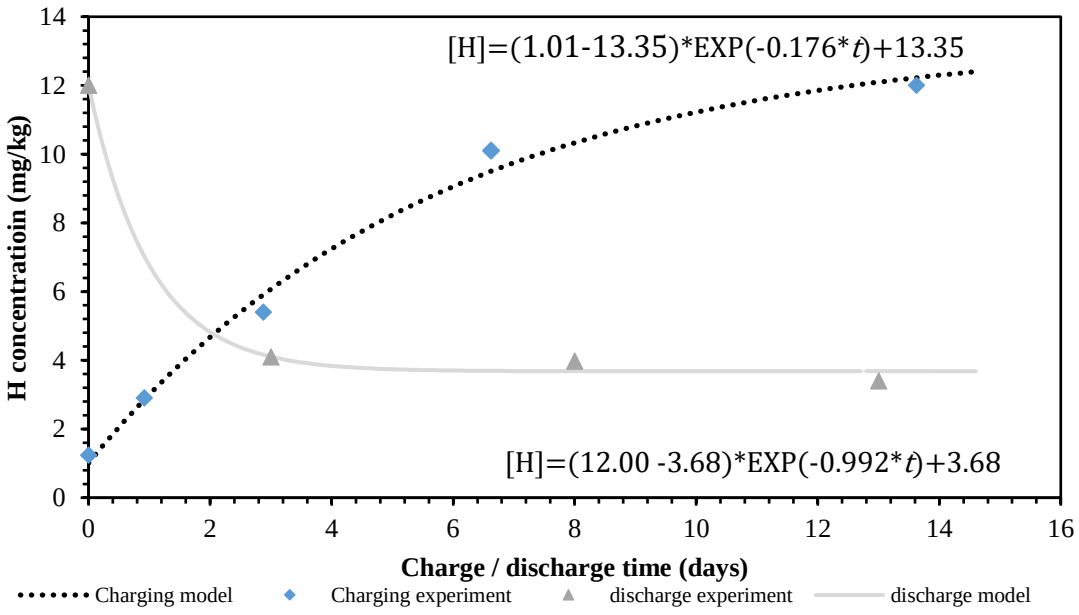

Figure 5-3 Profile of H concentration during charging and discharging.

5.3.2 Effect of hydrogen on the FCGR

The progression of the crack length as a function of the number of cycles (*a*-*N* curve) are presented in Figure 5-4 (a), (b) and (c) for the three CT specimens tested. On these graphs, vertical dotted lines indicate a change in testing conditions (new block). When transiting (T) from a block to another, a certain number of load cycles was necessary to stabilize the crack length reading. This explains the small gaps in data points. In addition, the data points are few for specimen CT1 tested at ΔK = 8 MPa.m$^{0.5}$ (Figure 5-4 (b)). This is the results of an improper data acquisition setting. This was improved by performing data acquisition every 5 000 cycles rather than at fixed crack extension.

For each test block, the FCGR is the slope of the *a*-*N* results. Examples of linear fits are presented in Figure 5-4 (d), (e) and (f) for specimens CT0, CT1 and CT2, respectively.

To reveal trends in the evolution of the FCGR, the measured *da/dN* of the three specimens are grouped per testing conditions and presented in Figure 5-5, where filled symbols represent the results for ΔK = 15 MPa.m$^{0.5}$ and hollow symbols are used for ΔK = 8 MPa.m$^{0.5}$. The average of results, for given testing conditions, is also reported. According to the linear elastic fracture mechanic, a given ΔK is associated with a given crack growth rate. Modification of the FCGR when ΔK remains constant, indicates that some intrinsic or extrinsic characteristics influenced the material resistance to crack growth.

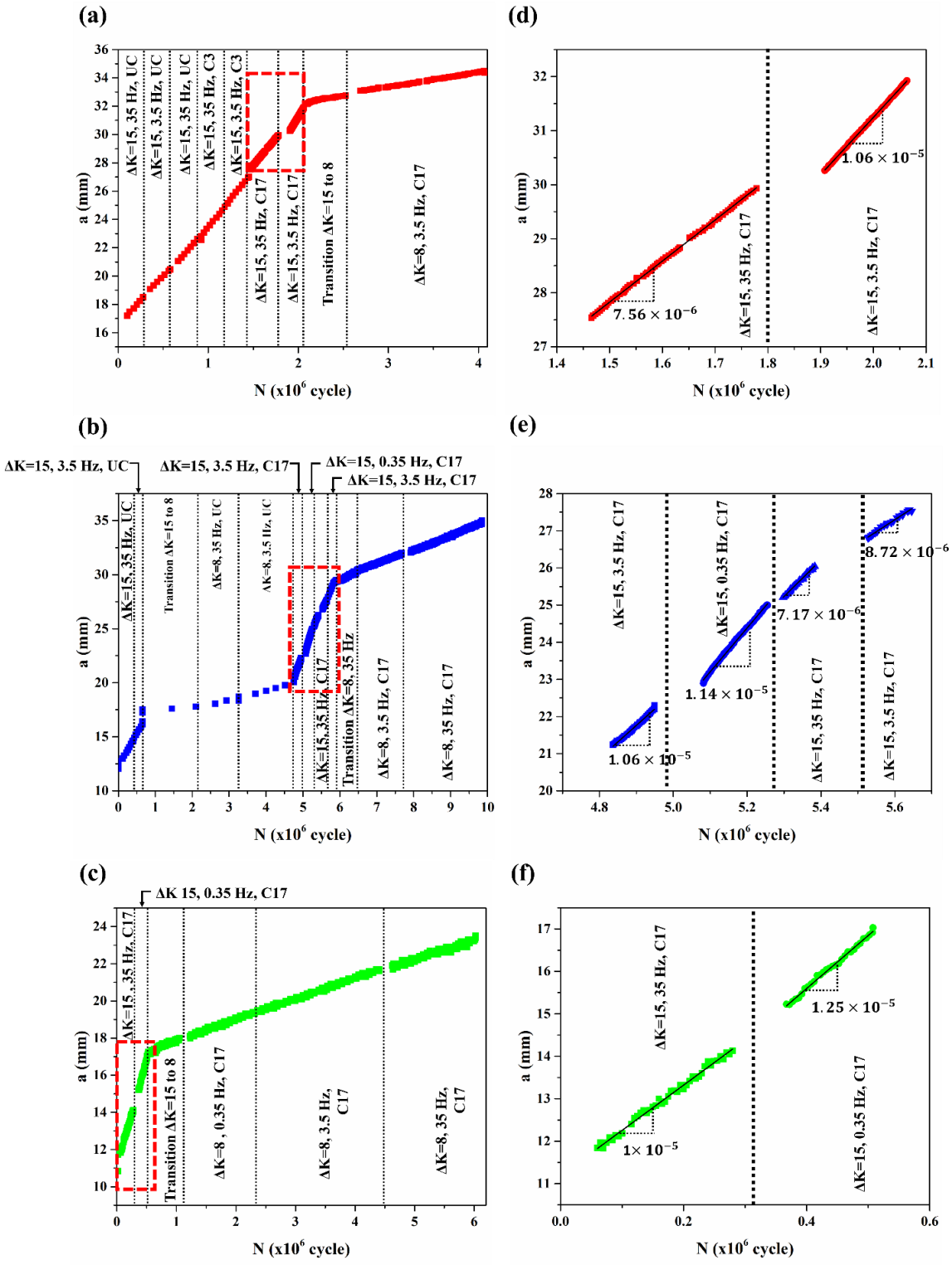

Figure 5-4 Graphs of a-N for CT specimens (a) CT0, (b) CT1 and (c) CT2 for all tested conditions. Graphs (d), (e) and (f) are enlarged views of the a-N curves.

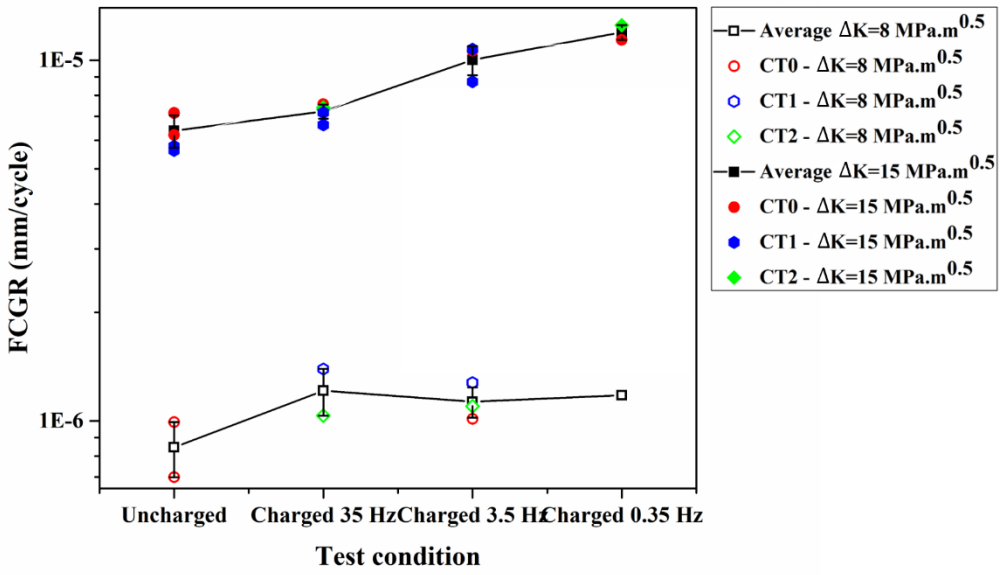

Figure 5-5 FCGR of charged and uncharged specimens at different loading frequencies tested under ΔK = 15 MPa.m$^{0.5}$ and ΔK = 8 MPa.m$^{0.5}$. Lines are connecting experimental points to reveal the trend, they have no physical sense.

For both values of ΔK, the average FCGR of the hydrogen rich material (charged) are greater than the ones measured on the raw material (uncharged specimens). In addition to the hydrogen content, the effect of the load frequency on the FCGR can also be observed. At a ΔK of 15 MPa.m$^{0.5}$; a negative correlation is revealed between the frequency and the FCGR. During the test block performed at 0.35 Hz after electrocharging, the FCGR measured is 1.7 times greater than the one measured at 35 Hz and twice the one measured before electrocharging. On the other hand, at a ΔK of 8 MPa.m$^{0.5}$, the effect of the load frequency on the FCGR is not significant.

To further understand the effect of hydrogen and loading frequency on the crack propagation behavior, the fracture surfaces of three CT specimens are presented in Figure 5-6. The pre-crack area and the different test blocks, matching the graphs in Figure 5-4 are identified.

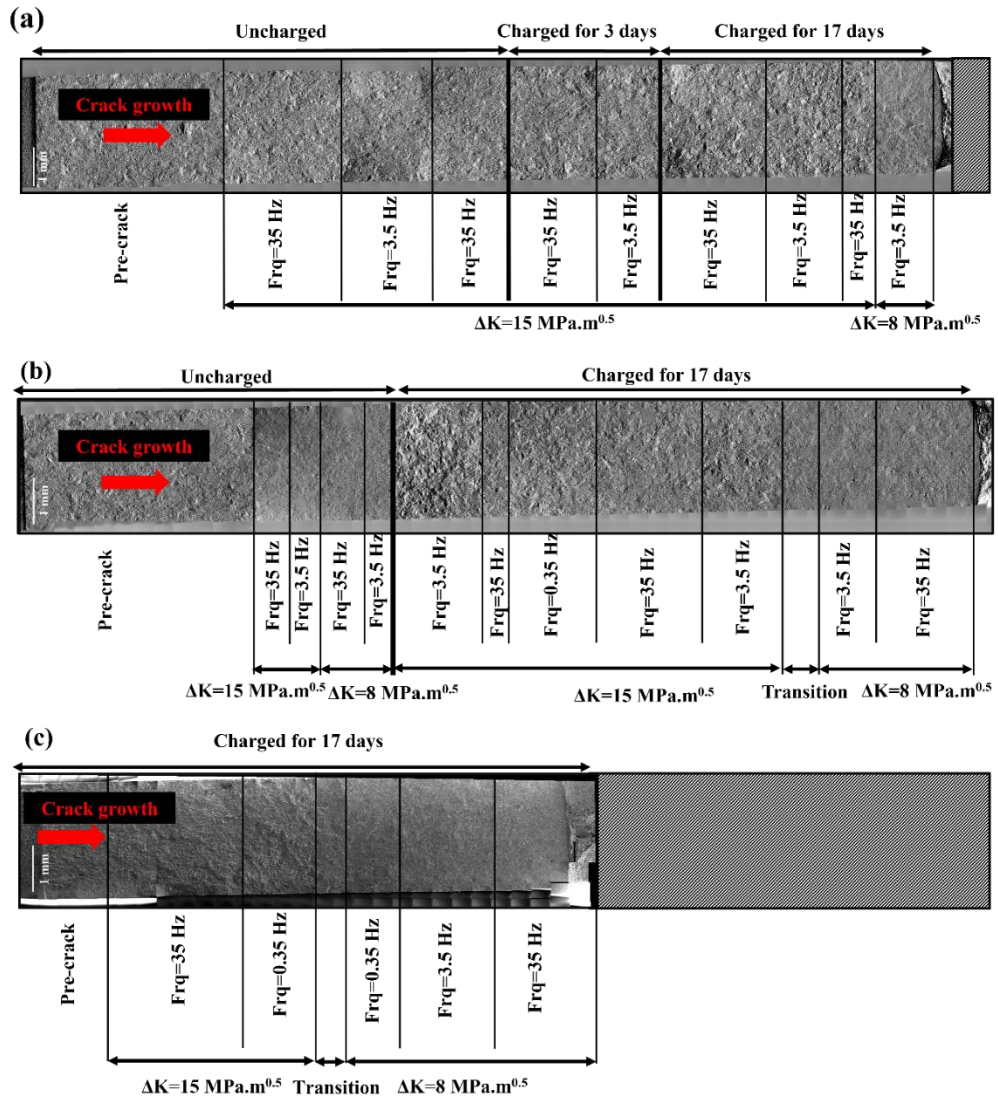

Figure 5-6 Overview of fracture surface of CT specimens after FCG test: (a) CT0, (b) CT1 and (c) CT2.

From the pictures presented in Figure 5-6 a difference in the fracture surface appearance is observed between the portion of test performed at a ΔK of 8 and 15 MPa.m$^{0.5}$. The former being smoother than the latter. Most importantly, charging the specimens with hydrogen for 17 days had an impact on the crack path. The existence of very bright regions is an indication of potential intergranular features.

Higher magnification pictures of the fracture surfaces are shown in Figure 5-7 and Figure 5-8. In Figure 5-7, the typical fracture surfaces created while testing at a ΔK of 8 MPa.m$^{0.5}$ are presented.

A side-by-side comparison reveals the effect of frequency (35 Hz on the left and 3.5 Hz on the right) and the up and down comparison shows the effect of hydrogen.

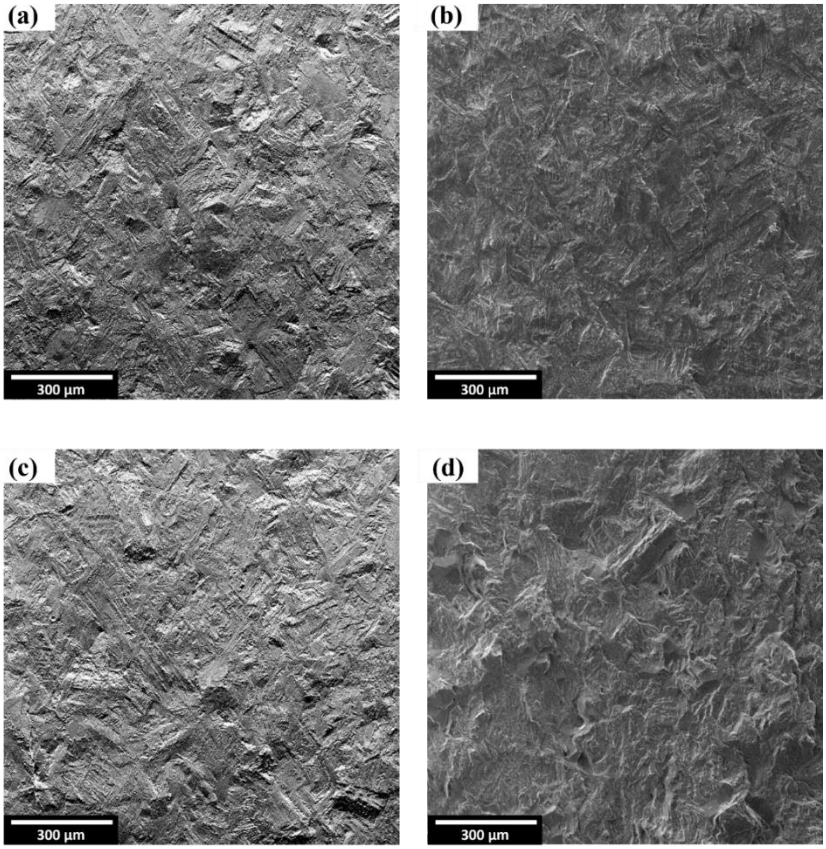

Figure 5-7 Shows SEM analysis of fracture surfaces of CT1 specimen after FCG at $\Delta K = 8\ MPa.m^{0.5}$ for uncharged specimens tested at frequency of (a) 35 Hz and (b) 3.5 H, and for charged specimens tested at frequency of (c) 35 Hz and (d) 3.5 Hz.

The main fracture mechanism observed on the four pictures above is transgranular. Figure 5-7 (a), (b) and (c) are very similar: the surfaces are smooth with some martensitic features visible. Similar fracture surfaces were also reported by Thibault et al. [8] who studied the propagation of fatigue cracks in 415 stainless steel; the crack path seemed to follow martensite sub structures. Figure 5-7 (d) is slightly different. It appears rougher than the other three surfaces. Both cleavage and interpacket features can be observed. Cleavage is recognizable by planes comparable in size to the grains (grains are revealed in Figure 5-1) and covered by river lines. The cleavage feature looks

more brittle than the inter-packet propagation. The presence of hydrogen may have favored the cleavage fracture mechanism.

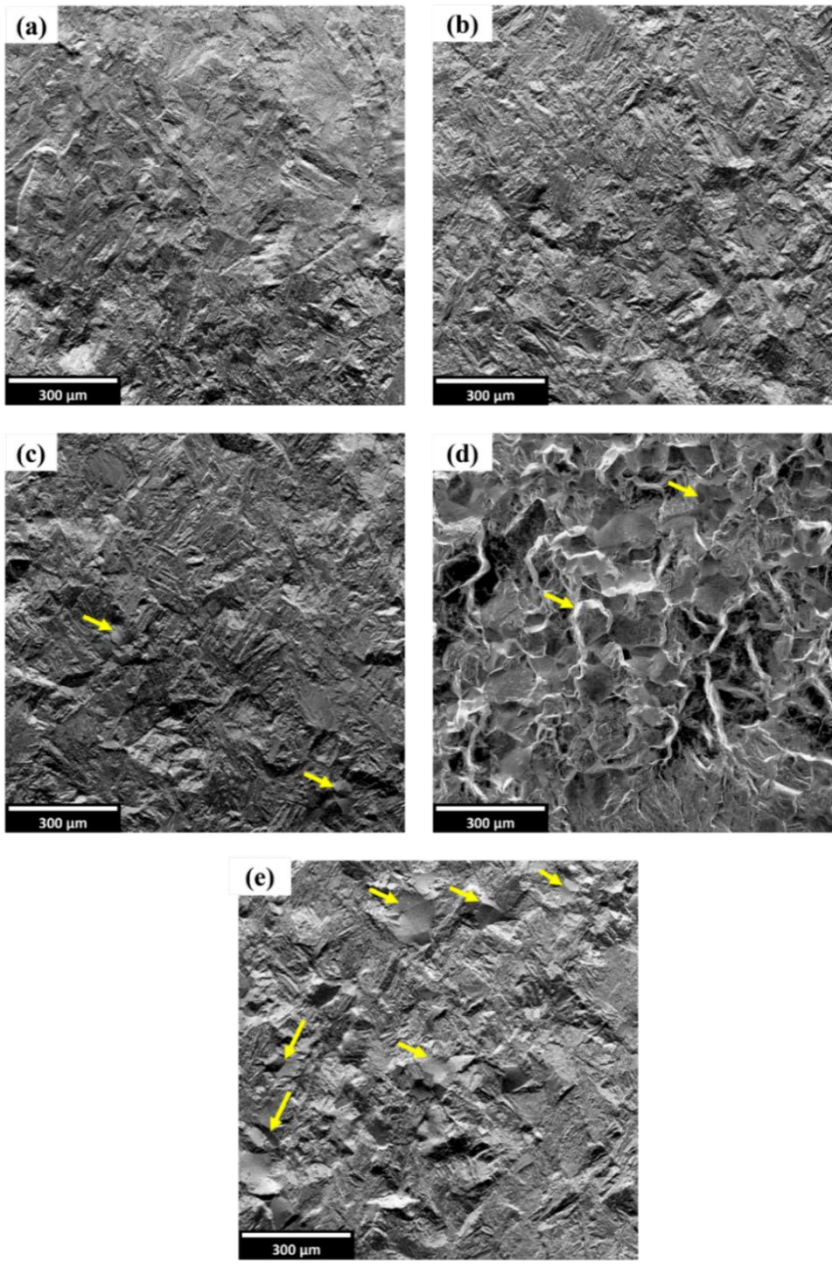

Figure 5-8 Shows SEM analysis of fracture surfaces after FCG test at $\Delta K = 15$ MPa. $m^{0.5}$ for uncharged specimens tested at frequency of (a) CT1 - 35 Hz and (b) CT1- 3.5 Hz, and for charged specimens tested at frequency of (c) CT0- 35 Hz (d) CT0-3.5 Hz. and (e) CT1- 0.35 Hz. Some of the intergranular features are marked by yellow arrows

In the pictures of Figure 5-8, the fracture surfaces created while fatigue testing the material at ΔK=15 MPa.m$^{0.5}$ are presented. A side-by-side comparison is proposed to reveal the effect of frequency (35 Hz for (a) and (c) and 3.5 Hz for (b) and (d)) and the up and down comparison shows the effect of hydrogen. An additional picture taken on the charged specimen tested at 0.35 Hz is also presented in Figure 5-8.

For the raw material (Figure **5-8** (a) and (b)), the fracture surfaces created by a crack propagating at a ΔK of 15 MPa.m$^{0.5}$ are comparable to the ones observed at a ΔK of 8 MPa.m$^{0.5}$. Transgranular propagation revealed packet like features. In this material condition, the frequency has no visible effect on the crack path. On the other hand, the fracture surfaces characterizing the propagation in hydrogen rich material is different. Zones of intergranular propagation are observed at all three tested frequencies as pointed out by the arrows. The surface fraction covered by the intergranular features varies with the testing frequency: ≈ 5% at 35 Hz, ≈ 90 % at 3.5 Hz and ≈ 15% at 0.35 Hz. An explanation of this phenomenon is attempted in the discussion section.

In view of this diversity of crack path, the crack closure was monitored for all test blocks. The closure load over the maximum load (P_{Cl}/P_{max}) for each test condition are presented in the Figure 5-9. For a given testing condition, a mean value of the closure ratio is also provided. These mean values are joined by a line together to show the general trend of the effect of crack closure. These lines have no physical meaning. As indicated in the Figure 5-9, H charging has no significant effect on crack closure under either tested ΔK values. However, at ΔK= 8 MPa.m$^{0.5}$ closure is slightly higher for cracks propagating at low frequencies (3.5 and 0.35 Hz). No explanation is provided to explain this difference in closure load.

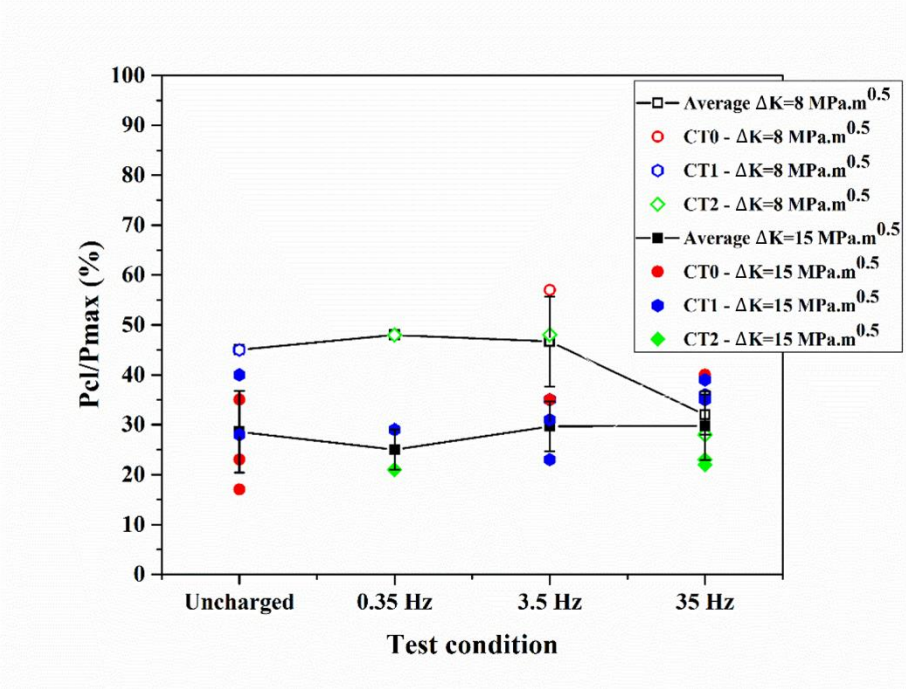

Figure 5-9 Crack closure ratio for different test condition for charged specimens. Lines are joining experimental points to reveal the trend, they have no physical sense.

5.4 Theoretical model explaining synergetic effects of hydrogen and loading conditions on the crack propagation behavior and its application

5.4.1 Model description

The proposed modeled is based on 5 hypotheses (HP) for which we do not have direct experimental proof. Nevertheless, results in the literature and indirect observations are supporting arguments.

HP1. After charging, the H content is homogeneously distributed at the macroscale.

Based on the charging experiments, the hydrogen concentration is nearly at saturation after 17 days of electrocharging. At the scale of the grain size, it is therefore assumed that the hydrogen atoms are homogeneously distributed in the material as schematized in Figure 5-10 (a).

HP2. Hydrogen is heterogeneously distributed at the microscale

According to the work of Johnson et al.[55], the solubility of hydrogen in a BCC steel structure with solution heat of 28.6 kJ.mol^{-1} is about 1.4×10^{18} atoms/m^3. The 4 mg/kg H measured in our material after discharging for 4 days corresponds to approximately (1.9×10^{25} atoms/m^3). This difference of 7 order of magnitude supports the hypothesis that a large quantity of hydrogen is trapped in microstructural heterogeneities. The presence of austenite, in weight fraction of 20 %, could be the microstructural feature trapping hydrogen. In Figure 5-10, trapped hydrogen atoms are schematized by blue dots.

HP3. Transformation of austenite to martensite (TRIPing) releases trapped H

It is of common knowledge that stress localization at the tip of a crack causes the formation of a monotonic plastic zone (MZ). According to Irwin's theory [56], the diameter of this plastic zone, in plane strain condition, can be estimated by equation (5.3) assuming a perfectly plastic material:

$$D_{MZ} = \frac{1}{3\pi}\left(\frac{K_{max}}{\sigma_y}\right)^2 = \frac{1}{3\pi}\left(\frac{\Delta K}{(1-R)\sigma_y}\right)^2 \quad (5.3)$$

Where ΔK is the stress intensity factor range, K_{max} is the maximum stress intensity factor and σ_y is the yield strength. In Figure 5-10 (b), the monotonic plastic zone (MZ) is schematized by a blue circle.

Based on results from the literature, plastic deformation can induce phase transformation of austenite into martensite. Godin et al. [57] experimentally showed that 3 % of plastic strain is sufficient to TRIP almost 80 % of the reformed austenite contained in a 13%Cr-4%Ni martensitic stainless steel. Once such a phase transformation occurs, the hydrogen hypothetically trapped in the austenite is released and free to diffuse. This is in line with the findings of previous studies. Park et al. [58] studied the hydrogen trapping behavior of a duplex stainless steel containing 12 % of austenite. They revealed that the activation energy of trapped H was reduced by the application

of a plastic strain allowing the austenite to transform into martensite. Solheim et al. [54] also observed that the susceptibility to H embrittlement of a martensitic stainless steel containing 12%Cr-6%Ni was following a positive trend with its content of austenite. They proposed that austenite increases the initial H solubility and released it. If such a hypothesis is accepted, a fraction (*Z*) of the trapped hydrogen becomes diffusible once the austenite to martensite phase transformation is triggered. This phenomenon is schematized in Figure 5-10 (b) where the atoms of hydrogen being untrapped are colored in red. In the schematic presentation, *Z=1*, since all H atoms are colored in red.

HP4. Untrapped hydrogen diffuse toward the crack tip

Once the hydrogen is released from the traps, it is available for diffusion. Sofronis et al. [40] proposed that the chemical potential of hydrogen is a function of the hydrostatic stress following equation (5.4):

$$\mu = \mu^0 + RTLnC_L + \sigma_H \bar{V}_H \quad (5.4)$$

Where μ is chemical potential, μ^0 is reference chemical potential, C_L is concentration of H in the metal lattice, $\sigma_H$is hydrostatic stress and $\bar{V}_H$ is volume molar of H. The stress concentration arising at the tip of the crack provides a gradient in chemical potential driving hydrogen diffusion toward the tip of the crack. This diffusion phenomenon is schematized by the green lines in Figure 5-10 (b).

Consequently, under a load, the hydrogen released in the monotonic plastic zone diffuses towards the crack tip resulting in a heterogeneous distribution of hydrogen within the monotonic plastic zone.

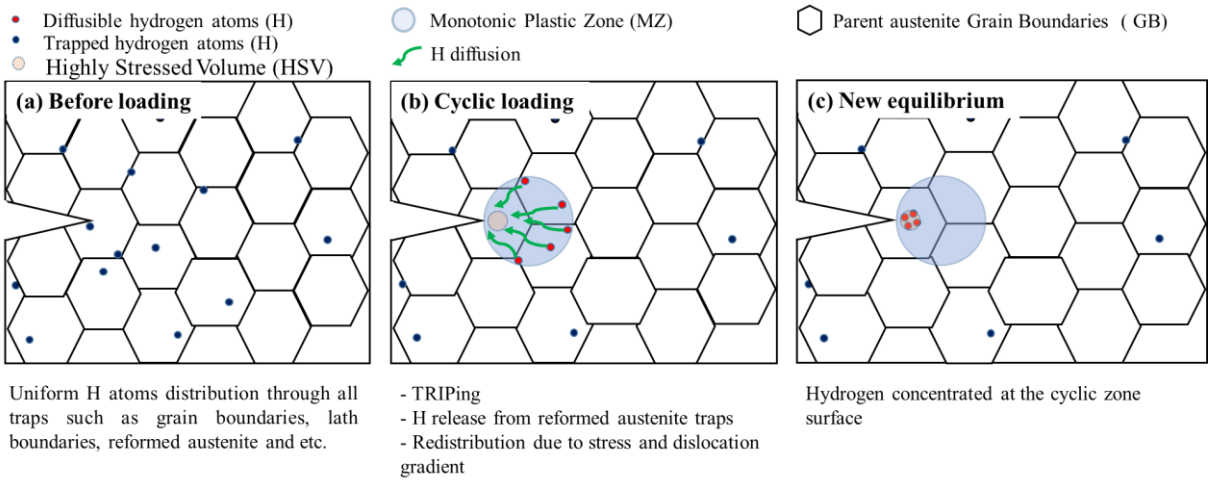

Figure 5-10 Illustration of the hypothesis supporting the proposed model. a) initial distribution of hydrogen in traps, b) H untrapped by the TRIP effect and free to diffuse, c) concentration of H in the region of maximum hydrostatic stress.

To support this hypothesis of hydrogen diffusion toward the crack tip when a load is applied, we compared the local hydrogen content within CT specimens as explained in *section 2.5* The results presented in Figure 5-11 shows a homogeneous hydrogen content in the un-tested specimen while for the specimen subjected to load cycles, the average hydrogen content near the fracture surface is about 3 times higher than the average measured far from the crack (notch) plane. These data support the hypothesis that the stress concentration at the crack tip leads to a local accumulation of hydrogen.

The significant scatter of H concentration near the fracture surface of CT1 specimen is probably the result of the different testing conditions (testing blocks) applied while the crack grew.

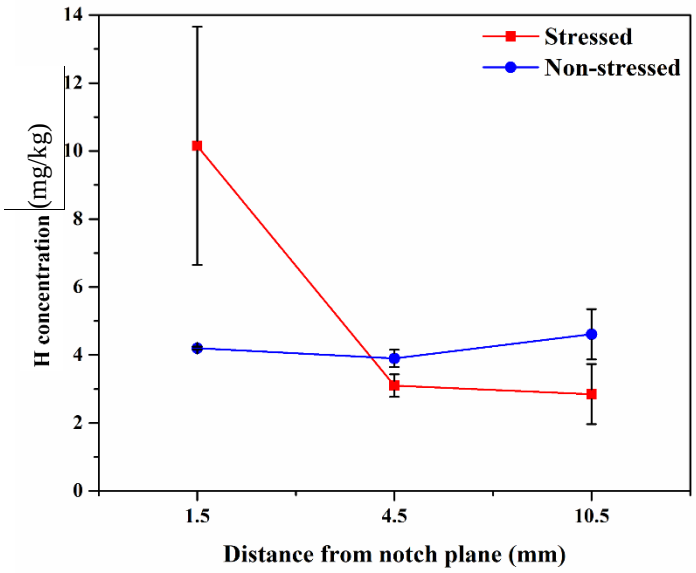

Figure 5-11 H distribution in the stressed and non-stressed CT specimens as a function of the distance normal to the notch plane. Lines are connecting data points to reveal the trend, they have no physical sense.

HP5. Definition of a highly stressed volume

The stress distribution close to the crack tip can be estimated using the large deformation model. Sofronis et al. [40], used this methodology to study the stress distribution at the tip of a crack in a steel having a yield strength of 1200 MPa. They proposed a nonlinear distribution of the hydrostatic stress, σ_H, as schematized by the dotted line in Figure 5-12. The maximum value of the hydrostatic stress is located at a distance R, equal to 1.22 δ, from the crack tip, where δ is the crack tip opening displacement (CTOD).

To estimate the hydrogen concentration at the location of maximum hydrostatic stress, we propose to define a highly stressed differential volume (*HSV*) as a reference of our calculations. The *HSV* is considered as the region where the hydrostatic stress is maximum. The *HSV* is represented a cylinder revolving around an axis position at $R = 1.22\delta$ as schematized in Figure 5-12. The diameter of the cylinder (D_{HSV}) is assumed to be independent of the applied ΔK.

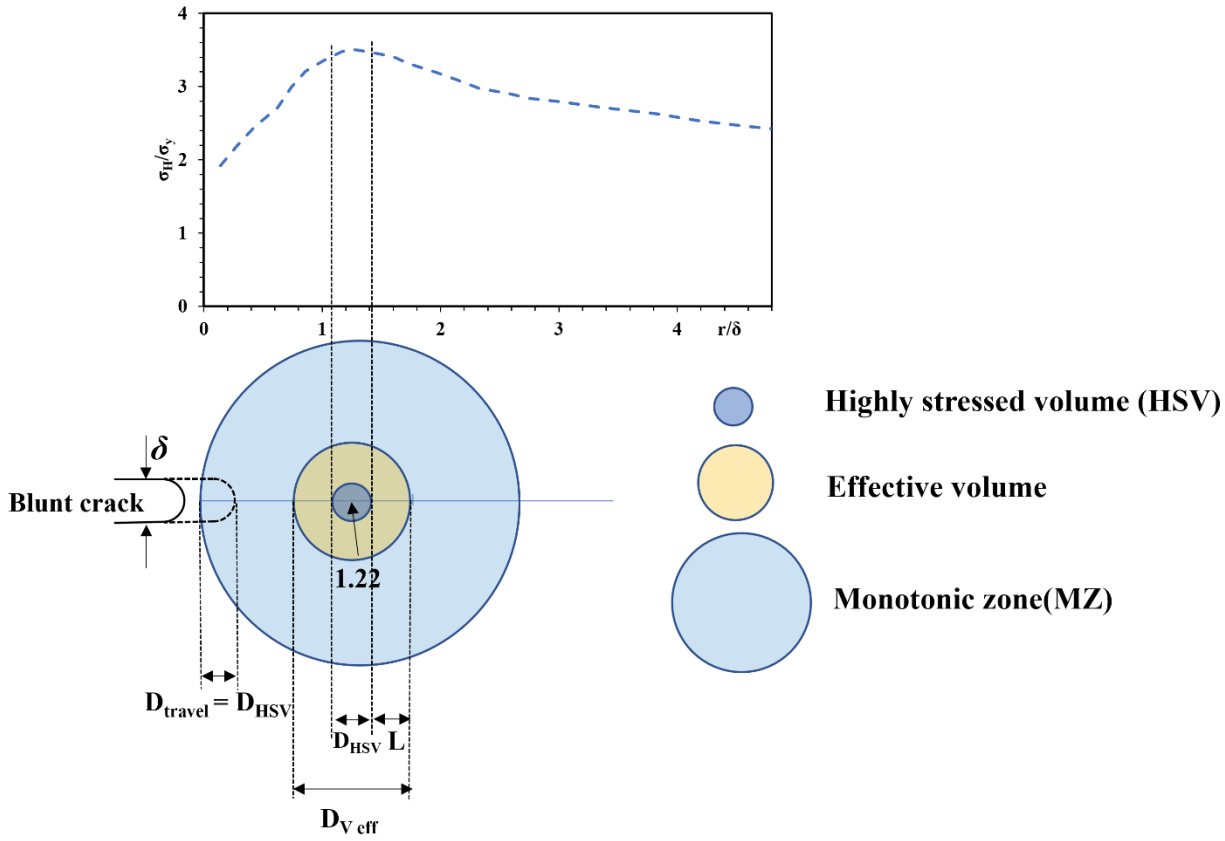

Figure 5-12 Schematic representation of the hydrostatic stress distribution at a crack tip. The position of the highly stressed volume is also illustrated.

Proposed model: H concentration in the HSV as a function of the crack growth velocity (da/dt) and the ΔK

For a given material, the H concentration in the *HSV* (C_{HSV}^{H}) is determined by the number of hydrogen atoms (N_{HSV}^{H}) divided by the volume of the *HSV*.

According to hypothesis HP3, the number of H atoms available to diffuse toward the *HSV* is a fraction, *Z*, of the H originally contained in the volume of the monotonic plastic zone (V_{MZ}). Such can be expressed by equation (5.5):

$$N_D^H = C_U \times Z \times V_{MZ} \tag{5.5}$$

where N_D^H is the number of hydrogen atoms available for diffusion (in atom), C_U is the average H concentration (in atom/m^3) in the bulk material before applying a load. If time for diffusion is infinite the system will reach a thermodynamic equilibrium. In this case, the concentration of hydrogen in the *HSV*, $C_{HSV_{eq}}^H$, is expressed in equation (5.6):

$$C_{HSV_{eq}}^H = \frac{4N_D^H}{\pi {D_{HSV}}^2} = \frac{4(C_U \times Z \times V_{MZ})}{\pi {D_{HSV}}^2} \tag{5.6}$$

In equation (5.6), the sample thickness *B* is assumed to be unity (1 m).

The scenario of hydrogen diffusion in an environment where a crack propagates is different. The position of the crack tip and of the *HSV* evolve as the crack grows. When the time needed for the crack tip to propagate for a distance equal to D_{HSV} is shorter than the time needed for the available hydrogen to diffuse to the *HSV*, the concentration of H in the *HSV* depends on the crack growth velocity *da/dt*. In such a non-equilibrium situation, the faster the crack propagates, the lesser time is available for diffusion, and consequently the local hydrogen concentration is lower.

To generalize the expression of $C^H{}_{HSV}$ for non-equilibrium situations ($C_{HSV_{non-eq}}^H$), an effective volume of diffusion, V_{eff}^H, smaller than V_{MZ} is used resulting in the following equation:

$$C_{HSV_{non-eq}}^H = \frac{4\left(C_U \times Z \times V_{eff}^H\right)}{\pi {D_{HSV}}^2} \tag{5.7}$$

When time is infinite, $V_{eff}^H = V_{MZ}$ and the hydrogen concentration in the *HSV* is at its maximum. Otherwise, $C_{HSV_{non-eq}}^H$ is kinetic dependent as there exists a competition between the crack velocity and the diffusion of hydrogen. Therefore, V_{eff}^H is a function of both the load (*K*) and the crack velocity ($da/dt = f \times da/dN$).

The expression proposed for V_{eff}^H , still assuming a specimen thickness of unity, is the following:

$$V_{eff}^H = \frac{\pi}{4}(D_{HSV} + 2L)^2 \tag{5.8}$$

where L, a function of time, is the maximum distance the H atoms can reach by diffusion while the crack propagates over a distance equivalent to the highly stressed volume (D_{HSV}). As schematized in Figure 5-12, L is the difference between the radius of the V_{eff}^{H} and the *HSV* if one assumes that the *HSV* and the V_{eff}^{H} have the same center position.

The maximum diffusion distance is a function of the effective diffusion constant of hydrogen, D^H, and the time available for diffusion, Δt as expressed in equation (5.9).

$$L = 2(D^H \times \Delta t)^{0.5} \tag{5.9}$$

where D^H is the effective diffusion constant of hydrogen (m^2/s) and Δt is the time (s), needed for the crack to grow on a distance equal to D_{HSV}. Equation (5.9) can be expressed as a function of the crack propagation rate and the loading frequency as follows:

$$L = 2\left(D^H \times \frac{D_{HSV}}{\left(\frac{da}{dN}\right).f}\right)^{0.5} \tag{5.10}$$

Combining equations (5.8) and (5.10), an expression of V_{eff}^{H} as a function of *da/dN* and f is obtained:

$$V_{eff}^{H} = \frac{\pi}{4}(D_{HSV} + 4(D^H \times \frac{D_{HSV}}{\left(\frac{da}{dN}\right).f})^{0.5})^2 \tag{5.11}$$

Equation (5.11) can be further generalized by substituting *da/dN* with a Paris type relationship:

$$V_{eff}^{H} = \frac{\pi}{4}(D_{HSV} + 4(D^H \times \frac{D_{HSV}}{(C.\Delta K^{m_2}).f})^{0.5})^2 \tag{5.12}$$

By combining equation (5.12) and equation (5.7), the effect of the loading frequency and the ΔK on the concentration of hydrogen at the crack tip is explained.

For a given material containing a given amount of hydrogen, C_U, Z, D^H, D_{HSV}, C and m_2 are constants and $C^H_{HSV_{non-eq}}$ is influenced only by f and ΔK as simplified in equation (5.13):

$$C^H_{HSV_{non-eq}} = C_U\left(1+\frac{C_1}{\Delta K^{m_2}.f}+2\left(\frac{C_1}{\Delta K^{m_2}.f}\right)^{0.5}\right), \qquad C_1 = \frac{16D^H}{D_{HSV}C} \tag{5.13}$$

Equation (5.13) proposes a negative correlation between the concentration of the hydrogen in the *HSV* with ΔK and frequency. It is due to an increased in crack velocity ($\frac{da}{dt}$) caused by increasing ΔK and *f*. consequently the time needed to cross the *HSV* is reduced. Since this is the time available for diffusion of H, the diffusion distance is shortened and not all the H available in the monotonic zone reaches the *HSV*. This negative relationship explains our results and the results of Rodkey et al.[5]. Rodkey et al. studied the effect of hydrogen on the propagation kinetics of cracks within a martensitic stainless steel (12Cr-1Mo). They performed crack propagation tests at three load frequencies (0.2 Hz, 1 Hz and 5 Hz) and recorded the fastest FCGR at the lowest frequency (0.2 Hz).

Finally, the general model predicting the concentration of hydrogen near the crack tip is expressed by equation (5.14):

$$C^H_{HSV} = min\begin{cases} C^H_{HSV_{eq}} = \dfrac{4N^H_D}{\pi {D_{HSV}}^2} = \dfrac{4(C_U \times Z \times V_{MZ})}{\pi {D_{HSV}}^2} \\ C^H_{HSV_{non-eq}} = C_U\left(1+\dfrac{C_1}{\Delta K^{m_2}.f}+2\left(\dfrac{C_1}{\Delta K^{m_2}.f}\right)^{0.5}\right) \end{cases} \tag{5.14}$$

It is the minimum value of the equilibrium hydrogen concentration (equation (4.6)) and the non-equilibrium (equation (5.13)).

5.4.2 Application of the model to our testing conditions

We applied the model to our testing conditions by fixing the constants C_U, C, m_2 and D_{HSV} with the values provided in Table 5.3. For the value of C_U the plateau of the discharge profile (Figure 5-3) is considered (4 mg/kg). For the C and m_2 the values reported by Deschênes et al. [7] for this alloy tested under R=0.1 are used. To ease calculation, the D_{HSV} is fixed to 1 µm.

Table 5.3 List of constants and corresponding values used to apply the model to our experimental results

Constant	Value	References
C_U (atom/m3)	1.88×10^{25}	Present experiments
C (MPa and m/cycle)	2.14×10^{-12}	Deschênes et al. [7]
m_2 (unit less)	3.2	Deschênes et al. [7]
D_{HSV} (m)	1×10^{-6}	Assumed

With these values fixed, the evolution of $C^H_{HSV_{eq}}$ and $C^H_{HSV_{non-eq}}$ as a function of ΔK are plotted in Figure 5-13. Since $C^H_{HSV_{non-eq}}$ is a function of the frequency, the three plots presenting the tested frequencies are presented.

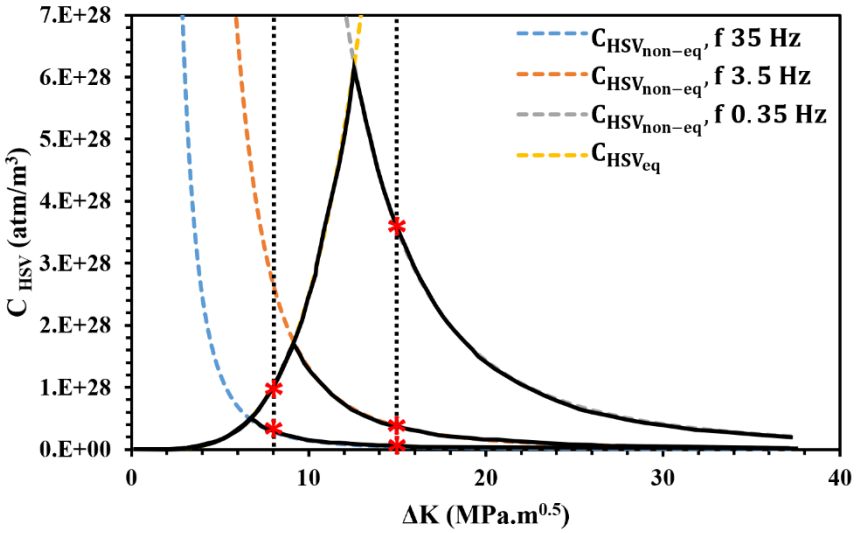

Figure 5-13 Relationship of $C^H_{HSV_{eq}}$ and $C^H_{HSV_{non-eq}}$ with ΔK as predicted by the prosed model

For a given load frequency, the minimum of $C^H_{HSV_{eq}}$ and $C^H_{HSV_{non-eq}}$ gives the estimated value of the H concentration in the *HSV*. It is presented by solid lines in Figure 5-13. These minimum functions

have a bell shape with a well-defined maximum of hydrogen concentration at a ΔK specific for each load frequency. Above this critical ΔK value, the concentration of hydrogen is non-equilibrium and controlled by the kinetic of hydrogen diffusion and crack velocity.

Our experimental conditions, ΔK=15 MPa.m$^{0.5}$ and ΔK=8 Mpa.m$^{0.5}$, are marked on Figure 5-13 by dotted black lines. For the experiments performed at ΔK=15 MPa.m$^{0.5}$ the concentration of hydrogen at the crack tip is non-equilibrium and highly dependent on the load frequency. This should result in different FCGR at each tested frequency under this ΔK. At ΔK=8 MPa.m$^{0.5}$, the tests performed at 0.35 Hz and 3.5 Hz result in a crack velocity slow enough to allow all the hydrogen to diffuse to the *HSV* leading to intersection at below critical ΔK. No difference in the FCGR is expected between these two test conditions. The C_{HSV}^{H} predicted at ΔK=8 MPa.m$^{0.5}$ and 35 Hz falls above the critical ΔK . It is therefore kinetic dependent. For this last testing condition, the predicted C_{HSV}^{H} is the smallest of all tests performed at ΔK=8 MPa.m$^{0.5}$.

The interpretation of Figure 5-13 is supported by quantitative calculations presented in Table 5.4. Also presented in Table 5.4, the differences in the measured FCGR caused by the presence of hydrogen. This difference is normalized by the FCGR characterizing the raw material (uncharged specimen) at a given ΔK and expressed in %. This characteristic, expressed in equation (5.15), is named the cyclic susceptibility to hydrogen embrittlement (CSHE).

$$CSHE = \left(\frac{FCGR\ hydrogen - FCGR\ raw}{FCGR\ raw}\right) * 100$$

Table 5.4 Concentration of hydrogen in the HSV (C_{HSV}^{H}) and cyclic susceptibility to hydrogen embrittlement (CSHE) for all tested conditions

ΔK (MPa.m$^{0.5}$)	Frequency (Hz)	C_{HSV}^{H}	CSHE (%)
15	35	7.5E+26	13
15	3.5	6.3E+27	57
15	0.35	6.2E+28	87
8	35	4.88E+27	43
8	3.5	10.21E+27	34
8	0.35	10.21E+27	39

Except for two experimental conditions (f = 3.5 and 0.35 Hz under ΔK=8 MPa.m$^{0.5}$), the ascending order of the predicted C_{HSV}^{H} is in accordance with the ascending order of the CSHE. Nevertheless, based on the predicted C_{HSV}^{H} , the CSHE of the specimens tested at ΔK=8 and f = 3.5 and 0.35 in the presence of hydrogen should be greater than 57%. We explain this divergence of the experimental results with the model by crack closure. As presented in Figure 5-9 a higher crack closure load ratio was measured for the tests blocks performed at ΔK=8 and f = 3.5Hz and 0.35 Hz. This higher crack closure describes the lower measured FCGR comparing to what is predicted by the model. To account for closure, the proposed model could be expressed in effective ΔK. However, using the model regardless of the effect of crack closure would ends up with more conservative predictions. Consequently, for the purpose of this paper the concept of effective ΔK was not considered for less complexity.

Based on Figure 5-13 andTable 5.4, we conclude that the proposed model can successfully explain the combined effect of pre-charged hydrogen, ΔK and load frequency on the FCGR in the studied conditions.

5.5 Conclusions

The effect of pre-charged H on the fatigue behavior of cracks propagating in a 415 stainless steel was studied. Experiments mainly consists of FCG tests performed on CT specimens at two constant ΔK (15 MPa.m$^{0.5}$ and 8 MPa.m$^{0.5}$) under three different load frequencies (35 Hz, 3.5 Hz and 0.35 Hz). Hydrogen was introduced electrochemically to the material up to a concentration of 13 mg/kg.

The main conclusions are the following:

- For all tested conditions, the FCGR was higher in hydrogen rich specimens than in the raw material.
- Smaller load frequency led to higher FCGR in hydrogen enriched material tested at a ΔK of 15 MPa.m$^{0.5}$. The effect of frequency is not significant at a ΔK of 8 MPa.m$^{0.5}$.
- The highest FCGR, monitored at a ΔK of 15 MPa.m$^{0.5}$ and a load frequency of 0.35 Hz, is two times greater than the one measured in the raw material (same loading conditions).
- The fracture mechanisms in the raw material are essentially transgranular with inter packet like features, while in hydrogen rich material, cleavage and intergranular features are observed.
- A theoretical model was proposed to predict the hydrogen concentration near the crack tip. This model well describes the influence of the ΔK and the load frequency on the local hydrogen concentration.
- The prediction of the hydrogen concentration near the crack tip is correlated positively with the cyclic susceptibility to hydrogen embrittlement.

To finish with a more practical conclusion of this work, our results show that hydrogen introduced in 415 stainless steel (30 HRC) can double the FCGR under specific testing conditions. Moreover, the proposed model can anticipate the critical loading condition for which the presence of hydrogen will significantly increase the FCGR. Additional work on this topic is needed to validate the applicability of this model to a wider range of testing conditions and to other materials.

5.6 Acknowledgment

The work was financially supported by the Institut de recherche d'Hydro-Québec (IREQ), SACMI, Natural Sciences and Engineering Research Council of Canada (NSERC) and Consortium de recherche et d'innovation en transformation métallique (CRITM). Cooperation of S. Laliberté-Riverin, Alexandre Bois-Brochu, Pierre-Antony Deschênes and C. Baillargeon is also acknowledged.

CHAPTER 6 GENERAL DISCUSSION

The scientific manuscript presented in the previous chapter encompasses the main discussion for this project. However, an additional discussion addressing complementary results is proposed herein to address the sub-objectives of the project which are the following:

SO1: Develop a test method to introduce hydrogen to AISI 415 and validate its efficiency and reproducibility.

SO2: Measure the effect of absorbed hydrogen on the FCGR of AISI 415.

SO3: Characterize the impact of absorbed hydrogen on the fatigue fracture mode.

SO4: Theoretically explain the behaviours observed in SO2 and SO3.

6.1 Verification of efficiency of test method to investigate susceptibility to hydrogen embrittlement

Section 4.1 presented the results of testing the susceptibility of AISI 415 (13Cr-4Ni) alloy with 20 % reformed austenite to hydrogen embrittlement under monotonic loading. As explained in Chapter 2, a pre-charged hydrogen strategy was used to obtain these results. In this strategy, test samples were charged before being mechanically tested, so that a relatively high amount of hydrogen was available before the application of stress.

Although the method used in this study to introduce hydrogen to the test samples (pre-charged hydrogen strategy) is different from that used by other researchers [2, 18], our results agree with their findings. The use of pre-charged hydrogen is capable of triggering hydrogen embrittlement under a SSRT, as observed in other studies using external hydrogen charging. In the present study, the MSHE for AISI 415 with 20 % reformed austenite was 44 %. Fan et al. [18]reported a similar MSHE value of 42 % for the same material using the external hydrogen charging applied in-situ during the SSRT.

6.2 Measuring the effect of absorbed hydrogen on the rate and path of fatigue crack propagation in AISI 415

Our study reveals that pre-charged H increases FCGR under all tested ΔK and frequencies. We demonstrate that initial H concentration (depending on charging/discharging time), ΔK and frequency affect the CSHE.

Direct application of these findings to practical working conditions is limited to situations where internal H content is available, including but not limited to the condition of hydrogen diffusion during fabrication or repair welding.

Our study reveals that pre-charged H increases brittle fracture features such as quasi-cleavage and intergranular fractures. It also reveals that maximum intergranular fracture occurs when monotonic zone size (MZS) is comparable with PAG size and *da/dt* is optimal (in our case 3.5 Hz) allowing enough time for H to reach the boundaries but not so much time that H depletion occurs.

6.3 Proposed theory to explain observations

The proposed model indicates that three phenomena govern the effect of pre-charged hydrogen on fatigue crack propagation behaviour: first, the available diffusible hydrogen, second, hydrogen redistribution at the crack tip, and third, crack closure.

In the case of internal H, these 3 parameters can be interpreted as follows. Available diffusible H is controlled by initial trapped H concentration and monotonic zone size. Hydrogen redistribution occurs due to the stress gradient from the entire volume of the monotonic zone toward the highly stressed volume (*HSV*), where hydrostatic stress is maximal. Therefore, H concentration in the *HSV* tends to increase. The crack velocity (da/dt) can limit the amount of hydrogen reaching the *HSV* explaining the influence of f and ΔK on the *CSHE*. Lastly, crack closure should not be overlooked, as it can shield the effect of H, especially at lower ΔK values.

6.4 Generalization of the findings to working conditions

Generalization of the findings of this study to actual working conditions for hydroelectric turbines in Hydro-Québec infrastructures requires detail knowledge of the working conditions. In this

section limitations of the results and conclusion are highlighted and recommendations for future studies are proposed.

The following are three limitations of this study in the perspective of hydraulic turbines 'working conditions:

a. Different sources of hydrogen:

   In actual working conditions, a combination of internal and environmental hydrogen is expected. Pre-charging method used in this study is more representative to the case of internal hydrogen coming from sources such as welding and plating. Environmental hydrogen, which is generated in the vicinity of corrosion pits due to the electrochemical reactions of corrosion, can behave in a relatively different manner because they are generated while the crack is propagating.

b. Limitation of *R* ratio:

   In the present study, the applied *R ratio* is 0.1, whereas hydroelectric turbines runner are subjected to a combination of load cycles with *R ratio* ranging from 0.1 to 0.7. At high R values, less crack closure is expected. Consequently, the FCGR under working conditions may be higher than the data provided in this work.

c. Limitation of reformed austenite content

   This study tested AISI 415 samples with 20% reformed austenite. However, in practical applications, alloys have reformed austenite content ranging from 2% to 20%. A smaller amount of reformed austenite is expected to significantly reduce the amount of trapped hydrogen and therefore decrease the material's susceptibility to pre-charged hydrogen embrittlement. On the other hand, a lower content in reformed austenite is expected to increase the diffusion rate of H. This could counterbalance the first effect.

A situation comparable to working condition of hydro turbines (R=0.7 and environmental hydrogen) would appear to be harsher than the condition studied (R=0.1 and pre-charged hydrogen), since the two controlling factors of limited available hydrogen and crack closure are no longer in effect. In such a case, hydrogen is continuously generated by corrosion, so that the amount of available hydrogen would be controlled by the rate of corrosion reactions and the hydrogen

permission rate. It would thus no longer be limited to untrapped hydrogen in the monotonic zone. Moreover, a high *R ratio* prevents crack closure, and its shielding effect is no longer expected.

Considering this discussion, it would be advisable to more directly validate these predictions by investigating the effect of hydrogen on FCG utilising an in-situ hydrogen charging strategy (representing environmental H), and in addition, to duplicate tests at higher *R ratio*s (i.e., 0.7). Testing samples with lower reformed austenite content is also essential as it could offer a direct observation for the hypothesized role of reformed austenite as a reservoir of hydrogen in a pre-charging hydrogen strategy. This is also critical as the hydrogen diffusion rate in the alloy is relative to the reformed austenite content. The results could then more readily be used for analysis of fatigue corrosion of AISI 415 under actual working conditions.

In addition, it is recommendable to put special attention to recognize and control the internal H sources during fabrication and maintenance of 415 stainless steel parts. The effective internal H can introduce to the material during welding. Therefore, it is crucial to observe practices such as preheating the parts or drying the welding consumables before welding.

Lastly it should be highlighted that when the FCGR test results are used for the remaining life estimation, planning inspections, or deciding about maintenance intervals, it is essential to consider the H content of test samples and actual working parts.

CHAPTER 7 CONCLUSION AND RECOMMENDATIONS

The sub-objectives of the project were met in four main steps. First, a methodology was developed to promote hydrogen embrittlement in AISI 415 and its efficiency and reproducibility were proven (SO1) by comparing the mechanical behaviour of hydrogen charged and uncharged samples via slow strain rate tensile testing. Second, the effect of pre-charged hydrogen on the fatigue crack growth rate was measured (SO2) under the constant ΔKs of 15 MPa.m$^{0.5}$ and 8 MPa.m$^{0.5}$ and three different load frequencies (35 Hz, 3.5 Hz, and 0.35 Hz), following ASTM E647 testing method for CT samples. Third, the effect of hydrogen embrittlement on the fatigue fracture mode (crack propagation path) was evaluated (SO3) by studying the fracture surface of hydrogen charged and uncharged CT samples. Finally, the behaviours observed in SO2 and SO3 were explained theoretically (SO4). Lastly, several hypothetical explanations and predictions regarding the effect of hydrogen embrittlement on the fatigue crack growth behaviour of AISI 415 under actual working conditions were presented. Limitations of the present study were discussed, and recommendations for further studies were proposed to examine the role of hydrogen embrittlement in fatigue-corrosion of hydroelectric turbines in Hydro-Quebec facilities.

The present study used AISI 415 alloy in quenched and tempered condition and with a yield strength of around 600 MPa and 20% reformed austenite content. An electrochemical method was employed to charge samples with up to 12mg/kg of hydrogen under ambient conditions.

The main findings of the present study are summarized as follows:

- The electrochemical hydrogen charging method used can introduce hydrogen up to concentrations near the solubility limit.
- Slow strain rate tensile test reveals that electrochemical H charging of the AISI 415 samples can lead to 44% monotonic H susceptibility to hydrogen embrittlement. This finding is in good correlation with H susceptibility to hydrogen embrittlement of 42% reported for the same material in the literature.
- By increasing the hydrogen content from 9 to 13 mg/kg, the fracture surface of tensile samples is changed from quasi-cleavage to intergranular fracture, while an uncharged sample reveals a dimple form ductile fracture with evident plastic deformation.

- Pre-charged hydrogen increased the fatigue crack growth rate for all tested conditions.
- For hydrogen enriched material, a negative correlation exists between the load frequency and the susceptibility of fatigue crack growth rate to H. The lower the loading frequency, the lower the crack velocity and the more time needed to cross the *HSV*. Consequently, the time available for H diffusion toward the *HSV* increases. Such correlation is not observable for uncharged samples.
- Among the conditions tested, the highest FCGR corresponded to a ΔK of 15 MPa.m$^{0.5}$ and load frequency of 0.35, where the FCGR was twice that measured in the raw material.
- In fatigue crack growth tests, the introduction of hydrogen caused a significant change to a brittle fracture mode. The fracture mechanism in the raw material was essentially transgranular with interpacket-like features. Hydrogen charging changed this to a cleavage fracture at a ΔK of 8 MPa.m$^{0.5}$. At all frequencies under ΔK 15 MPa.m$^{0.5}$, a combination of intergranular and cleavage fracture is observed.
- The surface proportion of the intergranular feature changed with the loading frequency and ΔK, so that its maximum is observed at a load frequency of 3.5 Hz and ΔK=15 MPa.m$^{0.5}$.

A theoretical model was proposed to explain the results. The following conclusions are based on this model.

- Effect of pre-charged hydrogen on fatigue crack propagation behaviour is governed by three phenomena: They are the available diffusible hydrogen, hydrogen redistribution at the crack tip, and crack closure.
- For a given loading frequency there exist a value of ΔK leading to a maximum concentration of hydrogen near the crack tip and favoring hydrogen embrittlement.
- Other conditions favoring hydrogen enrichment near the crack tip are slow crack velocity in terms of (da/dt) combined with a large monotonic plastic zone (high values of K_{max}/σ_y).
- The presence of reversible hydrogen traps such as reformed austenite can increase the effect of internal hydrogen embrittlement on the FCGR.
- The effect of hydrogen embrittlement on the FCGR could be more significant under actual working conditions, where hydrogen is continually being generated via corrosion reactions

at the crack vicinity. Hypothetically, if $\frac{da}{dt}$ is slow enough, hydrogen could be accumulated in high concentrations in the critical volume at the position of maximum hydrostatic stress.

Scope of the presented model and findings are limited to the followings:

- The test method was limited to electrochemical pre-charged H. Consequently, the results are not directly interpretable to the case of environmental H.
- The *R* ratio of fatigue test was limited to 0.1.
- The reformed austenite content of the material under this study was 20%.

To finish with a more practical conclusion of this work, our results show that although the hardness of 415 stainless steel is not very high (< 30 HRC) pre-charged hydrogen can double the FCGR in specific testing conditions. Therefore, following recommendations should be observed:

- Special cautions are required during welding in the fabrication and maintenance of the parts made of AISI 415 to recognize and limit the internal H sources. Pre-heating the parts before welding to mitigate the condensation and complete drying the welding consumables are two examples of such cautions.
- Potential difference between H content of the test samples and the actual working components should not be considered, while quantitative measurement of the H content of actual components usually is impractical.
- The proposed model could be used to estimate the severity of H embrittlement under each practical working condition (combination of ΔK and *f*).
- Based on the proposed model, the reformed austenite is acting as a reservoir for H in the microstructure. Therefore, decreasing its content could be beneficial for lowering the susceptibility of FCG to pre-charged H. However, reformed austenite content may influence other mechanisms such as crack closure and diffusion, so its global effect on FCG needs to be studied further.
- Findings of this research could be used for planning further studies to understand the effect of in-situ H source, higher *R ratio* and lower reformed austenite content on the susceptibility of the material to hydrogen embrittlement.

APPENDIX A TECHNICAL DRAWINGS

Herein the technical drawings that were used to fabricate the test samples are presented, Figure A-1 for tensile samples and Figure A-2 for CT samples.

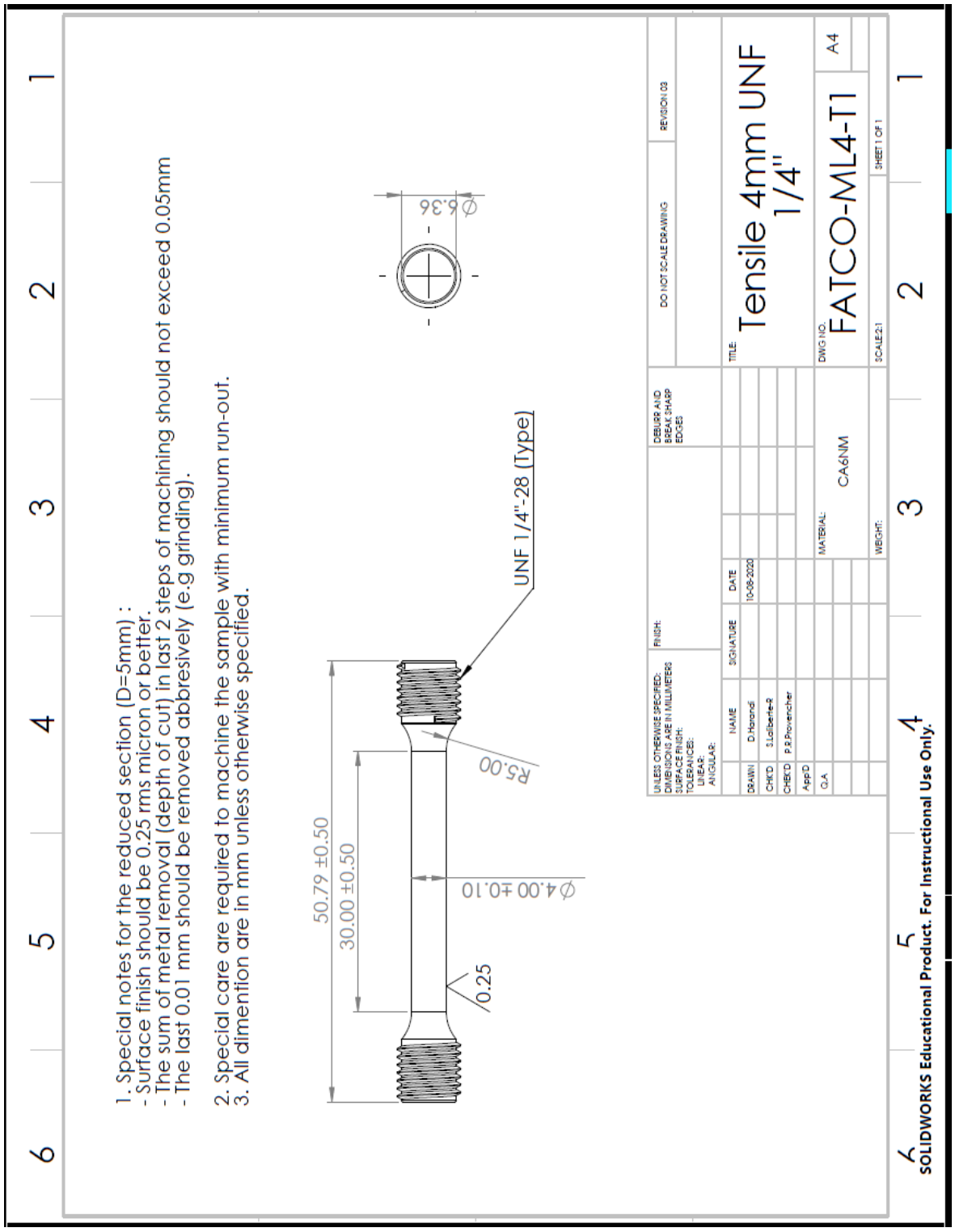

Figure A-1 Technical drawing of tensile samples

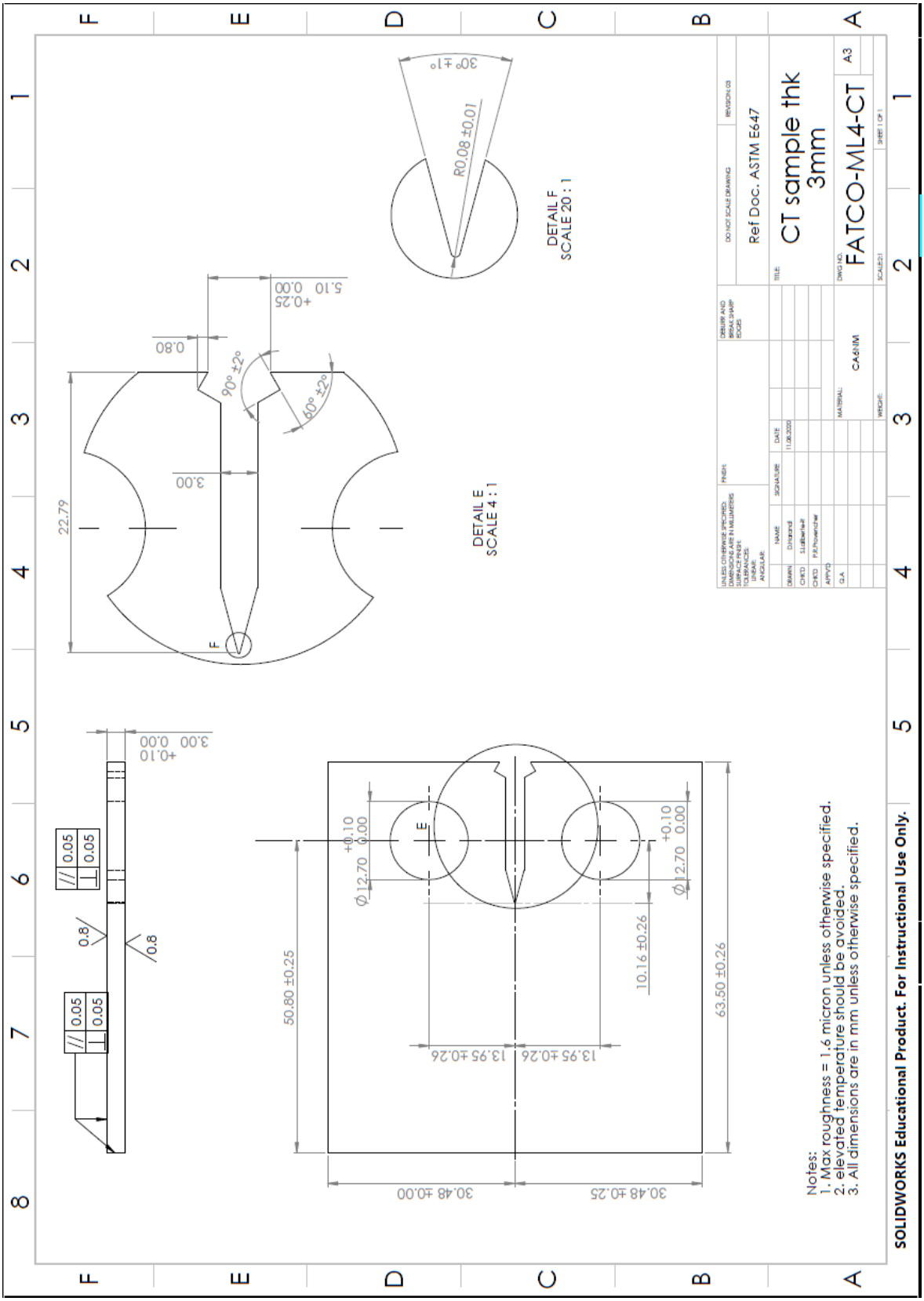

Figure A-2 Technical drawing of CT samples

REFERENCES

[1] *"Standard specification for chromium and chromium-nickel stainless steel plate, sheet, and strip for pressure vessels and for general applications*, ASTM A240, 2018.

[2] J. He, L. Chen, X. Tao, S. Antonov, Y. Zhong, and Y. Su, "Hydrogen embrittlement behavior of 13Cr-5Ni-2Mo supermartensitic stainless steel," *Corrosion Science*, vol. 176, 2020, doi: 10.1016/j.corsci.2020.109046.

[3] L. W. Tsay, Y. F. Liua, R. T. Huang, and R. C. Kuo, "The effect of sensitization on the hydrogen-enhanced fatigue crack growth of two austenitic stainless steels," *Corrosion Science*, vol. 50, no. 5, pp. 1360-1367, 2008/05/01/ 2008, doi: https://doi.org/10.1016/j.corsci.2008.01.005.

[4] E. M. Co. "francis-turbines." http://www.eternoohydro.com/turbines/francis-turbines.html.

[5] G. F. Rodkey and R. H. Jones, "Effect of internal hydrogen on the fatigue crack growth of a 12Cr-1Mo steel," *Journal of Nuclear Materials*, vol. 155-57, no. pt B, pp. 760-765, 1988, doi: 10.1016/0022-3115(88)90411-4.

[6] *"Standard specification for general requirements for flat-rolled stainless and heat-resisting steel plate, sheet, and strip"*, ASTM A480, ASTM, 2018.

[7] P.-A. Deschênes, "Comportement des fissures de fatigue dans un champ de contraintes résiduelles de tension," École polytechnique de Montréal, Montréal, 2016. [Online]. Available: https://publications.polymtl.ca/2287/

[8] D. Thibault, P. Bocher, M. Thomas, J. Lanteigne, P. Hovington, and P. Robichaud, "Reformed austenite transformation during fatigue crack propagation of 13%Cr-4%Ni stainless steel," *Materials Science and Engineering A*, vol. 528, no. 21, pp. 6519-6526, 2011, doi: 10.1016/j.msea.2011.04.089.

[9] J. Chaix, "Influence de la température de revenu sur la résistance du ca6nm à la propagation des fissures de fatigue," Ecole polytechnique de montréal, 2014.

[10] M. Hassanipour, "Fatigue crack propagation under variable amplitude loading in steels used in Francis turbine runners," École polytechnique de Montréal, Montréal, 2017. [Online]. Available: https://publications.polymtl.ca/2814/

[11] "Fatigue crack growth measurement and data analysis," ASTM STP738, J. Hudak, Ed., 1981: ASTM.

[12] N. E. Dowling, *Mechanical Behavior of Materials*. Pearson, 2013.

[13] A. J. McEvily, *On crack closure in fatigue crack growth*. ASTM International, 1988.

[14] A. Trudel, "Étude expérimentale de la propagation de fissures de fatigue dans la zone affectée thermiquement de joints soudés de roues de turbines hydrauliques," École polytechnique de Montréal, Montréal, 2013. [Online]. Available: https://publications.polymtl.ca/1315/

[15] "*Standard test method for measurement of fatigue crack growth rates*," *ASTM E647*, 2015.

[16] A. Akhiate, "Effet de la teneur en carbone sur la résistance du ca6nm à la propagation des fissures de fatigue," Ecole polytechnique de Montréal, 2015.

[17] O. Barrera *et al.*, "Understanding and mitigating hydrogen embrittlement of steels: a review of experimental, modelling and design progress from atomistic to continuum," *J Mater Sci,* vol. 53, no. 9, pp. 6251-6290, 2018, doi: 10.1007/s10853-017-1978-5.

[18] Y. H. Fan *et al.*, "The role of reversed austenite in hydrogen embrittlement fracture of S41500 martensitic stainless steel," *Acta Materialia,* vol. 139, pp. 188-195, 2017, doi: 10.1016/j.actamat.2017.08.011.

[19] Y. Murakami and S. Matsuoka, "Effect of hydrogen on fatigue crack growth of metals," *Engineering Fracture Mechanics,* vol. 77, no. 11, pp. 1926-1940, 2010, doi: 10.1016/j.engfracmech.2010.04.012.

[20] X. Li *et al.*, "Effect of aging treatment on hydrogen embrittlement of PH 13-8 Mo martensite stainless steel," *Materials Science and Engineering: A,* vol. 651, pp. 474-485, 2016/01/10/ 2016, doi: https://doi.org/10.1016/j.msea.2015.09.116.

[21] J. Yang, F. Huang, Z. Guo, Y. Rong, and N. Chen, "Effect of retained austenite on the hydrogen embrittlement of a medium carbon quenching and partitioning steel with refined microstructure," *Materials Science and Engineering: A,* vol. 665, pp. 76-85, 2016/05/17/ 2016, doi: https://doi.org/10.1016/j.msea.2016.04.025.

[22] L. Chen, Z. Ma, R. Shi, Y. Su, L. Qiao, and L. Wang, "Comprehensive effect of hydrostatic compressive stress in retained austenite on mechanical properties and hydrogen embrittlement of martensitic steels," *International Journal of Hydrogen Energy,* vol. 45, no. 41, pp. 22102-22112, 2020/08/21/ 2020, doi: https://doi.org/10.1016/j.ijhydene.2020.06.012.

[23] H. Vehoff and W. Rothe, "Gaseous hydrogen embrittlement in fesi- and ni-single crystals," *Acta Metallurgica,* vol. 31, no. 11, pp. 1781-1793, 1983, doi: 10.1016/0001-6160(83)90125-6.

[24] W. W. Gerberich, T. L1vne, X. F. Chen, and M. Kaczorowski, "Crack growth from internal hydrogen—temperature and microstructural effects in 4340 steel," *Metallurgical Transactions A,* vol. 19, no. 5, pp. 1319-1334, 1988/05/01 1988, doi: 10.1007/BF02662593.

[25] P. J. Ferreira, I. M. Robertson, and H. K. Birnbaum, "Hydrogen effects on the interaction between dislocations," *Acta Materialia,* vol. 46, no. 5, pp. 1749-1757, 1998, doi: 10.1016/S1359-6454(97)00349-2.

[26] Y. Jagodzinski, H. Hanninen, O. Tarasenko, and S. Smuk, "Interaction of hydrogen with dislocation pile-ups and hydrogen induced softening of pure iron," *Scripta Materialia,* vol. 43, no. 3, pp. 245-251, 2000, doi: 10.1016/S1359-6462(00)00398-5.

[27] A. Nagao, M. Dadfarnia, B. P. Somerday, P. Sofronis, and R. O. Ritchie, "Hydrogen-enhanced-plasticity mediated decohesion for hydrogen-induced intergranular and “quasi-cleavage” fracture of lath martensitic steels," *Journal of the Mechanics and Physics of Solids,* vol. 112, pp. 403-430, 2018/03/01/ 2018, doi: https://doi.org/10.1016/j.jmps.2017.12.016.

[28] A. Nagao, K. Hayashi, K. Oi, and S. Mitao, "Effect of uniform distribution of fine cementite on hydrogen embrittlement of low carbon martensitic steel plates," *ISIJ International,* vol. 52, no. 2, pp. 213-221, 2012, doi: 10.2355/isijinternational.52.213.

[29] A. Nagao, C. D. Smith, M. Dadfarnia, P. Sofronis, and I. M. Robertson, "Interpretation of hydrogen-induced fracture surface morphologies for lath martensitic steel," *Procedia Materials Science,* vol. 3, pp. 1700-1705, 2014, doi: 10.1016/j.mspro.2014.06.274.

[30] S. Shen, X. Song, Q. Li, X. Li, R. Zhu, and G. Yang, "A study on stress corrosion cracking and hydrogen embrittlement of Jethete M152 martensitic stainless steel," *Materials Science and Engineering: A,* vol. 740-741, pp. 243-251, 2019/01/07/ 2019, doi: https://doi.org/10.1016/j.msea.2018.10.091.

[31] B. S. Kumar, V. Kain, M. Singh, and B. Vishwanadh, "Influence of hydrogen on mechanical properties and fracture of tempered 13 wt% Cr martensitic stainless steel," *Materials Science and Engineering: A,* vol. 700, pp. 140-151, 2017, doi: 10.1016/j.msea.2017.05.086.

[32] R. Silverstein and D. Eliezer, "Mechanisms of hydrogen trapping in austenitic, duplex, and super martensitic stainless steels," *Journal of Alloys and Compounds,* vol. 720, pp. 451-459, 2017, doi: 10.1016/j.jallcom.2017.05.286.

[33] S. Brück, V. Schippl, M. Schwarz, H.-J. Christ, C.-P. Fritzen, and S. Weihe, "Hydrogen embrittlement mechanism in fatigue behavior of austenitic and martensitic stainless steels," *Metals,* vol. 8, no. 5, 2018, doi: 10.3390/met8050339.

[34] Y. Murakami, T. Kanezaki, Y. Mine, and S. Matsuoka, "Hydrogen embrittlement mechanism in fatigue of austenitic stainless steels," *Metallurgical and Materials Transactions A,* vol. 39, no. 6, pp. 1327-1339, 2008, doi: 10.1007/s11661-008-9506-5.

[35] S. Matsuoka, "Effects of hydrogen on fatigue crack growth and stretch zone of 0.08 mass%C low carbon steel pipe," (in eng), *Nihon Kikai Gakkai Ronbunshu, A Hen/Transactions of the Japan Society of Mechanical Engineers, Part A,* vol. 74, no. 12, pp. 1528-1537, 2008.

[36] S. Matsuoka, O. Takakuwa, S. Okazaki, M. Yoshikawa, J. Yamabe, and H. Matsunaga, "Peculiar temperature dependence of hydrogen-enhanced fatigue crack growth of low-carbon steel in gaseous hydrogen," *Scripta Materialia,* vol. 154, pp. 101-105, 2018/09/01/ 2018, doi: https://doi.org/10.1016/j.scriptamat.2018.05.035.

[37] S. Matsuoka, H. Tanaka, N. Homma, and Y. Murakami, "Influence of hydrogen and frequency on fatigue crack growth behavior of Cr-Mo steel," *International Journal of Fracture,* vol. 168, no. 1, pp. 101-112, 2011, doi: 10.1007/s10704-010-9560-z.

[38] G. Wang, Y. Yan, X. Yang, J. Li, and L. Qiao, "Investigation of hydrogen evolution and enrichment by scanning Kelvin probe force microscopy," *Electrochemistry Communications,* vol. 35, pp. 100-103, 2013/10/01/ 2013, doi: https://doi.org/10.1016/j.elecom.2013.08.006.

[39] Y. Jiang, C. Li, D. Wang, and X. Di, "Effect of cyclic plastic deformation on hydrogen diffusion behavior and embrittlement susceptibility of reeling-pipeline steel weldments," *International Journal of Hydrogen Energy,* vol. 46, no. 58, pp. 30158-30172, 2021/08/23/ 2021, doi: https://doi.org/10.1016/j.ijhydene.2021.06.135.

[40] P. Sofronis, "Numerical analysis of hydrogen transport near a blunting crack tip," (in eng), *Journal of the Mechanics and Physics of Solids*, vol. 37, no. 3, pp. 317-350, 1989.

[41] H. A. Wriedt and R. A. Oriani, "Effect of tensile and compressive elastic stress on equilibrium hydrogen solubility in a solid," *Acta Metallurgica*, vol. 18, no. 7, pp. 753-760, 1970/07/01/ 1970, doi: https://doi.org/10.1016/0001-6160(70)90039-8.

[42] M. Nagumo, *Fundamentals of hydrogen embrittlement* (Fundamentals of hydrogen embrittlement). springer singapore, 2016, pp. 1-239.

[43] J. K. Tien, R. J. Richards, O. Buck, and H. L. Marcus, "Model of dislocation sweep-in of hydrogen during fatigue crack growth," *Scripta Metallurgica*, vol. 9, no. 10, pp. 1097-1101, 1975/10/01/ 1975, doi: https://doi.org/10.1016/0036-9748(75)90287-2.

[44] "*Standard practice for microetching metals and alloys," ASTM E407*, 2015.

[45] S. Laliberté-Riverin, J. Bellemare, F. Sirois, and M. Brochu, "Determination of hydrogen embrittlement stress intensity threshold by fractography," *Materialia*, vol. 12, 2020, doi: 10.1016/j.mtla.2020.100759.

[46] T. Misawa, A. P. Nomachi, and H. Sugawara, "Effect Of Cathodic Hydrogen Charging On Crack Propagation In Austenitic Stainless Steels Under Cyclic Loading," *Boshoku gijutsu*, vol. 30, no. 4, pp. 227-229, 1981, doi: 10.3323/jcorr1974.30.4_227.

[47] Z. Wu, K. Zhang, Y. Hong, C. Zhou, J. Zheng, and L. Zhang, "The dependence of fatigue crack growth on hydrogen in warm-rolled 316 austenitic stainless steel," *International Journal of Hydrogen Energy*, vol. 46, no. 23, pp. 12348-12360, 2021, doi: 10.1016/j.ijhydene.2020.03.247.

[48] H. Tanaka, N. Homma, S. Matsuoka, and Y. Murakami, "Effect of hydrogen and frequency on fatigue behavior of SCM435 steel for storage cylinder of hydrogen station," *Nihon kikai gakkai ronbunshu, a hen/transactions of the japan society of mechanical engineers, Part A*, vol. 73, no. 12, pp. 1358-1365, 2007, doi: 10.1299/kikaia.73.1358.

[49] H. K. Birnbaum and P. Sofronis, "Hydrogen-enhanced localized plasticity-a mechanism for hydrogen-related fracture," *Materials Science and Engineering A*, vol. A176, no. 1-2, pp. 191-202, 1994.

[50] W. W. Gerberich, R. A. Oriani, M. J. Lji, X. Chen, and T. Foecke, "The necessity of both plasticity and brittleness in the fracture thresholds of iron," *Philosophical Magazine A*, vol. 63, no. 2, pp. 363-376, 1991/02/01 1991, doi: 10.1080/01418619108204854.

[51] "*Standard Test Methods for Determining Average Grain Size*," *ASTM E112-13*, 2021.

[52] R. A. Young, *The rietveld method*. International union of crystallography, 1993.

[53] J. a. M. de Araújo, R., "Simple models for diffusion in thin plates or membranes," *Journal of Applied Mathematics and Physics*, vol. 7, pp. 1547-1559, 2019, doi: 10.4236/jamp.2019.77105.

[54] K. G. Solheim, J. K. Solberg, J. Walmsley, F. Rosenqvist, and T. H. Bjorna, "The role of retained austenite in hydrogen embrittlement of supermartensitic stainless steel," *Engineering Failure Analysis*, vol. 34, pp. 140-149, 2013, doi: 10.1016/j.engfailanal.2013.07.025.

[55] H. H. johnson, "Hydrogen in metals," Ohaio, USA, A. W. T. I. M. Bernstein, Ed., 1974: ASM, p. p.35.

[56] G. Irwin, "Linear fracture mechanics, fracture transition, and fracture control," *Engineering fracture mechanics*, vol. 1, no. 2, pp. 241-257, 1968.

[57] S. Godin, J. Hamel-Akre, D. Thibault, A.-M. Serventi, and P. Bocher, "Ni and Mn enrichment effects on reformed austenite: thermodynamical and low cycle fatigue stability of 13%Cr4%Ni and 13%Cr6%Ni stainless steels," *SN Applied Sciences*, vol. 2, no. 3, 2020, doi: 10.1007/s42452-020-2180-y.

[58] Y. D. Park, I. S. Maroef, A. Landau, and D. L. Olson, "Retained Austenite as a hydrogen trap in steel welds," *Welding Journal (Miami, Fla)*, vol. 81, no. 2, pp. 27/S-35/S, 2002.